Probing disorder-driven topological phase transitions via topological edge modes in Floquet-engineered honeycomb lattices

Alexander Christian Hesse

SIGILL. UNIVERSITAT. LUDOVIC. MAXIM.

München 2025

Probing disorder-driven topological phase transitions via topological edge modes in Floquet-engineered honeycomb lattices

Dissertation an der Fakultät für Physik
Ludwig-Maximilians-Universität München

vorgelegt von

Alexander Christian Hesse

aus Werl

München, den 21.10.2025

Tag der mündlichen Prüfung: 1. 12. 2025

Erstgutachter: Prof. Immanuel Bloch

Zweitgutachter: Prof. André Eckardt

Weitere Prüfungskommissionsmitglieder: Prof. Thomas Birner, Prof. Alexander Högele

Zusammenfassung

In dieser Arbeit wird über die Beobachtung von unordnungsgetriebenen topologischen Phasenübergängen in einem tunnelmodulierten optischen Gitter berichtet. Da konventionelle Methoden zur Charakterisierung topologischer Regimes in optischen Gittern in der Gegenwart von Unordnung versagen, entwickeln und verwenden wir eine Technik, die auf der direkten Beobachtung der Randzustände des Systems basiert, welche über die Korrespondenz zwischen Volumen und Rand mit den topologischen Eigenschaften des Volumens verknüpft sind.

Floquet-Engineering, das heißt in diesem Fall die periodische Modulation des Tunnelns in unserem optischen Gitter, kann abhängig von den Parametern der Modulation mehrere verschiedene topologische Phasen realisieren. Unter diesen Phasen befindet sich eine anomale Floquet-Phase – eine echte Nichtgleichgewichtsphase – in der die Chern-Zahl verschwindet, während topologische Randmoden bestehen bleiben. Wir entwickeln Protokolle zur Population der Randmoden in drei unterschiedlichen topologischen Regimes des modulierten Gitters, indem wir ein eng lokalisiertes Wellenpaket nahe einer topologischen Grenzfläche platzieren, die mittels einer von einem digitalen Mikrospiegelgeräts projizierten Potentialstufe gebildet wird. Wir untersuchen die Entstehung der Randmode durch die Variation der Höhe der Potentialstufe und bestimmen die charakteristische Energieskala in den drei topologischen Regimes. Wir untersuchen auch die Abhängigkeit der Randmodengeschwindigkeit im Haldane-Regime von der Breite der topologischen Grenzfläche.

Wenn Unordnung in topologisch nichttriviale Systeme eingeführt wird, wird erwartet, dass die Propagation der Randmoden robust gegenüber Rückstreuung für Unordnungsstärken ist, die die Energielücke des Systems nicht schließen. Wir untersuchen die Propagation der Randmode im Haldane-Regime unseres Systems in Gegenwart von Unordnung und beobachten eine unordnungsinduzierte Geschwindigkeitsrenormierung der Randmode. Anschließend nutzen wir die Abhängigkeit der Randmodenpopulation vom konkreten Präparationsprotokoll, um selektiv nur die Randmode im anomalen Floquet-Regime zu besetzen, was es uns ermöglicht, den Phasenübergang zwischen dem anomalen Floquet- und dem Haldane-Regime auch in der Anwesenheit von Unordnung zu verfolgen. Hier beobachten wir einen unordnungsgetriebenen Phasenübergang zwischen zwei topologisch nichttrivialen Regimes. Wir beenden unsere Untersuchung, indem wir das Verhalten bei starker Unordnung untersuchen und den Übergang sowohl des anomalen Floquet- als auch des Haldane-Regimes zu einer topologisch trivialen Phase im Limit starker Unordnung beobachten.

Diese Ergebnisse legen die Grundlage für weitere Untersuchungen ungeordneter topologischer Phasen mittels Randzuständen, insbesondere im Hinblick auf die Beobachtung eines anomalen Floquet-Anderson-Isolators, eines Systems, in dem der Randtransport auch dann aufrechterhalten werden kann, wenn das Volumen vollständig lokalisiert ist.

Abstract

This thesis presents the observation of disorder-driven topological phase transitions in a tunneling-modulated optical lattice. As conventional methods for characterizing topological regimes in optical lattices fail in the presence of disorder, we develop and employ a technique based on the direct observation of the system's edge states, which are linked to the topological properties of the bulk via the bulk-boundary correspondence.

Floquet engineering, i.e. the periodic modulation of the tunneling in our optical lattice, can, depending on the parameters of the modulation, realize multiple different topological phases. Among these phases is an anomalous Floquet phase – a genuine out-of-equilibrium phase – in which the Chern number vanishes, while topological edge modes persist. We develop protocols for populating the edge modes in three distinct topological regimes of the modulated lattice by releasing a tightly confined wave packet near a topological interface, which is formed by a potential step projected using a digital micromirror device. We investigate the emergence of the edge mode by varying the height of the potential step, and determine the characteristic energy scale in the three topological regimes. We also investigate the dependence of the edge mode velocity in the Haldane regime on the width of the topogical interface.

When disorder is introduced into topologically nontrivial systems, the propagation of the edge modes is expected to be robust to backscattering for disorder strengths which do not close the energy gap of the system. We investigate the propagation of the edge mode in the Haldane regime of our system in the presence of disorder, observing disorder-induced velocity renormalization of the edge mode. We then utilize the dependence of the edge mode population on the precise preparation protocol to selectively only populate the edge mode in the anomalous Floquet regime, enabling us to track the phase transition between the anomalous Floquet- and Haldane regime, even in the presence of disorder. Here, we observe a disorder-driven phase transition between two topologically nontrivial regimes. We close our investigation by studying the large-disorder behavior, observing the transition of both the anomalous Floquet as well as of the Haldane regime to a topologically trivial phase in the limit of large disorder.

These results establish the groundwork for further investigations of disordered topological phases using edge states, in particular towards the observation of an anomalous Floquet Anderson insulator, a system in which edge transport can sustain even when the bulk is fully localized.

Contents

CHAPTER 1

Introduction

The classification of phases of matter in terms of symmetries and order parameters has been a foundational tool in physics [1], with Landau's framework of spontaneous symmetry breaking [2] providing a systematic approach to understanding how phase transitions arise from changes in symmetry: For instance, the transition from a paramagnet to a ferromagnet involves the breaking of rotational symmetry [1, 3, 4], and the phase transition from a liquid to a solid requires the breaking of continuous translational symmetry [1].

The discovery of the integer quantum Hall effect (QHE) in 1980 [5–7] demonstrated the limitations of symmetry-based phase classification [1, 8], and has since evolved into one of the most prominent examples for topological phases of matter [1, 9, 10]: When a two-dimensional (2D) electron gas is subjected to a strong perpendicular magnetic field at low temperatures, its Hall conductance becomes quantized in units of e^2/h. This quantization cannot be understood through symmetry breaking, but instead emerges from the topological properties of the electronic wavefunctions. Since this quantization originates from an integer topological invariant, it is topologically protected against small perturbations of the system, and is therefore robust against microscopic imperfections of the material [11, 12]. Strikingly, this quantized transport is not only robust to defects in the material, but instead even relies on the presence of some amount of disorder [13–15]: While for a perfectly clean system a linear increase of resistance with magnetic field is expected, the localization of states due to defects in the material enable the resistance to stay constant if the chemical potential is varied on these localized states [15], underlining the key role disorder can play in shaping the properties of topological systems.

The quantized Hall conductivity is closely linked to the existence of edge states – unidirectional transport channels immune to backscattering, and consequently to the localization from disorder – via the bulk-boundary correspondence [16]. Since the position the plateaus observed in these measurements only depends on the electron charge e and Planck's constant h together with the aforementioned integer topological invariant, the von-Klitzing constant $R_K = h/e^2$ extracted from QHE measurements has been widely used as a resistance standard in metrology applications, and its value has been fixed in the 2019 redefinition of the SI units [17], using QHE measurements as a basis.

The mathematical concepts underlying these phenomena draw from differential topology, where systems are classified by global invariants that remain unchanged under continuous deformations [1, 18, 19]. Closed surfaces provide an intuitive example: They are topologically classified by their genus g, where g counts the holes in the surface, with surfaces of equal genus being continuously deformable into one another. A torus with $g = 1$ can be smoothly transformed into any other single-holed surface, yet no continuous deformation can connect it to a sphere with $g = 0$.

These topological invariants are expressed as integrals of geometric quantities. In condensed matter systems, the curvature of an energy band in the Brillouin zone – the Berry curvature – yields an integer invariant known as the Chern number when integrated,

$$\mathcal{C} = \frac{1}{2\pi} \int_{\mathrm{BZ}} \Omega d^2 k. \tag{1.1}$$

In the quantum Hall effect, the plateaus of the Hall conductivity are labeled by integers that correspond to the sum of Chern numbers across all occupied bands.

Because this formulation leads to equal results for two gapped systems, it follows that – provided there exists a continuous transformation between them that does not close the energy gap – these systems are robust to a certain degree of perturbation, and they belong to the same topological class [1, 9, 10, 20, 21]. While the emergence of topological phases of matter is not fundamentally rooted in symmetry breaking, they can nonetheless be systematically classified according to the discrete symmetries preserved of the underlying Hamiltonian, using the Altland-Zirnbauer (AZ) classification [22, 23]. Here, the Hamiltonians are categorized by the dimensionality of the system, as well as the presence or absence of time-reversal, charge conjugation, and chiral symmetry. QHE systems, where all three symmetries are broken in a 2D system, belong to the class $\mathbb{Z}$, indicating that the topological invariant $\mathcal{C}$ can be any integer number. Another system, which belongs to the same class, are so-called Chern insulators, which support quantum Hall states without relying on an external magnetic field. The Haldane model [24] exhibits topologically protected edge states on a hexagonal lattice. Additional spin-orbit coupling can lead to the conservation of time-reversal symmetry in these systems [25, 26]. Such a quantum spin Hall insulator was first experimentally observed in semiconductor quantum wells [27, 28].

Interactions in topological systems can lead to even richer physics, with the most prominent example being the fractional quantum Hall effect [29–31], where plateaus in the conductivity form at fractional values of e^2/h. Special interest lies on these states as they can feature non-Abelian anyons [32, 33].

Engineering topological Bloch bands with ultracold atoms in optical lattices

Since the first observation of Bose-Einstein condensation (BEC) [34, 35] and degenerate Fermi gases [36], ultracold atomic systems have developed into a versatile tool for simulating the behavior of different quantum systems. The interaction between the atoms can be tuned via Feshbach resonances [37–39], they can be placed in optical lattices of varying lattice geometries [40–42], and dimensionality can be controlled by varying the confinement along different directions [43]. In the presence of optical lattices, defect-free condensed matter systems can be studied [44, 45], with quantum gas microscopes [46–48] allowing to probe these systems with single lattice site resolution. In addition to this, applying optical dipole potentials [49] to these systems allows to confine them with a high degree of control [50–52] or trap individual atoms in optical tweezers [53, 54].

The realization of topological phases with neutral atoms however presents unique challenges, as charge-neutral atoms, unlike electrons, do not couple to magnetic fields, so that alternative approaches for creating the necessary complex tunneling elements are needed [55]. To realize topological phases, Floquet engineering – the periodic modulation of parameters of the Hamiltonian of the system – has proven to be a successful tool. In the high-frequency limit, where $\hbar\omega$, with $\omega/(2\pi)$ being the modulation frequency, exceeds all other energy scales, Floquet systems simulate effective static Hamiltonians. This enabled the experimental realization of the Hofstadter model [56–58] and of Haldane-type Hamiltonians [59–61].

More recently, Floquet engineering has enabled the realization of strongly interacting topological systems, such as the Meissner phase [62]. Special interest lies again in fractional quantum hall systems, which only recently have become accessible in small systems by employing Floquet engineering, with realizations using ultracold atoms in optical lattices [63], and in superconducting circuits [64].

As the driving frequency of the Floquet scheme is decreased and becomes comparable to the system's energy scales however, genuine out-of-equilibrium phases can emerge. These systems can no longer be characterized by just the Chern number, but the characterization of this multi-band-system requires knowledge of multiple winding numbers [65]. Here, particular interest lies in the exotic behavior such systems can exhibit in the presence of disorder, as, while in a static system the conductivity in the edge channels is directly connected to the conductivity in the bulk of the system via the bulk-boundary correspondence [16], in a so-called anomalous Floquet Anderson insulator (AFAI), edge transport can sustain even when the bulk is fully localized [66, 67].

Due to the high interest in topological phases of matter, numerous techniques have been developed to characterize the geometric properties of engineered topological Bloch bands with cold atoms [60, 68–72]. However, they almost exclusively rely on the translational invariance of the underlying lattice, so that they fail in the presence of disorder, hindering the investigation of topology in these systems.

The introduction of disorder can also lead to the emergence of new topological phases. Topological Anderson insulators [73] can emerge when disorder is introduced into topologically trivial systems. Such systems have so far only been studied in topological pumps and in 1D momentum space lattices on ultracold atom platforms [74, 75], while 2D realizations have only been demonstrated in photonic systems [76–78]. The study of disorder-driven phase transitions in ultracold atomic systems in 2D however remains as elusive as the study of disorder-driven phase transitions between two topologically nontrivial regimes.

Contents of this thesis

This thesis presents the observation of a disorder-driven phase transition between two topologically non-trivial regimes in a Floquet-modulated two-dimensional optical lattice. By modulating the tunneling in this system, we can realize several topologically non-trivial phases [61]. We probe these systems by populating their edge states [79]. To this end, we place a tightly confined wavepacket in the vicinity of a topological interface, and observe the subsequent chiral evolution along the interface. By precisely controlling the location, spatial extent and phase profile of this wave packet, we can populate the edge state of the different phases realized by our Floquet scheme. By varying the height of the topological interface, we are able to probe the emergence of these edge modes, determining the characteristic energy scale for the different regimes. By tuning the width of the potential, we can observe a reduction in propagation velocity of the Haldane edge state.

In a second set of experiments, we probe the topological properties of our system in the presence of disorder [80]. By populating the edge state of the Haldane phase in a disordered potential landscape, we are able to observe disorder-induced velocity renormalization. Furthermore, we utilize the dependence of the edge mode population on the precise preparation protocol to selectively populate the edge state only in the anomalous Floquet regime. This enables us to track the location of the phase transition between the anomalous Floquet and the Haldane regime, even in the presence of disorder. Here, we observe a disorder-driven phase transition between two topologically nontrivial regimes. We close our investigation by probing the large-disorder behavior of the phase diagram, observing the transition of both the anomalous Floquet as well as of the Haldane regime into a topologically trivial phase.

This thesis is structured into six chapters as follows:

Chapter 2 provides the theoretical foundation, beginning with an introduction to geometrical phases and topological systems, with the Haldane model serving as a paradigmatic example of a Chern insulator. In the following, Floquet engineering is discussed, introducing out-of-equilibrium systems. In this context, anomalous Floquet systems are introduced, and their properties discussed. The chapter concludes with an introduction into disordered topological systems, establishing the observables which can be employed to characterize them.

Chapter 3 describes the experimental setup, and the steps for generating a BEC of ^{39}K on it are described. Detailed insights are given on the newly added components of the experiment: A speckle beam, which is employed to generate disorder in our systems, is characterized and calibrated carefully. Additional improvements to the imaging system are discussed, which allow us to take absorption pictures with higher signal to noise ratio than previously possible.

Chapter 4 presents experimental results on the observation and manipulation of edge states in a 2D real-space Floquet topological system. After establishing the preparation protocol, we demonstrate the observation of edge states in the anomalous Floquet regime. We then investigate the population of the edge states in the Haldane regime, and optimize the overlap of the prepared wave packet with them. We conclude by investigating the behavior of the edge states when the properties of the topological interface are changed. For this, we first vary the height of the potential step making up the topological interface, and study the emergence of edge modes, and the characteristic energy scale at which they emerge. Lastly, we probe the effect which the width of the topological interface has on the velocity of the edge modes.

Chapter 5 investigates the effect disorder has on the transport in the edge modes, and how it influences the topological phases in our system. We establish preparation protocols, which allow us to populate the edge mode of the system both in the anomalous- and Haldane regime, or just in the anomalous Floquet regime, thereby creating a sensitive probe for identifying topological regimes. The study begins by analyzing the transport properties in the Haldane regime under the influence of disorder. Next, we map out the phase diagram under the influence of disorder, using the edge states as a probe for the topological regime. We compare these results to gap-closing measurements at zero disorder, and to numerical simulations. Finally, we probe the behavior of the system for large disorder, examining the system close to the transition between anomalous- and Haldane system, as well as deep within both the anomalous and Haldane system.

The thesis concludes with a summary of its main results in Chapter 6, and a brief outlook on future directions is given.

Publications

The central results presented in this thesis have been published or appear as preprints in the following references:

- C. Braun, R. Saint-Jalm, **A. Hesse**, J. Arceri, I. Bloch, and M. Aidelsburger, *Real-space detection and manipulation of topological edge modes with ultracold atoms*, Nat. Phys. **20**, 1306 (2024)

- **A. Hesse**, J. Arceri, M. Hornung, C. Braun, and M. Aidelsburger, *Probing disorder-driven topological phase transitions via topological edge modes with ultracold atoms in Floquet-engineered honeycomb lattices*, arXiv:2508.20154, preprint (2025)

CHAPTER 2

Topological phases, Floquet engineering and disorder

The behavior of non-interacting electrons in periodic potentials (such as a crystal) is described in terms of a band structure, which can be classified according to its topological properties. In the following, we will first introduce the concept of geometric phases in Sec. 2.1, discussing the integer quantum Hall effect and the Haldane model. Subsequently, we will discuss Floquet engineering in Sec. 2.2, a technique commonly used for generating topologically nontrivial bandstructures with charge neutral ultracold atoms. Following that, we will discuss the tunneling-modulated honeycomb lattice in Sec. 2.3, and show how the modulation scheme realizes a Haldane model in the high-frequency limit. We will then discuss anomalous Floquet phases in Sec. 2.4, illustrating how such a system can be realized with the modulation scheme introduced in the previous section, and close our discussion by considering disordered systems in Sec. 2.5, first discussing the propagation of particles in a disordered potential landscape, and then introducing the Bott index, allowing to probe the system's topological properties in the presence of weak disorder.

2.1 Geometric phases in Bloch bands

A single particle in a periodic potential is described by the Hamiltonian

$$\hat{H}_L = \frac{\hat{\mathbf{p}}^2}{2m} + V_L\left(\mathbf{r}\right). \tag{2.1}$$

Here, $\hat{\mathbf{p}}$ is the momentum operator, m is the mass of the particle, and $V_L\left(\mathbf{r}\right) = V_L\left(\mathbf{r} + \mathbf{R}\right)$ is the potential, being periodic in $\mathbf{r}$ with periodicity $\mathbf{R}$. According to Bloch's theorem [3], the eigenstates of this system are the Bloch waves $\psi^n_{\mathbf{k}}\left(\mathbf{r}\right)$, given by

$$\psi^n_{\mathbf{k}}\left(\mathbf{r}\right) = e^{i\mathbf{k}\cdot\mathbf{r}} u^n_{\mathbf{k}}\left(\mathbf{r}\right), \tag{2.2}$$

where $u^n_{\mathbf{k}}\left(\mathbf{r}\right)$ has the same periodicity as the potential, i.e. $u^n_{\mathbf{k}}\left(\mathbf{r}\right) = u^n_{\mathbf{k}}\left(\mathbf{r} + \mathbf{R}\right)$.

Plugging this into the Schrödinger equation yields

$$\left(\frac{\hat{\mathbf{p}}^2}{2m} + V_L(\mathbf{r})\right)\psi_{\mathbf{k}}^n(\mathbf{r}) = E_{\mathbf{k}}^n \psi_{\mathbf{k}}^n(\mathbf{r}). \tag{2.3}$$

By plugging our ansatz from Eq. 2.2 into this, we can derive the eigenvalue equation for $u_{\mathbf{k}}^n(\mathbf{r})$:

$$\hat{H}_L(\mathbf{k})\, u_{\mathbf{k}}^n(\mathbf{r}) = E_{\mathbf{k}}^n u_{\mathbf{k}}^n(\mathbf{r}), \tag{2.4}$$

where

$$\hat{H}_L(\mathbf{k}) = \frac{(\hat{\mathbf{p}} + \hbar\mathbf{k})^2}{2m} + V_L(\mathbf{r}). \tag{2.5}$$

Here, $E_{\mathbf{k}}^n$ is the energy of the n-th band at quasimomentum $\mathbf{k}$. The geometric properties of Bloch bands become apparent, when we consider the adiabatic transport of a particle through quasimomentum space. According to the adiabatic theorem, a particle initialized in an eigenstate $|u_{\mathbf{k}(0)}^n\rangle$ of band n evolves along the path of instantaneous eigenstates $|u_{\mathbf{k}(t)}^n\rangle$ as the quasimomentum $\mathbf{k}(t)$ is slowly varied. The total phase acquired during this process, $\phi(t)$, can be decomposed into a dynamical contribution, ϕ_d, and a geometric contribution, ϕ_g,

$$\phi(t) = \phi_d(t) + \phi_g(t) = -\frac{1}{\hbar}\int_0^t E_n(\mathbf{k}(t')\, dt' + i\int_{\mathbf{k}(0)}^{\mathbf{k}(t)} \langle u_{\mathbf{k}'}^n|\nabla_{\mathbf{k}'}|u_{\mathbf{k}'}^n\rangle \cdot d\mathbf{k}'. \tag{2.6}$$

The dynamical phase ϕ_d is determined solely by the band's energy dispersion $E_n(\mathbf{k})$ as well as the duration of the evolution. The geometric phase ϕ_g in contrast is independent of time and energy, it only depends on the geometric path traced in the Brillouin zone. This motivates the definition of the Berry connection

$$\mathbf{A}_n(\mathbf{k}) = i\langle u_{\mathbf{k}}^n|\, \nabla_{\mathbf{k}}\, |u_{\mathbf{k}}^n\rangle. \tag{2.7}$$

While the Berry connection as well as the geometric phase for an open path are gauge dependent, the phase for a closed loop is a gauge-invariant physical quantity, and is called Berry phase [81]:

$$\oint_C \mathbf{A}_n(\mathbf{k})\, d\mathbf{k} = \int_S \Omega_n(\mathbf{k})\, d\mathbf{k}. \tag{2.8}$$

Here $\Omega_n(\mathbf{k})$ denotes the Berry curvature, which is gauge invariant, and is defined as the curl of the Berry connection

$$\Omega_n(\mathbf{k}) = \nabla_{\mathbf{k}} \times \mathbf{A}_n = i\langle \nabla_{\mathbf{k}} u_{\mathbf{k}}^n| \times |\nabla_{\mathbf{k}} u_{\mathbf{k}}^n\rangle. \tag{2.9}$$

This expression shows that the Berry curvature is an intrinsic property of the geometry of the Hilbert space parameterized by $\mathbf{k}$.

2.1.1 The quantum Hall effect and the bulk-boundary correspondence

While we so far only considered the effects the topological properties have on the Bloch bands of a system, the behavior at its edge is also determined by this. An example for this is the integer quantum Hall effect (QHE) [5–7]. Here, a two-dimensional electron gas at low temperatures is exposed to a strong magnetic field, and the current is measured while a transverse voltage is applied. In this scenario, one observes that the Hall conductivity σ_{xy} does not continuously increase with the applied magnetic field strength, but instead exhibits a series of flat plateaus, with the conductivity being quantized according to

$$\sigma_{xy} = \nu \frac{e^2}{h} \tag{2.10}$$

with ν being an integer. This quantized conductivity is a result of the topology of the Bloch bands, with Thouless, Kohmoto, Nightingale, and den Nijs (TKNN) showing that ν is a topological invariant of the system [16]. This invariant can be calculated by integrating the Berry curvature of a band over the entire Brillouin zone, yielding an integer known as the Chern number,

$$\mathcal{C}^n = \frac{1}{2\pi} \int_{BZ} d\mathbf{k}\, \Omega_n \left(\mathbf{k}\right). \tag{2.11}$$

The Chern number is connected to the existence of chiral edge states at the boundary of the system, connecting the localized bulk bands via channels, which are immune to backscattering. This relationship is known as the bulk-boundary correspondence, guaranteeing that a bulk material whose occupied bands have a net Chern number of $\mathcal{C}$ must host $|\mathcal{C}|$ protected, chiral states at its boundary.

2.1.2 The Haldane model

Topological insulators are classified by the fundamental symmetries they preserve. Systems in the Altland-Zirnbauer class A [22, 23] for example are characterized by a non-zero integer topological invariant. The canonical example for this is the integer quantum Hall (IQH) system, where time-reversal symmetry is broken by an applied magnetic field [5–7]. In 1988, the Haldane model was proposed [24], which realizes the same topological phase without the need for an external field. The Haldane model considers a honeycomb lattice, where TRS is broken internally by complex next-nearest-neighbor hopping amplitudes. These phases create a staggered pattern of magnetic flux with zero average per unit cell, opening a topologically non-trivial band gap. This system is the canonical exmple of a Chern insulator, demonstrating that topological nontrivial behavior can be an intrinsic property of a material's band structure. In the following, we will briefly discuss the main properties of the Haldane model.

The hexagonal lattice consists of two lattice sites per unit cell, such that two lattice vectors $\mathbf{a_1}$ and $\mathbf{a_2}$ are needed to describe the lattice:

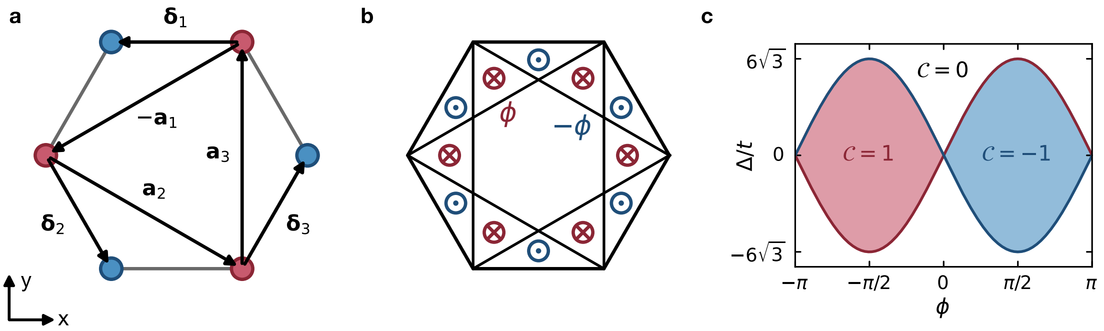

Figure 2.1 | **Tunneling directions, flux pattern and phase diagram of the Haldane model.** **a** Single plaquette of the honeycomb lattice. A-sites are colored in blue, while B-sites are colored in red. The vectors $\mathbf{a}_j$ connecting the lattice sites on the same sublattice as well as the vectors $\boldsymbol{\delta}_j$ connecting each lattice site to the three neighbouring sites are drawn in. **b** The flux pattern in a plaquette of the honeycomb lattice is illustrated. The plaquette is divided into 13 cells, of which 6 are each pierced by a positive or negative flux $\pm\varphi$. The central cell is not pierced by any flux. The net flux over the whole unit plaquette is zero. **c** Phase diagram of the Haldane model as a function of the complex nearest neighbor tunneling φ and of the sublattice offset Δ. The blue / red lines mark the location in the phase diagram at which the energy gap at **K** / **K**′ close. Between the gap closings, there are regions with $\mathcal{C}=1, \mathcal{C}=-1$, and outside of them a topologically trivial regime with $\mathcal{C}=0$.

$$\mathbf{a}_1 = \frac{a}{2}\begin{pmatrix}3\\ \sqrt{3}\end{pmatrix} \qquad \mathbf{a}_2 = \frac{a}{2}\begin{pmatrix}3\\ -\sqrt{3}\end{pmatrix}, \tag{2.12}$$

where the lattice spacing a is the distance between two adjacent lattice sites. We additionally define $\mathbf{a_3} = \mathbf{a_1} - \mathbf{a_2}$ for convenience. The A- and the B-sites of the lattice are connected via the vectors $\boldsymbol{\delta}_j$, with

$$\boldsymbol{\delta}_1 = a\begin{pmatrix}-1\\ 0\end{pmatrix} \qquad \boldsymbol{\delta}_2 = \frac{a}{2}\begin{pmatrix}1\\ -\sqrt{3}\end{pmatrix} \qquad \boldsymbol{\delta}_3 = \frac{a}{2}\begin{pmatrix}1\\ \sqrt{3}\end{pmatrix}. \tag{2.13}$$

These vectors are, in comparison to a plaquette of the hexagonal lattice, illustrated in Fig. 2.1a. We also define our reciprocal lattice vectors, which span the Brillouin zone, as

$$\mathbf{k}_1 = \frac{k_L}{2}\begin{pmatrix}\sqrt{3}\\ 3\end{pmatrix} \qquad \mathbf{k}_2 = \frac{k_L}{2}\begin{pmatrix}\sqrt{3}\\ -3\end{pmatrix}, \tag{2.14}$$

with $k_L = \frac{4\pi}{3\sqrt{3}a}$.

Tight-binding description In the Haldane model, a real tunneling with amplitude J is considered for nearest neighbour tunneling, while next-nearest neighbour tunneling has an amplitude J', which can be complex:

$$J' = te^{i\phi} \tag{2.15}$$

The resulting flux pattern in a plaquette of the hexagonal lattice is illustrated in Fig. 2.1b. The Hamiltonian of the Haldane model can be written in a tight-binding description as follows:

$$\begin{aligned}\hat{H} = \sum_{\mathbf{r}_A} \Bigg[J \sum_{j=1}^{3} \left(\hat{a}^\dagger_{\mathbf{r}_A} \hat{a}_{\mathbf{r}_A+\boldsymbol{\delta}_j} + h.c. \right) + \frac{\Delta}{2} \left(\hat{a}^\dagger_{\mathbf{r}_A} \hat{a}_{\mathbf{r}_A} - \hat{a}^\dagger_{\mathbf{r}_A-\boldsymbol{\delta}_1} \hat{a}_{\mathbf{r}_A-\boldsymbol{\delta}_1} \right) \\ \sum_{j=1}^{3} \left(J' \hat{a}^\dagger_{\mathbf{r}_A} \hat{a}_{\mathbf{r}_A+\mathbf{a}_j} + h.c. \right) + \sum_{j=1}^{3} \left(J' \hat{a}^\dagger_{\mathbf{r}_A-\boldsymbol{\delta}_1} \hat{a}_{\mathbf{r}_A-\boldsymbol{\delta}_1-\mathbf{a}_j} + h.c. \right) \Bigg]\end{aligned} \tag{2.16}$$

Here, we perform a sum over the tunnelings of all sites, with $\mathbf{r}_A$ being the location of an A-site, and the positions of the B-sites being described by $\mathbf{r}_A - \boldsymbol{\delta}_1$. The operators $\hat{a}_\mathbf{r}$ and $\hat{a}^\dagger_\mathbf{r}$ are the annihilation and creation operators for the particle number on a lattice site at $\mathbf{r}$, respectively.

We can now derive the energy dispersion of the Hamiltonian by making use of the Fourier transform of the creation and annihilation operators

$$\begin{aligned} \hat{a}^\dagger_{\mathbf{r}_A} &= \frac{1}{\sqrt{N}} \sum_{\mathbf{k}} e^{-i\mathbf{k}\cdot\mathbf{r}_A} a^\dagger_{\mathbf{k}} & \hat{a}_{\mathbf{r}_A} &= \frac{1}{\sqrt{N}} \sum_{\mathbf{k}} e^{i\mathbf{k}\cdot\mathbf{r}_A} \hat{a}_{\mathbf{k}} \\ \hat{a}^\dagger_{\mathbf{r}_A-\boldsymbol{\delta}_1} &= \frac{1}{\sqrt{N}} \sum_{\mathbf{k}} e^{-i\mathbf{k}\cdot(\mathbf{r}_A-\boldsymbol{\delta}_1)} \hat{b}^\dagger_{\mathbf{k}} & \hat{a}_{\mathbf{r}_A-\boldsymbol{\delta}_1} &= \frac{1}{\sqrt{N}} \sum_{\mathbf{k}} e^{i\mathbf{k}\cdot(\mathbf{r}_A-\boldsymbol{\delta}_1)} \hat{b}_{\mathbf{k}} \end{aligned} \tag{2.17}$$

with N being the number of unit cells. Plugging this into Eq. 2.16, we yield

$$\begin{aligned} \hat{H} = \sum_{\mathbf{k}} \Bigg[& J \sum_{j=1}^{3} \left(\hat{a}^\dagger_{\mathbf{k}} \hat{b}^\dagger_{\mathbf{k}} e^{i\mathbf{k}\cdot\delta_j} + h.c. \right) \\ & + \sum_{j=1}^{3} J' \left(\hat{a}^\dagger_{\mathbf{k}} \hat{a}_{\mathbf{k}} e^{i\mathbf{k}\cdot\mathbf{a}_j} + \hat{b}^\dagger_{\mathbf{k}} \hat{b}_{\mathbf{k}} e^{-i\mathbf{k}\cdot\mathbf{a}_j} \right) + h.c. \\ & + \frac{\Delta}{2} \left(\hat{a}^\dagger_{\mathbf{k}} \hat{a}_{\mathbf{k}} - \hat{b}^\dagger_{\mathbf{k}} \hat{b}_{\mathbf{k}} \right) \Bigg]. \end{aligned} \tag{2.18}$$

This is equivalent to a two-level system at each quasimomentum $\mathbf{k}$, so that the system can be expressed in terms of the Pauli matrices

$$\sigma_0 = \begin{pmatrix} 1 & 0 \\ 0 & 1 \end{pmatrix}, \qquad \sigma_x = \begin{pmatrix} 0 & 1 \\ 1 & 0 \end{pmatrix}, \qquad \sigma_y = \begin{pmatrix} 0 & -i \\ i & 0 \end{pmatrix}, \qquad \sigma_z = \begin{pmatrix} 1 & 0 \\ 0 & -1 \end{pmatrix} \tag{2.19}$$

as

$$\hat{H}(\mathbf{k}) = \hat{\sigma}_0 h_0(\mathbf{k}) + \hat{\boldsymbol{\sigma}} \cdot \mathbf{h}(\mathbf{k}). \tag{2.20}$$

Here, $h_0(\mathbf{k})$ and $\mathbf{h}(\mathbf{k})$ are defined as

$$\begin{aligned} h_0(\mathbf{k}) &= 2t\cos(\phi)\sum_{j=1}^{3}\cos(\mathbf{k}\cdot\mathbf{a}_j) \\ h_x(\mathbf{k}) &= J\sum_{j=1}^{3}\cos(\mathbf{k}\cdot\boldsymbol{\delta}_j) \\ h_y(\mathbf{k}) &= -J\sum_{j=1}^{3}\sin(\mathbf{k}\cdot\boldsymbol{\delta}_j) \\ h_z(\mathbf{k}) &= \frac{\Delta}{2} - 2t\sin(\phi)\sum_{j=1}^{3}\sin(\mathbf{k}\cdot\mathbf{a}_j). \end{aligned} \tag{2.21}$$

Calculating the eigenvalues of this system yields

$$E^{\pm}(\mathbf{k}) = h_0(\mathbf{k}) \pm |\mathbf{h}(\mathbf{k})|. \tag{2.22}$$

Phase transitions in the Haldane model We now investigate the gap closing points of this system. At the points $\mathbf{K}$ / $\mathbf{K}'$ located at

$$\mathbf{K} = k_L \begin{pmatrix} 0 \\ 1 \end{pmatrix} \qquad \mathbf{K}' = k_L \begin{pmatrix} 0 \\ -1 \end{pmatrix}, \tag{2.23}$$

with $k_L = \frac{4\pi}{3\sqrt{3}a}$, the contributions of $h_x(\mathbf{k})$ and $h_y(\mathbf{k})$ vanish. In addition to that, we can neglect the contribution of $h_0(\mathbf{k})$, as it shifts both bands simultaneously due to the multiplication with σ_0. This way we solve

$$\begin{aligned} h_z(\mathbf{K}) &= \frac{\Delta}{2} - 2t\sin(\phi)\left(\frac{3\sqrt{3}}{2}\right) \overset{!}{=} 0 \\ &\Rightarrow \Delta = 6\sqrt{3}t\sin(\phi) \end{aligned} \tag{2.24}$$

$$
\begin{aligned}
h_z\left(\mathbf{K}'\right) &= \frac{\Delta}{2} - 2t\sin\left(\phi\right)\left(-\frac{3\sqrt{3}}{2}\right) \overset{!}{=} 0 \\
&\Rightarrow \Delta = -6\sqrt{3}t\sin\left(\phi\right). \qquad (2.25)
\end{aligned}
$$

These gap closing points are illustrated in Fig. 2.1c. The topological invariant that characterizes the different phases here is the Chern number $\mathcal{C}$. As the Berry curvature is localized around the dirac cones at $\mathbf{K}$ and $\mathbf{K}'$, the Chern number can be calculated directly by summing the contributions from each Dirac point

$$
\mathcal{C} = \frac{1}{2}\left[\operatorname{sgn}\left(h_z\left(\mathbf{K}\right)\right) - \operatorname{sgn}\left(h_z\left(\mathbf{K}'\right)\right)\right]. \qquad (2.26)
$$

Here, the contribution at the $\mathbf{K}'$ point is subtracted due to the opposite chirality compared to $\mathbf{K}$, as can be seen from a Taylor expansion of the system around the Dirac points.

From this, one can see that $\mathcal{C} = 0$ for $\left|\frac{\Delta}{2}\right| > \left|3\sqrt{3}t\sin\phi\right|$, and $\mathcal{C} = \pm 1$ otherwise, with $\mathcal{C} = 1$ for $\phi \in (0, \pi)$, and $\mathcal{C} = -1$ for $\phi \in (-\pi, 0)$. This is illustrated, together with the gap-closing points, in Fig. 2.1c.

This model can also be understood in terms of symmetries: As the next-nearest neighbour tunneling $J' = te^{i\phi}$ can be complex, it is apparent that time-reversal symmetry is broken unless $\phi = N\pi$, with $N \in \mathbb{Z}$. In the presence of time-reversal symmetry, the system is always topologically trivial. Another symmetry of this system is inversion symmetry: For $\Delta = 0$, inversion symmetry is present, and the system is topologically nontrivial for $\phi \neq N\pi$ and $t \neq 0$. If both inversion symmetry as well as time reversal symmetry are broken, the system is topologically trivial for $|\Delta| > 6\sqrt{3}t\sin\phi$. In the Altland-Zirnbauer classification [22, 23] the Haldane model belongs to class A, and is an exmple of a Chern insulator.

2.2 Floquet engineering

The Floquet theorem [82–84] states, that the evolution of a time-periodic Hamiltonian $\hat{H}(t) = \hat{H}(t+T)$ can be described by an effective Hamiltonian, if it is probed stroboscopically after $n \cdot T, n \in \mathbb{Z}$. According to the Floquet theorem, the solution of the time-dependent Schrödinger equation

$$
i\hbar\frac{\partial}{\partial t}\left|\psi\left(t\right)\right\rangle = \hat{H}\left(t\right)\left|\psi\left(t\right)\right\rangle \qquad (2.27)
$$

of such a system are the so called Floquet states

$$
\psi_n\left(t\right) = e^{-i\epsilon_n t/\hbar}\left|\phi_n\left(t\right)\right\rangle. \qquad (2.28)
$$

Here, $\phi_n(t) = \phi_n(t+T)$ are the so-called Floquet modes of the system, with ϵ_n being their quasienergy. By inserting the Floquet states into the time-dependent Schrödinger equation one obtains

$$\left(\hat{H}\left(t\right)-i\hbar\frac{\partial}{\partial t}\right)\left|\phi_n\left(t\right)\right\rangle=\epsilon_n\left|\phi_n\left(t\right)\right\rangle. \tag{2.29}$$

The eigenenergies ϵ_n due to this equation are not uniquely defined, as becomes evident when multiplying them with a global phase factor

$$\phi_{n,m}\left(t\right)=e^{-i(m\hbar\omega)t/\hbar}\left|\phi_n\left(t\right)\right\rangle \tag{2.30}$$

with $m\in\mathbb{Z}$, and $\omega/(2\pi)=1/T$ being the driving frequency of the system. Inserting this into Eq. 2.29 yields the eigenenergies

$$\epsilon_{n,m}=\epsilon_n+m\hbar\omega. \tag{2.31}$$

This leaves the eigenstate of the time-dependent Hamiltonian unchanged

$$\left|\psi_{n,m}\left(t\right)\right\rangle=e^{-i(\epsilon_n+m\hbar\omega)t/\hbar}\cdot e^{im\omega t}\left|\phi_n\left(t\right)\right\rangle, \tag{2.32}$$

so that all solutions defined in Eq. 2.30 are physically equivalent. This means, that the quasienergy ϵ_n is unique only up to integer multiples of $\hbar\omega$, and that the energy spectrum of the system consists of infinitely many copies of each band, separated by $\hbar\omega$. In analogy to the Brillouin zone defined for quasimomenta, we can restrict the quasienergies to lie within the Floquet Brillouin zone,

$$\epsilon_n\in\left]-\frac{\hbar\omega}{2},\frac{\hbar\omega}{2}\right]. \tag{2.33}$$

Effective Hamiltonian The evolution of an eigenstate $\left|\psi_n\left(t\right)\right\rangle$ during one modulation period of the Hamiltonian can be written as

$$\left|\psi_n\left(t_0+T\right)\right\rangle=\hat{U}\left(t_0+T,t_0\right)\left|\psi_n\left(t_0\right)\right\rangle=\hat{\mathcal{T}}e^{-\frac{i}{\hbar}\int_{t_0}^{t_0+T}\hat{H}(t)dt}\left|\psi_n\left(t_0\right)\right\rangle. \tag{2.34}$$

with $\hat{\mathcal{T}}$ being the time-ordering operator. According to the Floquet theorem, $\hat{U}$ can be factored into a form separating the dynamics

$$\hat{U}\left(t,t_0\right)=\hat{U}_\mathrm{F}\left(t\right)e^{-i\hat{H}_\mathrm{eff}(t-t_0)/\hbar}\hat{U}_\mathrm{F}^\dagger\left(t_0\right) \tag{2.35}$$

where $\hat{U}_\mathrm{F}(t)=\hat{U}_\mathrm{F}(t+T)$ is a time-periodic unitary operator known as the micromotion operator, while $\hat{H}_\mathrm{eff}$ is time-independent, and is given by

$$\hat{H}_\mathrm{eff}=\hat{U}_\mathrm{F}^\dagger(t)\hat{H}(t)\hat{U}_\mathrm{F}(t)-i\hbar\hat{U}_\mathrm{F}^\dagger(t)\dot{\hat{U}}_\mathrm{F}(t). \tag{2.36}$$

It is important to note that the effective Hamiltonian $\hat{H}_\mathrm{eff}$ as well as the micromotion operator $\hat{U}_\mathrm{F}$ are not uniquely defined [85]. A simple way to see this is to multiply the micromotion operator with an arbitrary unitary operator from the right. A common choice for this is to

$\hat{U}'_{\mathrm{F}}(t) = \hat{U}_{\mathrm{F}}(t)\hat{U}^{\dagger}_{\mathrm{F}}(t_0)$, which yields a micromotion operator that equals the identity after each modulation period. With this choice, the time evolution operator simplifies to

$$\hat{U}\left(t, t_0\right) = \hat{U}'_{\mathrm{F}}\left(t, t_0\right) e^{-i\hat{H}^{t_0}_{\mathrm{F}}(t-t_0)/\hbar}, \tag{2.37}$$

with the Floquet Hamiltonian being

$$\hat{H}_{\mathrm{F}}(t_0) = \hat{U}_{\mathrm{F}}\left(t_0\right)\hat{H}_{\mathrm{eff}}\hat{U}^{\dagger}_{\mathrm{F}}\left(t_0\right). \tag{2.38}$$

This allows us to determine the time evolution of the system after one driving period according to

$$\hat{U}\left(t_0 + T, t_0\right) = e^{-i\hat{H}_{\mathrm{eff}}(t_0)T/\hbar}, \tag{2.39}$$

where the evolution of the system after $n \in \mathbb{N}$ driving periods can be determined by repeated application of the time evolution operator.

High frequency limit In most cases, an analytic derivation of the Floquet Hamiltonian $\hat{H}_F$ and of the micromotion operator $\hat{U}_F$ is not possible, but instead have to be derived numerically. For sufficiently large drive frequencies however, where the different Floquet copies are well separated, one can perform a perturbative expansion of the Hamiltonian by performing a Magnus expansion [86–88]. For this, the Hamiltonian is split into a time-independent part $\hat{H}_0$, and a time-dependent part $\hat{V}(t)$ oscillating with the drive frequency and harmonics:

$$\hat{H}(t) = \hat{H}_0 + \hat{V}(t) \tag{2.40}$$

$$\hat{V}(t) = \sum_{n=1}^{\infty} \hat{V}_n e^{in\omega t} + \hat{V}_{-n} e^{-in\omega t}. \tag{2.41}$$

Performing this expansion to first order yields

$$\hat{H}_F = \hat{H}_0 + \frac{1}{\hbar\omega}\sum_{n=1}^{\infty}\frac{1}{n}\left[\hat{V}_n, \hat{V}_{-n}\right] + \mathcal{O}\left(\frac{1}{(\hbar\omega)^2}\right). \tag{2.42}$$

In a similar fashion one can find an expression for the micromotion operator $\hat{U}_F$ [85, 88]. As we probe the system stroboscopically after full evolutions for the measurements presented in this thesis, we do not derive the expressions for this operator here.

2.3 The tunneling modulated honeycomb lattice

Ultracold atoms in optical lattices, being charge neutral, do not couple to magnetic fields via the Lorentz force, preventing the straighforward implementation of topological phases such as quantum Hall systems. Instead, several approaches have been developed to engineer complex tunneling amplitudes, most prominently laser-assisted tunneling [56, 57, 62, 89] or shaking of the lattice [59, 71].

In this work, we perform Floquet engineering by employing an amplitude modulation scheme, varying the optical potential of the three laser beams forming the optical lattice sinusodially. Similar behavior can however also be observed for stepwise driving protocols [90].

The scheme employed here is based on the optical lattice described in Sec. 3.3, where three free-running laser beams intersect at the location of the atoms and their cross-interference forms an optical lattice. One benefit of this setup is, that it allows variation of the tunneling along all three of the lattice directions independently. This way, one can realize a Hamiltonian varying the nearest neighbour tunneling,

$$\begin{aligned}\hat{H}\left(t\right) &= \sum_{j=1}^{3} \begin{pmatrix} 0 & J_j(t)e^{i\mathbf{k}\boldsymbol{\delta}_j} \\ J_j^*(t)e^{-i\mathbf{k}\boldsymbol{\delta}_j} & 0 \end{pmatrix} \\ &= \sum_{j=1}^{3} J_j(t)\left(\hat{\sigma}_x \cos\left(\mathbf{k}\boldsymbol{\delta}_j\right) + \hat{\sigma}_y \sin\left(\mathbf{k}\boldsymbol{\delta}_j\right)\right). \end{aligned} \tag{2.43}$$

Here $\boldsymbol{\delta}_j$ denites the position vector to the three nearest neighbours, as illustrated in Fig. 2.1. The first entry in the Hamiltonian corresponds to an A-site in the unit cell, and the second to a B-site.

The sinusoidal modulation of the beam potentials leads to a modulation of the tunneling according to

$$J_j(t) = A \cdot e^{B\cos\left(\omega t + \kappa j \frac{2\pi}{3}\right)} + C, \tag{2.44}$$

where for all measurements presented in this thesis $A = 0.220E_R$, $B = 0.767$, and $C = -0.065E_R$, with $E_R = h/(2\lambda_L^2 m_K) = h \cdot 9.23\,\mathrm{kHz}$ being the recoil energy of our optical lattice. The chirality $\kappa = \pm 1$ determines, in which order the three beams are modulated.

2.3.1 Behavior at high modulation frequencies

To determine the high-frequency behavior of our modulation scheme, one can perform a Magnus expansion [86–88], making use of Eq. 2.42:

$$\hat{H}_F = \hat{H}_0 + \frac{1}{\hbar\omega}\sum_{n=1}^{\infty}\frac{1}{n}\left[\hat{V}_n, \hat{V}_{-n}\right] + \mathcal{O}\left(\frac{1}{(\hbar\omega)^2}\right).$$

The zeroth-order term $\hat{H}_0$ represents the time-averaged Hamiltonian and can be evaluated as

$$\begin{aligned}\hat{H}_0 &= \sum_{j=1}^{3}\left(\frac{1}{T}\int_0^T J_j(t)\left(\hat{\sigma}_x\cos\left(\mathbf{k}\boldsymbol{\delta}_j\right)+\hat{\sigma}_y\sin\left(\mathbf{k}\boldsymbol{\delta}_j\right)\right)dt\right)\\ &= \sum_{j=1}^{3}(AI_0(B)+C)\left(\hat{\sigma}_x\cos\left(\mathbf{k}\boldsymbol{\delta}_j\right)+\hat{\sigma}_y\sin\left(\mathbf{k}\boldsymbol{\delta}_j\right)\right), \qquad (2.45)\end{aligned}$$

with I_0 being the modified Bessel function of the first kind. This Hamiltonian corresponds to a static honeycomb lattice with effective tunneling strength $J_{\text{eff},0} = AI_0(B) + C$.

To find an expression for $V_{\pm n}$, we perform a Jacobi-Anger expansion of the tunneling amplitude

$$\begin{aligned}J_j(t) &= Ae^{B\cdot\cos\left(\omega t+\kappa j\frac{2\pi}{3}\right)}+C\\ &= A\left(I_0(B)+2\sum_{m=1}^{\infty}I_m(B)\cos\left(m(\omega t+\kappa j\frac{2\pi}{3})\right)\right)+C. \qquad (2.46)\end{aligned}$$

This expansion allows us to identify the amplitude $\hat{V}_{\pm 1}$ of the first-order time dependent part

$$\hat{V}_{\pm 1} = AI_1(B)\sum_{j=1}^{3}e^{\pm i\kappa j\frac{2\pi}{3}}\left(\hat{\sigma}_x\cos\left(\mathbf{k}\boldsymbol{\delta}_j\right)+\hat{\sigma}_y\sin\left(\mathbf{k}\boldsymbol{\delta}_j\right)\right). \qquad (2.47)$$

Substituting this into the first-order term of Eq. 2.42, one obtains

$$\begin{aligned}\hat{H}_1 &= \frac{1}{\hbar\omega}\left[\hat{V}_1,\hat{V}_{-1}\right]\\ &= \frac{1}{\hbar\omega}\left(AI_1(B)\right)^2\sum_{j,k=1}^{3}e^{i\kappa(j-k)\frac{2\pi}{3}}\left[\left(\hat{\sigma}_x\cos\left(\mathbf{k}\boldsymbol{\delta}_j\right)+\hat{\sigma}_y\sin\left(\mathbf{k}\boldsymbol{\delta}_j\right)\right),\left(\hat{\sigma}_x\cos\left(\mathbf{k}\boldsymbol{\delta}_k\right)+\hat{\sigma}_y\sin\left(\mathbf{k}\boldsymbol{\delta}_k\right)\right)\right]\\ &= \frac{1}{\hbar\omega}\left(AI_1(B)\right)^2\sum_{j,k=1}^{3}e^{i\kappa(j-k)\frac{2\pi}{3}}2i\sigma_z\sin\left(\mathbf{k}(\boldsymbol{\delta}_k-\boldsymbol{\delta}_j)\right)\\ &= -\frac{1}{\hbar\omega}2\sqrt{3}\left(AI_1(B)\right)^2\sigma_z\sum_{j=1}^{3}\sin\mathbf{k}\cdot\mathbf{a_j}, \qquad (2.48)\end{aligned}$$

where we have used the Pauli matrix commutation relations and performed the geometric sum over the lattice vectors. Combining the zeroth- and first-order contributions, we arrive at the effective Floquet Hamiltonian

$$\begin{aligned}\hat{H}_F =& \sum_{j=1}^{3}(AI_0(B)+C)\left(\hat{\sigma}_x \cos\left(\mathbf{k}\boldsymbol{\delta}_j\right)+\hat{\sigma}_y \sin\left(\mathbf{k}\boldsymbol{\delta}_j\right)\right) \\ & -\frac{\kappa}{\hbar\omega} 2\sqrt{3}\left(AI_1(B)\right)^2 \sigma_z \sum_{j=1}^{3} \sin \mathbf{k}\cdot\mathbf{a_j}. \end{aligned} \tag{2.49}$$

Comparing this Hamiltonian to the Haldane model as defined in Eq. 2.21 we observe that our Floquet-engineered system realizes a Haldane-type Hamiltonian with zero sublattice offset $\Delta = 0$, a next-nearest neighbor tunneling amplitude $t = \frac{\sqrt{3}(AI_1(B))^2}{\hbar\omega}$, and a next-nearest neighbor tunneling phase $\phi = -\kappa\pi/2$.

2.4 Anomalous Floquet Phases

In the past sections, we have considered Floquet engineering mainly in the limit of the driving frequency being the largest energy scale in the system. Here, the dynamics over long timescales can be be accurately described by a static, effective Hamiltonian $\hat{H}_{\text{eff}}$, which can be derived via a Magnus expansion (as discussed in Sec. 2.3 and Sec. 2.2) [85]. If the driving frequency of the system is reduced, however, the system can no longer be described by a time-independent Hamiltonian $\hat{H}_{\text{eff}}$. These genuine out-of-equilibrium systems are known as anomalous Floquet phases. Such phases have been experimentally realized in a range of different platforms, such as photonic waveguides [76, 91, 92], nanophotonic lattices [93, 94], microwave- [95, 96] and acoustic resonators [97], liquid crystal devices [98] as well as in ultracold quantum gases in optical lattices [61].

The schematic band structure of an anomalous Floquet system is, together with the band structure of a Chern insulator, illustrated in Fig. 2.2. Anomalous Floquet phases rely on the periodicity of the energy spectrum, as they emerge when different Floquet copies of the system can hybridize. They realize a topologically trivial bulk, while exhibiting edge modes in all energy gaps of the system [65, 99]. This however means, that the Chern number is no longer suitable to characterize the topological properties of the system: As the energy spectrum has no lower bound, with any band of the system having an edge mode entering from the bottom and exiting from the top, all Chern numbers vanish, with the system still exhibiting topologically nontrivial behavior.

To properly characterize the topological properties of such anomalous Floquet phases, a different invariant is required. Instead, the topological invariant in anomalous Floquet systems is the winding number at quasienergy ϵ [65]

$$W_\epsilon\left(\hat{U}_\epsilon\right) = \frac{1}{8\pi^2}\int_0^T dt \int_{\text{BZ}} dk_x dk_y \text{Tr}\left(\hat{U}_\epsilon^{-1}\partial_t \hat{U}_\epsilon \left[\hat{U}_\epsilon^{-1}\partial_{k_x}\hat{U}_\epsilon, \hat{U}_\epsilon^{-1}\partial_{k_y}\hat{U}_\epsilon\right]\right). \tag{2.50}$$

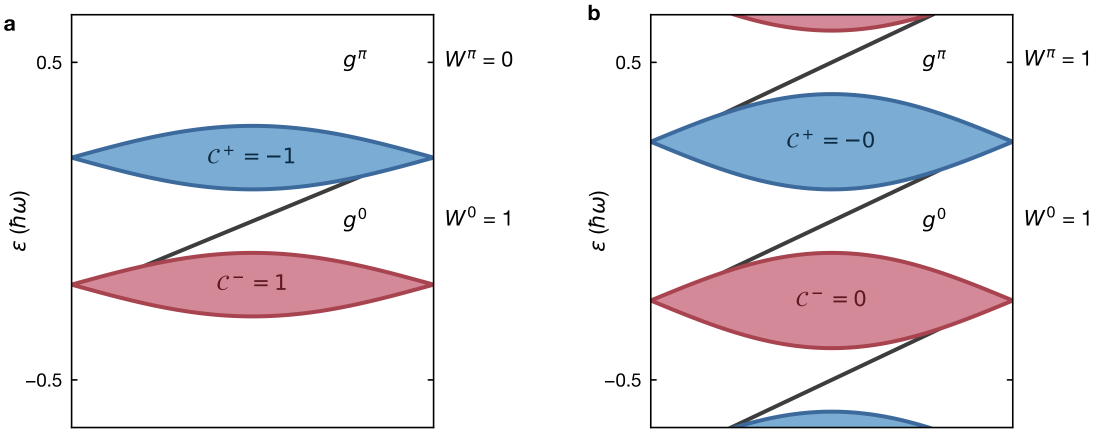

Figure 2.2 | Schematic energy spectrum of a Chern insulator and an anomlous Floquet system. **a** Schematic energy spectrum in a Chern insulator: There is only one edge mode in the 0-gap g^0 of the system. Because of this, the bands have nonzero Chern numbers $\mathcal{C}^- = 1$ and $\mathcal{C}^+ = -1$. **b** In an anomalous Floquet system, the bands of the different Floquet copies hybridized, leading to edge states both in the 0-gap g^0 as well as in the π-gap g^π of the system. Because of this, the Chern number of both bands are zero. Instead, one can use the winding numbers $W^0 = 1$ and $W^\pi = 1$ in the 0-gap and in the π respectively to characterize the system.

This expression integrates over the Brillouin zone for a full driving period, quantifying the nontrivial topology of the system by measuring how the eigenstates of the time-evolution operator $\hat{U}_\epsilon$ evolve as one traverses the Brillouin zone. Here, the net number of edge states at quasienergy ϵ is directly given by the winding number

$$n_{\text{edge}} = \left| W_\epsilon \left(\hat{U}_\epsilon \right) \right| . \tag{2.51}$$

A nonzero winding number at a particular quasienergy thus guarantees the presence of topologically protected edge states at that energy. This way, the Chern number of a band situated between quasienergies ϵ and ϵ' can be calculated according to

$$\mathcal{C}_{\epsilon',\epsilon} = W'_\epsilon \left(\hat{U}_\epsilon \right) - W_\epsilon \left(\hat{U}_\epsilon \right) . \tag{2.52}$$

An anomalous Floquet system can also be realized in our tunneling-modulated honeycomb lattice, as was investigated in [61]. To illustrate this transition, the dispersion of the lattice is numerically simulated, with results displayed in Fig. 2.3. Here, the 2D dispersion as well as the dispersion along the high-symmetry line Γ-M-K-Γ are simulated using the modulation scheme introduced in Sec. 2.3. To better illustrate the phase transition into the anomalous regime, the system is also simulated on a semi-infinite strip, where the system is periodic in x-direction, while it is terminated at the zig-zag edge in y-direction. This leads to edge

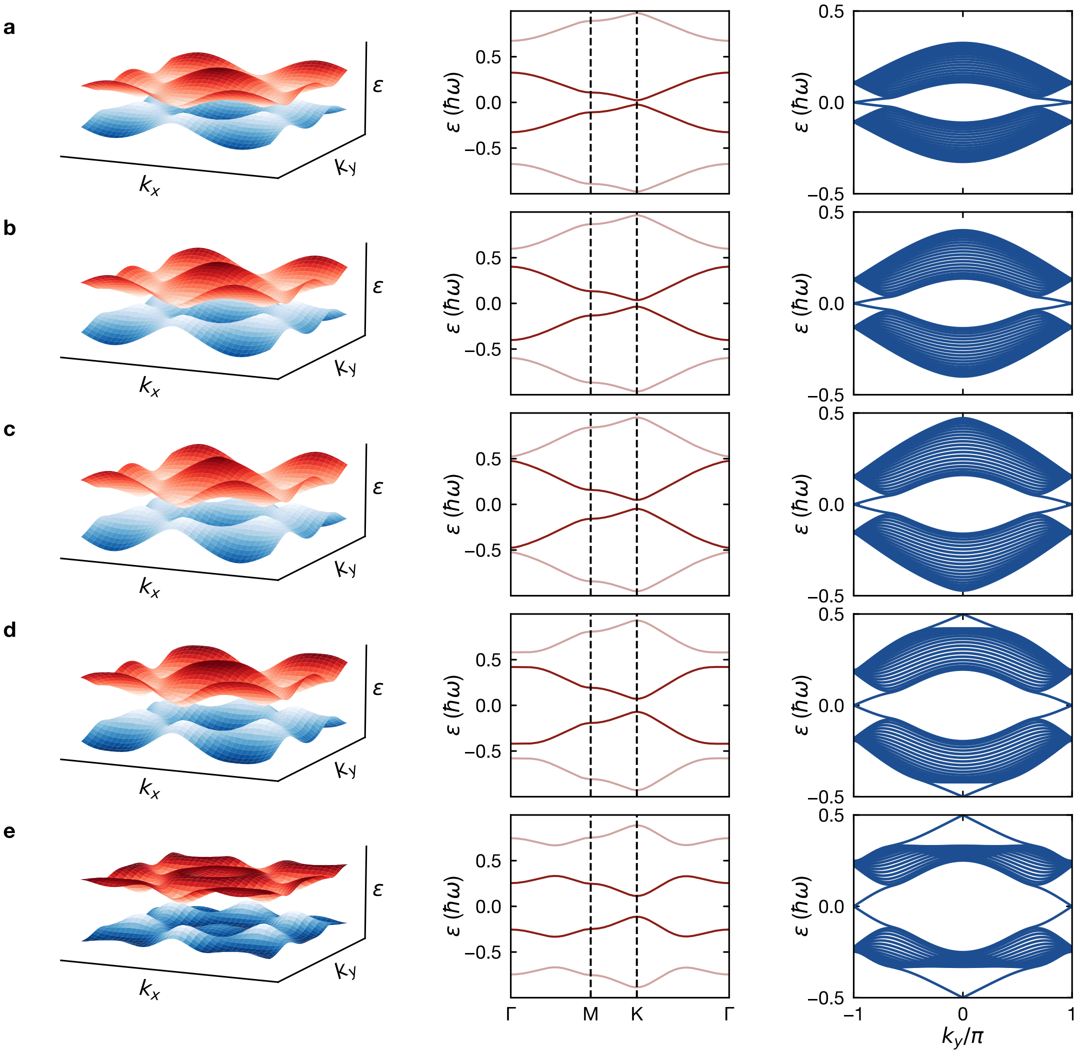

Figure 2.3 | Dispersion at the transition into the anomalous regime for the tunneling-modulated honeycomb lattice. From left to right, each subfigure shows the 2D bandstructure, the dispersion along the high symmetry-points Γ-*M*-*K*-Γ, and the dispersion on a semi-infinite strip, where the system is periodic in x-direction, and terminated at the numerical zig-zag edge in y-direction. In the high-symmetry line plot, the dispersion of the Floquet copies is shown using a lighter shade to illustrate the gap closing in the π-gap at Γ. The subfigures show **a** $\omega/(2\pi) = 16\,\mathrm{kHz}$, **b** $\omega/(2\pi) = 13\,\mathrm{kHz}$, **c** $\omega/(2\pi) = 11\,\mathrm{kHz}$, **d** $\omega/(2\pi) = 9\,\mathrm{kHz}$, **e** $\omega/(2\pi) = 7\,\mathrm{kHz}$.

states propagating along both numerical edges of the system, visible as two edge states, one with positive and the other with negative slope.

As discussed in Sec. 2.3.1, this system maps to a Haldane model with $\Delta = 0$ and $\psi = -\kappa\pi/2$ in the high frequency limit. We start our investigation in subfigure **a** at a modulation frequency significantly larger than the bandwidth, $\omega/(2\pi) = 16\,\mathrm{kHz}$, such that the different

Floquet copies are well separated, and no coupling between them is present. This frequency was chosen, as it is the one commonly used in our experiments, having both a relatively large π- and 0-gap (with the size of the 0-gap decreasing for larger modulation frequencies). One can see, that while the chiral modulation of the system leads to a gap opening at the K-points of the system, the dispersion is otherwise mostly identical to the dispersion of the unmodulated lattice.

If the modulation frequency is reduced, as illustrated in subfigures **b** and **c**, the size of the Floquet Brillouin zone is reduced, moving Floquet copies closer together in the π-gap. At $\omega/(2\pi) = 11\,\mathrm{kHz}$, the bands are just shy of touching each other at the Γ-point. Reducing the modulation frequency now even further, as illustrated in **d** and **e**, the upper band in the Floquet Brillouin zone starts to couple with the lower band of the upper Floquet copy, and vice versa. This leads to a deformation of the bands, originating at Γ, which gets stronger with reducing modulation frequency. At this point, one can also see an edge state in the π-gap originating at the band touching point, connecting the Floquet copies across the gap. This marks the transition from the Haldane- into the anomalous Floquet regime, changing the winding numbers of the two bands from $W^0 = 1$, $W^\pi = 0$ to $W^0 = 1$, $W^\pi = 1$.

If after this point the modulation freqeuncy is reduced even further after this point, a second transition into a regime with $W^0 = 0$, $W^\pi = 1$ can be observed, due to the bands touching at the Γ-point once again. This phase is usually referred to as the Haldane-like regime, as its properties are closely related to those in the Haldane regime.

Another feature of interest for future experiments can be seen in Fig. 2.3**e** for a modulation frequency $\omega/(2\pi) = 7\,\mathrm{kHz}$: Here, in the 2D bandstructure, a moat structure is visible, centered around Γ, similar to the one realized in [100], which might open a pathway towards the realization of a chiral spin liquid [101, 102].

2.5 Disordered systems

Material properties in disordered systems have long been an active field of research. A significant catalyst here was the discovery of the integer Quantum Hall Effect (QHE) [5–7], which relies on some degree of disorder to localize the bulk of the system while leaving a few extended states free to carry the quantized current along the edge.

The field of quantum simulation with ultracold atoms poses a natural choice for investigating such effects, as clean systems are easily obtained, and disorder can be reintroduced in a controlled manner – most notably in experiments on Anderson localization [103–107]. The extension of this research into systems realizing topological Bloch bands holds the opportunity for generating a better understanding of the robustness of topological protection, and of exotic phases like the anomalous Floquet Anderson insulator [66, 108]. Additional investigations of the effect disorder has on the phase diagram of such systems might deepen the understanding of the interplay between topology and disorder [109].

2.5.1 Transport in disordered media

On a simple level, particle transport can be understood via the Drude model, which provides a description of particle motion in the presence of scattering. The model assumes that particles travel ballistically at constant velocity v between instantaneous scattering events. These events occur randomly, with mean free time τ and a corresponding mean free path $\ell = v\tau$ between collisions. Upon scattering, the particle's direction is randomized isotropically. These microscopic processes can be linked to macroscopic diffusion, described by the diffusion coefficient

$$D = \frac{1}{d} v\ell = \frac{1}{d} v^2 \tau, \tag{2.53}$$

where d is the dimensionality of the system. By formulating a continuity equation for particle flow and by making use of Fick's law, one can now derive the probability density [4]

$$P(\mathbf{r}, t) = (4\pi D t)^{-d/2}\, e^{r^2/(4Dt)}, \tag{2.54}$$

assuming $r(t = 0) = 0$, yielding a Gaussian distribution. A useful metric for quantifying the extent of this distribution is the mean squared displacement

$$\langle r^2(t) \rangle = \int r^2 P(r, t)\, dr = 2dDt, \tag{2.55}$$

growing linearly in time, with a slope dependent on the dimensionality of the system.

This model effectively describes transport in systems, where interference effects remain negligible, i.e. when the coherence length is much shorter than the mean free path ℓ. According to this description, transport persists regardless of the amount of disorder, albeit with reduced mobility.

When the coherence length extends over multiple scattering events, one however needs to consider the acquired phases of all possible paths between two points, illustrated in Fig. 2.4a. This means, that the wave function at location $\mathbf{r}$ – again assuming expansion from $r = 0$ – has to be expressed as a Feynman path integral

$$|\psi(\mathbf{r}, t)\rangle = \int \mathcal{D}\mathbf{x}(t') e^{i\, S[\mathbf{x}(t')]/\hbar}, \tag{2.56}$$

with $\mathbf{x}$ being a path from 0 to $\mathbf{r}$, $S\left[\mathbf{x}(t')\right]$ its classical action, and $\mathcal{D}\mathbf{x}(t')$ being the integration measure, ensuring normalization [4]. In the semiclassical limit, considering only paths along which S is stationary, this simplifies to

$$\psi(\mathbf{r}, t) \approx \frac{1}{N} \sum_{j=1}^{N} e^{i\phi_j(t)}, \tag{2.57}$$

with N being the number of classical paths, and ϕ_j the phase acquired along path j. Assuming these phase differences to be uncorrelated due to the strong dependence of

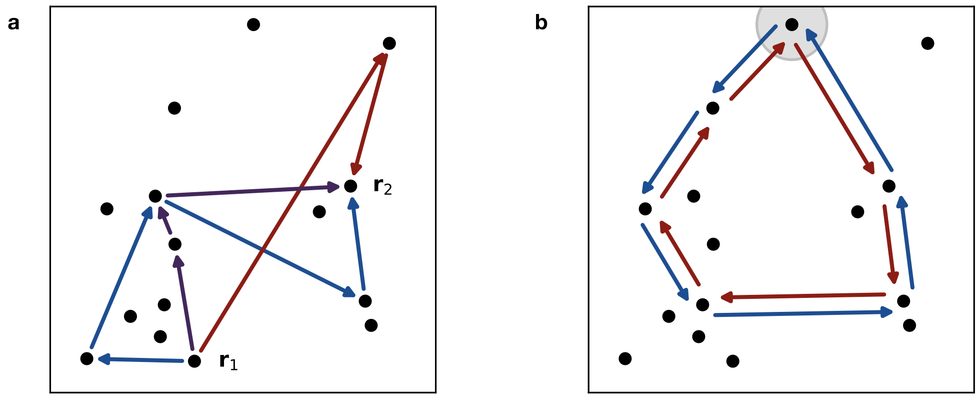

Figure 2.4 | **Coherence effects and weak localization.** **a** When the coherence length of the particle's phase extends over multiple scattering events, the coherent sum across all possible paths has to be determined to determine the probability of scattering from location $\mathbf{r}_1$ to $\mathbf{r}_2$. **b** Weak localization: The path length difference for paths traversed in opposite directions is zero. This way, constructive interference increases the probability of a particle returning to its initial location (encircled).

the acquired phase on the path taken, one can recover classical diffusion, as defined in Eq. 2.54. However, this is not true, with one of the strongest corrections to this being illustrated in Fig. 2.4b: For each path, there must exist a second path which acquires the same phase, in which the path is traversed in reverse. For closed paths, winding from a location $\mathbf{r}'$ back to location $\mathbf{r}'$, both paths having the same start- and end point, leading to constructive interference, which modifies Eq. 2.57 to

$$\psi(\mathbf{r}', t) \approx \frac{1}{N} \sum_{j=1}^{N/2} 2e^{i\phi_j(t)}, \tag{2.58}$$

with N still being the total number of paths, and j summing over all unique paths, e.g. all paths traversing clockwise. By comparing this to Eq. 2.57, one can see that due to the pairwise coherent addition of paths, the amplitude of the wave function is twice as large, leading to an increased average return probability, which is exactly twice the classically expected return probability [4]:

$$\overline{|\psi(\mathbf{r}', t)|^2} = 2(4\pi D t)^{-d/2}. \tag{2.59}$$

This effect is known as weak localization, as it diminishes the ability of a wave to travel through a disordered medium. In condensed matter experiments, it is responsible for the anomalous resisitance of thin metallic films [110, 111], where its effect can be probed by applying a magnetic field to dephase counter-propagating paths [112].

A similar effect can be observed in reciprocal space, where a state at quasimomentum $\mathbf{k}$ has an increased probability of scattering into a state at quasimomentum $-\mathbf{k}$, known as coherent back scattering. This effect together with the doubling of the probability of scattering back was first experimentally observed in pumped titanium-sapphire powder, and has since been observed with ultracold atoms [113].

Interference effects can even halt diffusion altogether, leading to so-called strong, or Anderson localization [114]. This type of localization strongly depends on the dimensionality of the system [115], which can be intuitively understood by considering the increased probability of scattering back towards the initial state for lower dimensional systems, increasing the strength of interference effects. This way, in a one-dimensional system of infinite size, all states in a disorder potential localize independent of the strength of the disorder. In two-dimensional systems, states of all energies still localize, but the region occupied by the localized states increases exponentially with energy, eventually reaching the system size. In 3D systems, a phase transition exists at an energy E_C, the so-called mobility edge, below which states are localized, while states above the mobility edge are extended.

In topologically nontrivial materials, the bulk-boundary correspondence ensures the existence of topological edge modes, as long as the disorder does not close the bulk gap or break the underlying protecting symmetry. The mechanism behind this topological protection can be understood by considering the processes leading to localization, such as coherent backscattering: As in the edge mode no counterpropagating channels to scatter into exist, the edge states stay conductive even in the presence of moderate disorder. This protection is not absolute, and sufficiently strong disorder can close the bulk band gap, driving the system into a topologically trivial state.

While disorder can break transport by closing energy gaps, it can also lead to the emergence of topological nontrivial phases. Here, the topological Anderson insulator [73], realized in [74, 76–78], serves as an example, where the application of disorder can drive an initially trivial system into a nontrivial phase, exhibiting topologically protected edge states. This underlines, how further investigations of the effect disorder has on topological materials are necessary to fully understand such systems.

2.5.2 The Bott index

In disordered systems, lacking translational invariance, conventional topological invariants, which rely on a well-defined quasi momentum, typically fail. The Bott index [116] probes the system in real space, quantifying whether topological features prevent the existence of a set of localized wavefunctions spanning a band's eigenspace. To this end, the commutativity of the projected position operators is evaluated, quantifying the extent to which they fail to commute.

To evaluate the Bott index, we consider a rectangular system consisting of N_s lattice sites, shaped $L_x \times L_y$, and periodic boundary conditions. For such a system, the Bott index $\mathcal{B}$ is then defined as

$$\mathcal{B} = \frac{1}{2\pi i}\mathrm{Tr}\left[\log\left(\hat{U}_x\hat{U}_y\hat{U}_x^\dagger\hat{U}_y^\dagger\right)\right]. \tag{2.60}$$

Here the unitary operators $\hat{U}_x$ and $\hat{U}_y$ are defined as

$$\begin{aligned}\hat{U}_x &= \hat{P} e^{2\pi i \hat{X}/L_x} \hat{P} + (\mathbb{I} - \hat{P}) \\ \hat{U}_y &= \hat{P} e^{2\pi i \hat{Y}/L_y} \hat{P} + (\mathbb{I} - \hat{P}),\end{aligned} \tag{2.61}$$

with $\hat{X}$ and $\hat{Y}$ being the position operators, and $\hat{P} = \sum_{n \in \text{occupied}} |\psi_n\rangle \langle\psi_n|$ being the projection operator onto the occupied states.

Thermodynamic limit of the Bott index In the limit of very large system sizes, $\hat{U}_x$ and $\hat{U}_y$ can be expanded to leading order,

$$\begin{aligned}\hat{U}_x &\approx \hat{P} \left(\mathbb{I} + \frac{2\pi i}{L_x} \hat{X} \right) \hat{P} + (\mathbb{I} - \hat{P}) \\ \hat{U}_y &\approx \hat{P} \left(\mathbb{I} + \frac{2\pi i}{L_y} \hat{Y} \right) \hat{P} + (\mathbb{I} - \hat{P}).\end{aligned} \tag{2.62}$$

Evaluating the argument in the logarithm in Eq. 2.60 to leading order in $1/(L_x L_y)$ yields then

$$\hat{U}_x \hat{U}_y \hat{U}_x^\dagger \hat{U}_y^\dagger \approx \mathbb{I} + \frac{(2\pi i)^2}{L_x L_y} \hat{P} \left[\hat{X}, \hat{Y} \right] \hat{P}. \tag{2.63}$$

Plugging that back into Eq. 2.60

$$\mathcal{B} = \frac{1}{2\pi i} \mathrm{Tr} \left[\log \left(\mathbb{I} + \frac{(2\pi i)^2}{L_x L_y} \hat{P} \left[\hat{X}, \hat{Y} \right] \hat{P} \right) \right] \tag{2.64}$$

and applying $\log(1 + x) \approx x$ for small x, one obtains

$$\mathcal{B} = \frac{2\pi i}{L_x L_y} \mathrm{Tr} \left(\hat{P} \left[\hat{X}, \hat{Y} \right] \hat{P} \right). \tag{2.65}$$

In a entirely clean system, exhibiting translational invariance, we can assume periodic boundary conditions, and work in the Bloch basis. The position operators in momentum space then become

$$\hat{X} = i \frac{\partial}{\partial k_x} \qquad \hat{Y} = i \frac{\partial}{\partial k_y}. \tag{2.66}$$

The projector onto occupied bands can be written as

$$\hat{P} = \sum_{n \in \text{occupied}} \int_{BZ} \frac{d\mathbf{k}}{(2\pi)^2} |u_{\mathbf{k}}^n\rangle \langle u_{\mathbf{k}}^n|, \tag{2.67}$$

with $|u_{\mathbf{k}}^n\rangle$ being the Bloch functions. This allows us to rewrite the trace in Eq. 2.65 as

$$\mathrm{Tr}\left(\hat{P}\left[\hat{X},\hat{Y}\right]\hat{P}\right)=\sum_{n\in\mathrm{occupied}}\int_{BZ}d\mathbf{k}\,\frac{L_xL_y}{(2\pi)^2}\,i\left\langle u_{\mathbf{k}}^{n}\right|\left[\partial_{k_x},\partial_{k_y}\right]\left|u_{\mathbf{k}}^{n}\right\rangle\left\langle u_{\mathbf{k}}^{n}\right|\left|u_{\mathbf{k}}^{n}\right\rangle, \tag{2.68}$$

with

$$\begin{aligned}i\left\langle u_{\mathbf{k}}^{n}\right|\left[\partial_{k_x},\partial_{k_y}\right]\left|u_{\mathbf{k}}^{n}\right\rangle&=i\left(\left\langle\partial_{k_x}u_{\mathbf{k}}^{n}\right|\left|\partial_{k_y}u_{\mathbf{k}}^{n}\right\rangle-\left\langle\partial_{k_y}u_{\mathbf{k}}^{n}\right|\left|\partial_{k_x}u_{\mathbf{k}}^{n}\right\rangle\right)\\&=i\left\langle\nabla_{\mathbf{k}}u_{\mathbf{k}}^{n}\right|\times\left|\nabla_{\mathbf{k}}u_{\mathbf{k}}^{n}\right\rangle\\&=\Omega_n\left(\mathbf{k}\right)\end{aligned} \tag{2.69}$$

being the Berry curvature, as defined in Eq. 2.9. Plugging this back into Eq. 2.65 yields

$$\mathcal{B}=\frac{1}{2\pi}\sum_{n\in\mathrm{occupied}}\int_{BZ}d\mathbf{k}\,\Omega_n\left(\mathbf{k}\right). \tag{2.70}$$

By comparing this to the definition of the Chern number in Eq. 2.11, one immediately sees that the Bott index is equal to the sum of the Chern numbers of all occupied bands for large, disorder-free systems,

$$\mathcal{B}=\sum_{n\in\mathrm{occupied}}\mathcal{C}^{n}. \tag{2.71}$$

CHAPTER 3

Experimental setup

This chapter provides an overview of the experimental platform utilized for the measurements presented in this thesis, with an emphasis on recent upgrades. Here, the focus lies on giving a broad overview over the platform, while providing details on recent additions to the setup. The fundamental platform is described in greater detail in [117, 118], with more recent changes to it being described in [119–122].

The chapter begins in Sec. 3.1 by providing details on the experimental steps and the tools used for creating a Bose-Einstein condensate (BEC) of ^{39}K, going throug the initial laser cooling steps, the magnetic transport, and the evaporative cooling stage. In the following, the optical trapping potentials used in the experiment are described: Sec. 3.2.1 describes the setup generating the crossed optical dipole trap, and Sec. 3.2.2 provides information on the optical tweezer trap we implemented. To project arbitrary binary repulsive potentials into the atomic plane, we have implemented a digital micromirror device (DMD) into the experimental setup, described in Sec. 3.2.3. Lastly, we have added a speckle beam to the setup, which enables us to project repulsive disorder into the atomic plane, with information provided in Sec. 3.2.4. Following this, Sec. 3.3 presents the optical lattice setup used, and how it can be utilized to measure the band gap of a system. The chapter concludes in Sec. 3.4 with a description of our absorption imaging system, providing details on the improved in-situ imaging capabilities in Sec. 3.4.1, and on its calibration to account for saturation effects in Sec. 3.4.2.

3.1 Generating a Bose-Einstein condensate

The experiments described in the following chapters have been performed using a Bose-Einstein condensate (BEC) of ^{39}K, as it has a wide Feshbach resonance accessible at 403 G. While our experimental setup in general is also able to create BECs of ^{87}Rb, only the generation of BECs of ^{39}K, using ^{87}Rb for sympathetic cooling, is discussed.

3.1.1 Atom loading and laser cooling

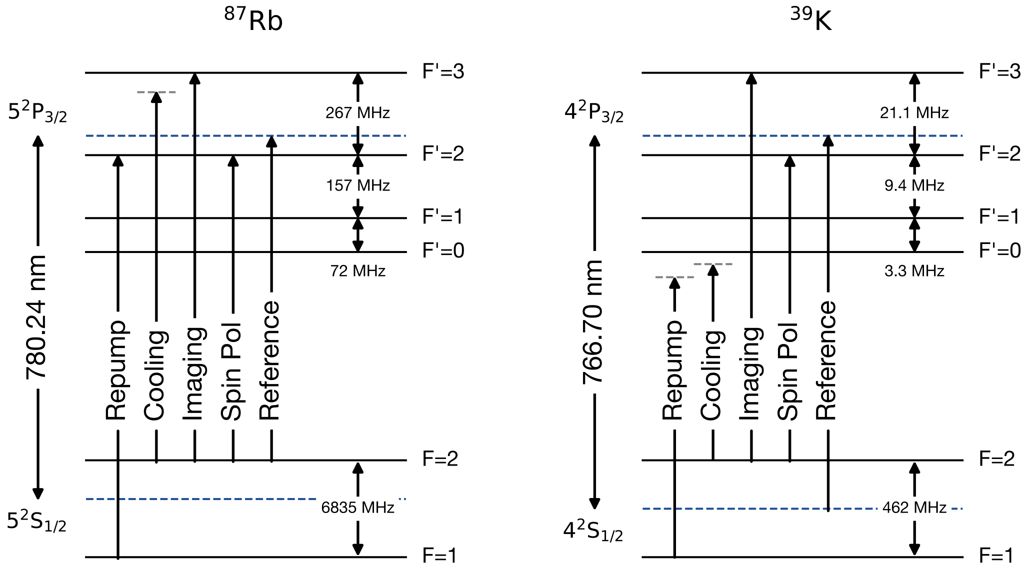

Figure 3.1 | Hyperfine structure of the D_2 lines for ^{87}Rb and ^{39}K. The diagram indicates the laser frequencies used for cooling ^{87}Rb and ^{39}K, with detunings marked by grey dashed lines and crossover resonances by blue dashed lines. The frequencies for the imaging system at large magnetic fields are discussed in Sec. 3.4.1. Data is sourced from [123, 124].

The experimental sequence begins with loading both ^{87}Rb and ^{39}K from the background pressure in a dual-species two-dimensional magneto-optical trap (2D MOT). In this stage, two pairs of red-detuned, circularly polarized laser beams provide transverse cooling, while a magnetic quadrupole field confines the atoms along the transversal direction [125]. For ^{39}K, an additional retro-reflected beam provides axial cooling, forming a 2D$^+$-MOT configuration [126]. Here, a mirror combined with a waveplate with a hole drilled in the center is reflecting back the beam, with the hole allowing atoms to travel to the differential pumping tube leading to the 3D MOT chamber, providing some additional axial cooling on the outer regions of the system, while pushing them into the differential pumping section in the inner (cooler) region. This differential pumping section generates a pressure gradient, maintaining a pressure of $\approx 1 \times 10^{-9}$ mbar in the 3D MOT chamber. For ^{87}Rb, a resonant laser beam is used to push the atoms from the 2D MOT chamber to the 3D MOT. Here, the atoms are cooled by three pairs of red-detuned, circularly polarized beams in combination with a magnetic quadrupole field [127–129]. Typical loading times are 2.5 s for rubidium, and $\approx$ 0.3 s for potassium, the latter being regularly optimized for the final ^{39}K BEC atom number.

Following the loading phase, the magnetic field gradient is increased to compress the cloud [130]. Subsequently, the magnetic field is turned off, and the laser detuning is increased to perform molasses cooling on both species [127, 129, 131].

3.1.2 Magnetic transport

The BEC is generated in the science chamber, which is separated by another differential pumping section. To transport the atomic cloud there, we employ a magnetic transport system [132]. As at the end of the molasses the atomic cloud ends up in a mixture of spin states, we optically pump both species into the $|F = 2, m_F = 2\rangle$ state before starting the transport.Then, a series of overlapping coil pairs in anti-Helmholtz configuration generate a moving quadrupole potential, which pulls the atoms through the differential pumping tube.

The differential pumping tube we transport through consists of two straight sections, connected under a 45° angle. This prevents direct line of sight between the 3D MOT and the science chamber, and thus helps with obtaining pressures $\sim 7 \times 10^{-12}$ mbar in the science chamber. The final coil pair of the magnetic transport system also serves as a strong magnetic quadrupole trap to hold the atoms after the transport. To prevent Majorana losses [133, 134], a blue-detuned laser at 760 nm blocks the atoms from entering the central region of the trap.

3.1.3 Evaporative cooling and Feshbach resonances

The final cooling to a BEC involves several stages. First, while the atoms are held in the magnetic quadrupole trap, we perform forced microwave evaporation on ^{87}Rb [135–137]: The energy levels of the rubidium atoms experience a Zeeman shift, which allows us to drive the transition $|F = 2, m_F = 2\rangle$ to the antitrapped state $|F = 1, m_F = 1\rangle$ position selectively. As the outermost regions of the cloud, which experience the largest magnetic field, will be populated by the hottest atoms, we can perform a sweep of the microwave frequency to always match the transition frequency of the hottest atoms remaining in the system. The potassium atoms in the quadrupole trap are unaffected by this microwave field, but are sympathetically cooled by the rubidium atoms [138].

To reach lower temperatures after this step, we transfer the atoms into a crossed optical dipole trap [49] (cf. Sec. 3.2.1) by ramping down the magnetic quadrupole field, and simultaneously ramping up the dipole trap power. We apply a small magnetic bias field during the last 70 ms of the quadrupole rampdown to provide a quantization axis, keeping the atoms spin-polarized. To prevent spin-changing collisions [139] in the subsequent evaporation, we transfer both ^{87}Rb and ^{39}K into their absolute ground state $|F = 1, m_F = 1\rangle$, using a microwave sweep for rubidium, and a radio frequency sweep for potassium. Atoms that remain in $|F = 2, m_F = 2\rangle$ are removed using a pulse of resonant light.

After the transfer of the atoms into the optical dipole trap, the current in the magnetic field coils is ramped up again, now providing a homogeneous magnetic field in the Helmholtz configuration. This allows us to tune the scattering length, both between ^{87}Rb and ^{39}K atoms, as well as between different atoms of ^{39}K by employing Feshbach resonances.

A Feshbach resonance occurs, when the energy of a molecular bound state is close to the energy of an open channel, where the atoms are not bound, allowing the states to couple, and influence the scattering properties of the atoms [38, 39]. As these two channels

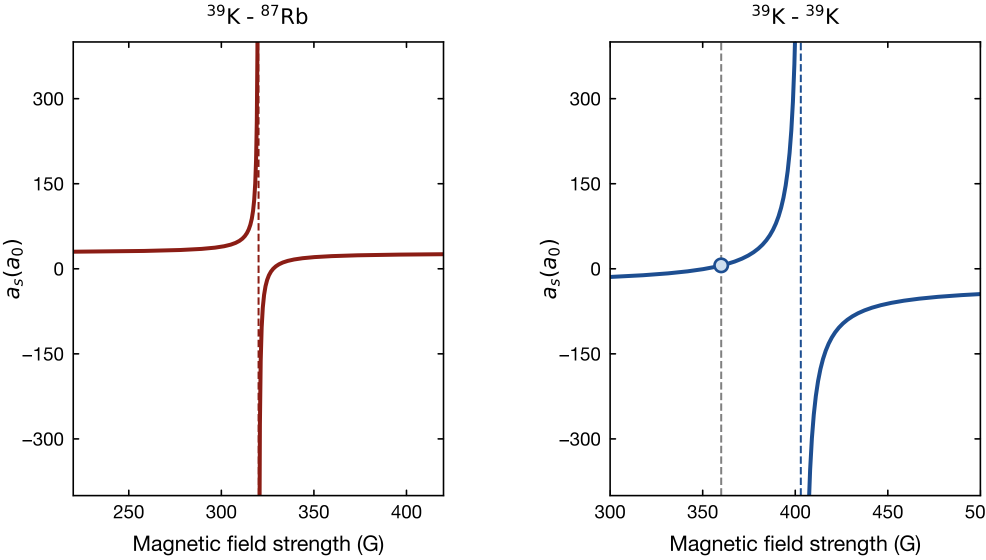

Figure 3.2 | Feshbach resonances employed in the experimental sequence. Inter-species scattering length in the vicinity of the Feshbach resonance between ^{87}Rb and ^{39}K at $B_0 = 320.1$ G, with a background scattering length $a_{bg} = -27.9a_0$ and a width $\Delta = 7.9$ G (left), as well the intra-species scattering length near the Fesbach resonance in ^{39}K at $B_0 = 403.3(7)$ G, with background scattering length $a_{bg} = -29a_0$ and width $\Delta = -52$ G (right). The grey dashed line in the right plot marks, together with the data point, the location at which the scattering length is $a_s = 6a_0$, as used for the measurements presented in Chapter 4 and Chapter 5 of this thesis.

typically have different magnetic moments, this condition can be realized by tuning the magnetic field. Near a Feshbach resonance, the s-wave scattering lengt between the involved atoms can be described as

$$a_s(B) = a_{bg}\left(1 - \frac{\Delta}{B - B_0}\right), \tag{3.1}$$

with a_{bg} being the background scattering length, Δ the width of the Feshbach resonance, and B_0 being its locations. The s-wave scattering length in the vicinity of the two Feshbach resonances we employ for our experiments is displayed in Fig. 3.2.

First, we utilize the inter-species Feshbach resonance [38, 39] of ^{87}Rb and ^{39}K at 320.1 G [140] to increase the scattering length to $\approx 90a_0$, which enhances the sympathetic cooling, and allows us to force the evaporation by ramping down the dipole trap. As the mass of ^{87}Rb is over two times the mass of ^{39}K, the gravitational sag leads to a weaker confinement of rubdium, so that at the end of this ramp nearly all rubidium atoms evaporated from the trap. Now, we make use of the interspecies Feshbach resonance of ^{39}K at 403.3(7) G [141] for both involved atoms in $|F = 1, m_F = 1\rangle$, decreasing the scattering length from $\approx 150a_0$ to $\approx 44a_0$ while slowly ramping down the dipole trap further. At the end of the ramp, we obtain an almost pure BEC of $\approx 2 \times 10^5$ atoms.

3.2 Optical potentials

3.2.1 Optical dipole trap

The optical dipole trap is formed by two intersecting beams with a wavelength $\lambda_{\text{dip}} = 1064\,\text{nm}$, which is far red-detuned from both the D_1 and the D_2 lines of ^{87}Rb and ^{39}K. The resulting attractive potential, V_{dip}, is proportional to the local intensity of the light field, $I(\mathbf{r}, t)$, as described by the relation [49]

$$V_{\text{dip}} = \frac{\pi c^2}{2} \left(\frac{\Gamma_{D_1}}{\omega_{D_1}^3} \frac{2 + g_F m_F \mathcal{P}}{\Delta_{D_1}} + \frac{\Gamma_{D_2}}{\omega_{D_2}^3} \frac{2 + g_F m_F \mathcal{P}}{\Delta_{D_2}} \right) I(\mathbf{r}, t), \tag{3.2}$$

where c is the speed of light, Γ is the natural linewidth of the transition under consideration, ω is its angular frequency, g_F is the Landé factor, m_F the magnetic quantum number, $\mathcal{P}$ describes the polarization of the trapping light, and Δ is its detuning from the transition under consideration, given by

$$\frac{1}{\Delta} = \frac{1}{\omega_L - \omega} + \frac{1}{\omega_L + \omega}. \tag{3.3}$$

Here, ω_L is the angular frequency of the trapping light. The light for the dipole trap is generated by a solid state laser[1], which seeds a fiber amplifier[2]. The amplified output is split into two paths, each intensity-stabilized by an acousto-optical modulator (AOM)[3]. The AOMs shift the frequencies of the two beams by $+80\,\text{MHz}$ and $-80\,\text{MHz}$ respectively, preventing interference between them. Subseqently, the beams are fiber coupled[4] and delivered to the main experiment. Here, they are shaped to an aspect ratio $\approx 1:10$ using cylindrical lenses, and focused into the atomic plane. The resulting waists of the dipole trap beams on the atoms are $\approx 300\,\mu\text{m} \times 30\,\mu\text{m}$, which provides the strong vertical confinement necessary to create the quasi-2D systems studied in this thesis.

Near the end of the work presented in this thesis, the fiber amplifier had to be replaced[5], providing an opportunity to improve the stability of the optical setup in front of the fibers. We installed fast mechanical shutters[6], allowing the AOMs to be held at a constant RF power throughout most of the sequence, thereby reducing thermalization effects. The AOMs themselves were also replaced with a model exhibiting lower temperature-dependent pointing drifts[7]. To further enhance stability, all newly installed optical components are made of UV fused silica, which has a low coefficient of thermal expansion, reducing the effect of thermal lensing.

---

[1] Innolight Mephisto 2000 NE

[2] Nufern NuAmp 1064-PD-0050-C0

[3] G&H 3080-197

[4] NKT Photonics aeroGUIDE POWER

[5] now an ALS-IR-1064-50-A-CP-SF

[6] NM Laser Products LST400-12

[7] Pegasus Optik AA.MT80-A1,5-1064

3.2.2 Optical tweezer trap

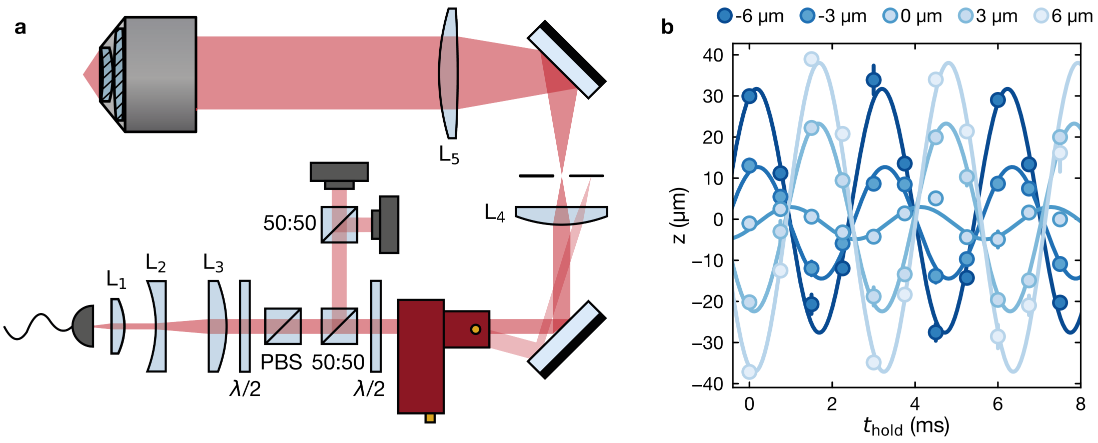

Figure 3.3 | **Setup used for generating the optical tweezer, focusing the objective using the tweezer.** **a** Schematic of the setup used for generating the tweezer beam: The fiber output at 1064 nm is collimated, and its size and polarization are adjusted to optimize the diffraction efficiency on a 2D AOD. The diffracted light is focused into an image plane, where undiffracted light and other diffraction orders are filtered out. Subsequently, this plane is imaged onto the atoms by a telescope, with our microscope objective being the final lens. Mirrors and dichroics are omitted where not necessary for the understanding of this setup. **b** Vertical oscillations in the dipole trap after releasing atoms from a tweezer at different vertical displacements. To increase the detectable signal, a time-of-flight measurement is performed after a hold time t_{hold} in the dipole trap. Each data point is the average over 3-4 measurements. Error bars give the standard deviation of the positions obtained for a given t_{hold}.

Investigating the edge dynamics of topological systems in ultracold quantum gas experiments requires precise control over the initial quantum state and its spatial extent, particularly the ability to populate small regions in the optical lattice. For this, we implemented an optical tweezer trap [142–146], which allows us to load ≈ 200 atoms and populate a few lattice sites in a controlled manner.

The experimental setup for the optical tweezer is illustrated in Fig. 3.3a: An optical fiber outputs light at 1064 nm[8], and is collimated by lens L_1, an asphere with a focal length of 18.4 mm. A Galilean telescope consisting of lenses L_2 and L_3 with focal lengths -50 mm and 75 mm respectively increases the beam diameter to improve the diffraction efficiency of the acousto-optical deflector (AOD) later on. A $\lambda/2$ plate together with a polarizing beam splitter are used to remove potential polarization fluctuations. We use a 50:50 beam splitter to split off half the beam power for intensity stabilization (with the power being distributed onto an in-loop and an out-of-loop photodiode by another 50:50 beamsplitter), and utilize a $\lambda/2$ waveplate to rotate the polarization by 90° to improve the diffration efficiency on the AOD[9]. The acousto-optical crystals in the AOD have been ground in such a way, that the first diffracted order exits the device parallel to the incoming beam. We

---

[8] derived from the Innolight Mephisto 2000 NE used for seeding the ALS amplifier

[9] AA Optoelectronics DTSXY-400-1064

optically Fourier transform the AOD plane with lens L_4 with focal length 150 mm, and filter out the undiffracted light as well as other diffraction orders here. This plane is then projected into the atomic plane by a telescope, formed by an achromat L_5[10] with focal length 400 mm, and our microscope objective with focal length 25 mm and NA $= 0.5$.

The resulting tweezer frequency is detuned from the seed laser by $f_{\mathrm{AOM}} + f_{\mathrm{AODx}} + f_{\mathrm{AODy}} \approx$ 230 MHz, providing sufficient detuning with respect to the optical dipole trap beams in the horizontal plane. Here f_{AODx} and f_{AODy} depend slightly on the precise tweezer position, while f_{AOM} is the frequency of the AOM used for intensity stabilization.

During the installation of the optical tweezer, we focused the objective onto the optical dipole trap by extracting the imaging response function from the density-density correlations of thermal atoms in the trap [147]. This allowed us to focus the optical tweezer into the same plane by trapping atoms in it and exciting oscillations along the optical axis. For this, we deliberately defocus the objective by a few µm, and release the atoms in the dipole trap from this position after a variable hold time t_{hold}. To increase the observable signal, we abruptly switch off all confining potentials after the hold time, and let the system expand for 7 ms. As we so far have not observed any focus shift between the tweezer focus and the focus of the imaging system, these measurements are now routinely used to focus the objective onto the dipole trap, with exemplary results shown in Fig. 3.3b.

While only a single tweezer trap was used for the measurements presented in this thesis, the AOD setup is capable of generating grids of multiple tweezers, with the DDS frequency source currently limiting us to two frequencies / two tweezers in each direction. This capability would however be interesting for studying the characteristics of topological systems by observing the interference and interactions of edge states on quantum point contacts [148, 149]. For such experiments, it is essential to populate the edge modes of the system at multiple locations with a constant phase relation.

To investigate our ability to do so, we performed measurements where two or four optical tweezers with a trap frequency $\omega_T/(2\pi) = 1.6(1)$ kHz were loaded from the same BEC of ^{39}K at $a_s = 6a_0$. The tweezers were kept at a constant position, while the remaining atoms in the dipole trap were expelled by briefly lowering the dipole trap, and increasing it back to its original value afterwards. Afterwards, we released the atoms from the tweezers simultaneously into the dipole trap, and let the system evolve for 2 ms. An exemplary absorption picture obtained this way is shown in Fig. 3.4a, with a measurement for two tweezers shown on the top, and a result for four tweezers on the bottom. However, upon repeating this measurement, the phase of the interferenca pattern fluctuates, which is indicative of the atoms acquiring varying phases in the tweezers. The resulting interference pattern washes out, as shown in the averaged absorption images in Fig. 3.4b. This demonstrates that the phase relation between the tweezers fluctuates significantly, preventing the deterministic preparation of phase relations. To confirm that the coherence of the individual tweezers is preserved, one can evaluate the average of the squared absolute value of the

---

[10] Thorlabs AC508-400-B

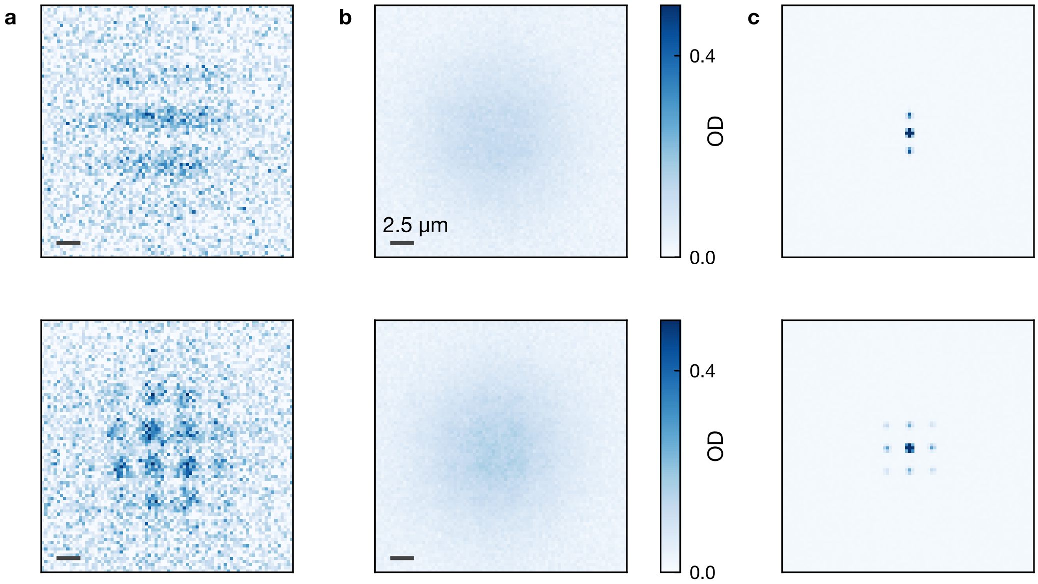

Figure 3.4 | Interference of multiple tweezer traps in the dipole trap. a In situ absorption pictures obtained 2 ms after releasing the atoms into the crossed optical dipole trap from two (top) and four (bottom) tweezer traps, each with a trap frequency of 1.6(1) kHz. **b** Average over 118 absorption pictures obtained for the same settings as in **a**, with two tweezers shown on the top, and four tweezers on the bottom. **c** The individual absorption pictures used in **b** are Fourier transformed, and then the average over their squared absolute value is determined.

Fourier transform $\overline{|\mathcal{F}(\mathrm{OD}_i)|^2}$, shown in Fig. 3.4c, with OD_i being the optical density of an individual absorption picture. Here, strong peaks are visible at the spatial frequency of the interference patterns, with no other prominent features present apart from the central peak from the envelope at zero frequency, confirming the coherence of the individual wavepackets.

To improve the phase stability of the tweezers, one of the first modifications to do on the setup would be to perform intensity stabilization of the tweezers (the setup being illustrated in Fig. 3.3a) on the diffracted beam after the AOD, instead of stabilizing the ingoing beam. As the tweezers generated by the AOD will have slightly varying trap frequencies depending on their precise location, global intensity fluctuations of all tweezers lead to a varying potential energy difference between the atoms trapped in different tweezers, causing the atoms to acquire differential phases. Therefore, it is essential for the global intensity of the tweezers to be stabilized well. A straightforward approach to target this is to replace the mirror after the AOD with a plate beam splitter, allowing one to directly measure the intensity of all diffracted tweezers.

Furthermore, additional improvements could be made to the signal generation for the AOD input. The radio frequency signal used here is currently generated by the four output channels of a direct digital synthesis (DDS) IC[11], two channels each being combined using

---

[11] Analog Devices AD 9959

a splitter[12], with the resulting channels being amplified by a 5 W amplifier[13]. Currently, the phase of the four channels is not fixed with respect to the start of the tweezer intensity ramp, which means that intermodulation effects from nonlinearities in the signal path could also lead to varying acquired phases of the trapped atoms. While nonlinearities, and thus intermodulation effects, can never be fully eliminated from an experiment, their effect onto the atoms could be reduced by driving the AOD with phase relations fixed at the start of the tweezer loading.

3.2.3 Programmable repulsive potentials using a DMD

A digital micromirror device (DMD) consists of a programmable arrays of indiviually adressable microscopic mirrors. By tilting each mirror into an "on" or "off" state, a DMD can function as an arbitrary binary mask. In experiments on ultracold quantum gases, DMDs are routinely used for tasks such as shaping bulk systems [52, 70, 150], or for locally controlling the Hamiltonian in optical lattice systems [151–153].

The preparation and observation of topological edge states requires a well-defined boundary, separating regions with distinct topological invariants. Although the harmonic confinement naturally present in cold atom experiments in principle provides such a boundary, the non-infinite sharpness of the boundary leads to the dispersion of the edge mode hybridizing with the bulk modes, broadening the edge states and reducing their velocity, thereby making them hard to detect [154–156]. This underlines the necessity of a DMD used for projecting a topological interface to have a high resolution in the atomic plane, such that narrow boundaries can be realized, simplifying the detection.

To prevent optical speckle and ripples, which could inhibit the transport properties of the system, we illuminate the DMD spatially and temporally incoherent [157, 158]. The light source is created by overlaying four multi-mode laserdiodes[14] using a knife edging module[15]. An AOM[16] controls the intensity of the combined beam, and the light is subsequently coupled into a square-core fiber[17]. The square core fiber not only has the benefit of generating a square top-hat output mode, but also introduces spatial mode mixing, further reducing interference effects. To further minimize residual speckle, we rapidly average over different mode outputs by modulating the AOM drive frequency with a modulation frequency of 1 MHz. This technique yields a flat illumination profile with a residual speckle contrast of $\sim 3\%$, ensuring that potential corrugations at the projected topological interface are negligible.

---

[12] Mini Circuits ZFSC-2-4-S+

[13] Mini Circuits ZHL-5W-1

[14] USHIO HL63623HD

[15] Lasertack Beam Combiner Module for 9 mm laser diodes, with a fixed distance mirror, including 4 mm focal length collimation lenses

[16] G&H AOMO 3200-125

[17] Thorlabs FP150QMT

An added benefit of using this incoherent illumination scheme, compared to directly imaging a coherently illuminated DMD, is an improvement in optical resolution: As the square core fiber emits light approximately isotropically within the imaging system's numerical aperture, the minimal distance d between two points which can be distinguished is

$$d = 0.61\frac{\lambda}{\mathrm{NA}}, \tag{3.4}$$

where λ is the wavelength of the light illuminating the DMD, and NA the numerical aperture of the (circular aperture) objective [159]. In contrast, for coherent illumination, where different points in the image plane share the same phase, the minimal distinguishable distance is $d = 1.22\frac{\lambda}{\mathrm{NA}}$.

To design the optical system such, that the full numerical aperture of the imaging system is illuminated, while avoiding losing light due to clipping at the aperture, it makes sense to think about the design in terms of the conservation of étendue [160, 161]: The étendue G of a beam of light is defined as

$$G = n^2 \int_A \int_\Omega \cos(\theta)\, dA d\Omega, \tag{3.5}$$

where n is the refractive index of the medium the light is propagating in, A is the surface on which this light is emitted, Ω is the solid angle of emission, and θ the angle between a given ray with respect to the surface normal of area A.

For paraxial beams and for emission that is homogeneous and isotropic over area A and within solid angle Ω, this simplifies to

$$G = n^2 A\Omega. \tag{3.6}$$

The conservation of etendue states that in any passive, lossless optical system, the etendue can not decrease: $G_{\text{in}} \leq G_{\text{out}}$ [160, 161].

By calculating the etendue of the square core fiber output and applying this principle, we determine the smallest area on the atoms one can illuminate using the full objective NA while not losing light to be $\sim 120\,\mu\text{m} \times 120\,\mu\text{m}$. This, in turn, dictates that the illuminated area on the DMD should be $\sim 5\,\text{mm} \times 5\,\text{mm}$.

The optical setup we use for projecting the mask displayed on the DMD into the atomic plane is illustrated in Fig. 3.5a: The output of a square-core fiber is imaged onto the DMD using an aspheric condenser lens L_1 with focal length 12 mm. This gives us a region of $\sim$ 5mm × 5mm on the DMD[18], which is illuminated with a relatively flat intensity profile, as illustrated in Fig. 3.5b and c. In the following, we project the DMD into the atomic plane with a demagnification ~ 45. For this, we use two telescopes, the first consisting of lenses L_2 and L_3 (focal lengths 150 mm and 100 mm, respectively), and the second of L_4[19] having a focal length of 750 mm, and our microscope objective with a focal length of

---

[18] Vialux V-7000

[19] Thorlabs AC508-750-A

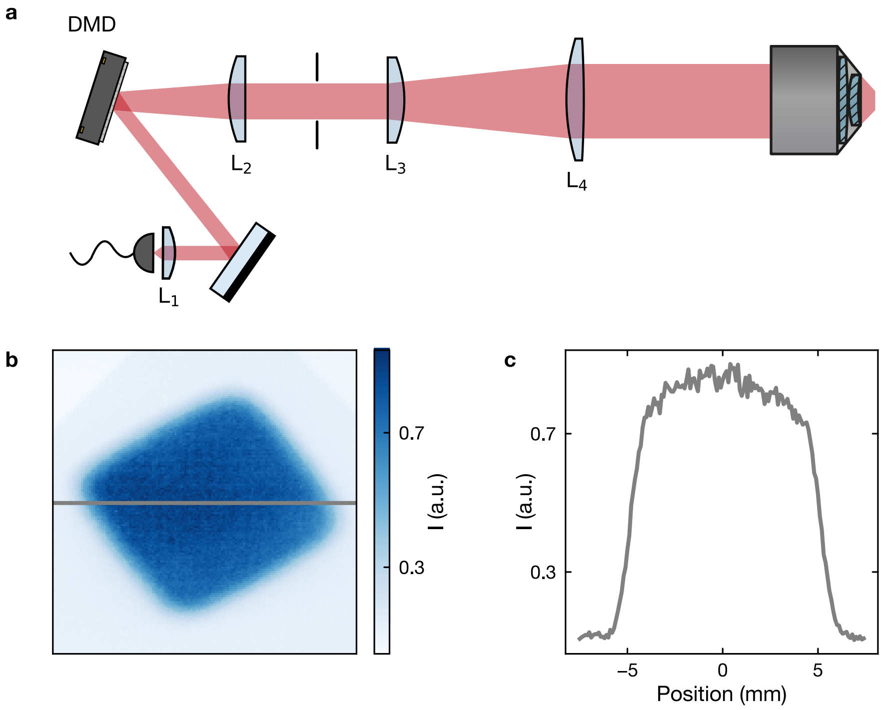

Figure 3.5 | Optical setup for projecting arbitrary repulsive potentials. a Schematic sketch of the DMD setup. Mirrors and dichroics are omitted where not necessary. The section stabilizing the intensity of the fiber output is not shown. **b** Output of the square-core fiber reflected off the DMD in an all-on state. The tip of the fiber is imaged onto the DMD, yielding an almost flat-top illumination within a rectangular region. **c** Cut through the intensity profile on the DMD. The grey line in **b** marks the location at which this cut is performed.

25 mm. An automated iris was placed in the Fourier plane between L_2 and L_3, allowing us to reduce the resolution with which the DMD is projected into the atomic plane for our measurements in Sec. 4.4.3. However, at this location, the speckle beam has already been overlaid with the DMD path via a dichroic, so that this iris has been impractical for our measurements in Chapter 5, and has been removed.

It is also important to note, that a simpler configuration was used for most measurements in Chapter 4: Here, instead of two telescopes, only one telescope (consisting of an achromat[20] with focal length 1000 mm and the microscope objective) was used to project the DMD into the atomic plane with a demagnification of ~ 40, such that a slightly larger region in the atomic plane was illuminated. The only exceptions for this are the results presented in Fig. 4.3b and in Fig. 4.11. The remainder of the optical setup, in particular the asphere imaging the fiber tip onto the DMD, remained unchanged.

---

[20] Thorlabs ACT508-1000-A

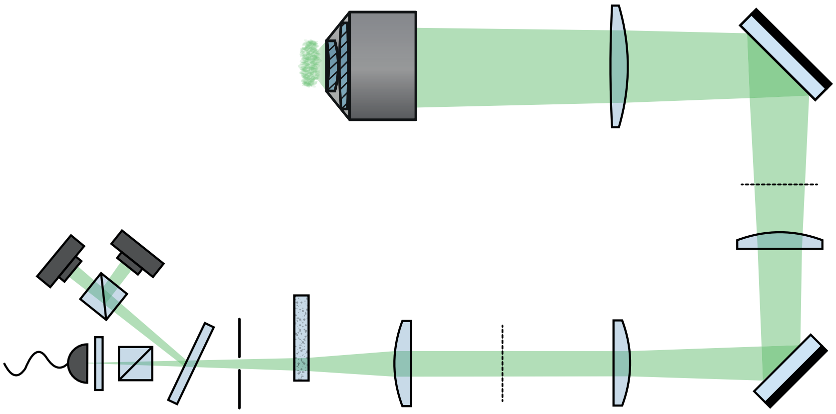

Figure 3.6 | Optical setup used for projecting disorder potentials. A diffuser is illuminated with an uncollimated laser beam. It is subsequently optically Fourier transformed, and imaged into the atomic plane. The dashed lines mark planes conjugate to the atomic plane. Mirrors and dichroics are omitted where not necessary for understanding the setup.

3.2.4 Controlled disorder potentials using optical speckle

Experiments on ultracold quantum gases, unlike condensed matter systems, where disorder is typically fixed and difficult to characterize, are relatively clean and free of defects. This makes it interesting to re-introduce disorder in a controlled manner, investigating the dependence of a system's properties on the characteristics and the amount of disorder. For this, several different methods have been developed: Multiple incommensurate optical lattices can be utilized, generating a quasi-random system [103, 162–164]. Alternatively, a DMD can be projected into the atomic plane using a high-NA objective [165, 166]. Lastly, optical speckle potentials can be used to generate disorder [167, 168], as is often done in studies of Anderson localization [104, 106, 107, 169].

In topological systems, disorder can introduce phase transitions into different regimes, as has been studied in the context of a 1D Thouless pump [75], or a 1D momentum-space lattice [74] using ultracold atoms. To study the influence disorder has on our Floquet systems, we have installed an optical speckle setup, which allows us to project disorder with a short correlation length into the atomic plane.

The optical setup employed here is illustrated in Fig. 3.6a: A solid-state laser[21] generates light at 532 nm. A PBS is used to remove any polarization noise, and the light is sent through an AOM with low thermal drifts[22] to stabilize the power and regulate the intensity. After the AOM, a shutter[23] enables us to keep the AOM at power when the potential is off, further reducing thermal drifts. The light is then fiber coupled into a photonic crystal fiber[24] with a mode field diameter of 12.5(15) µm and a divergence half angle of

---

[21] Lighthouse Photonics Sprout G-15W

[22] IntraAction ASD-1002B47

[23] NM Laser Products LST400-12

[24] NKT Photonis aeroGUIDE POWER

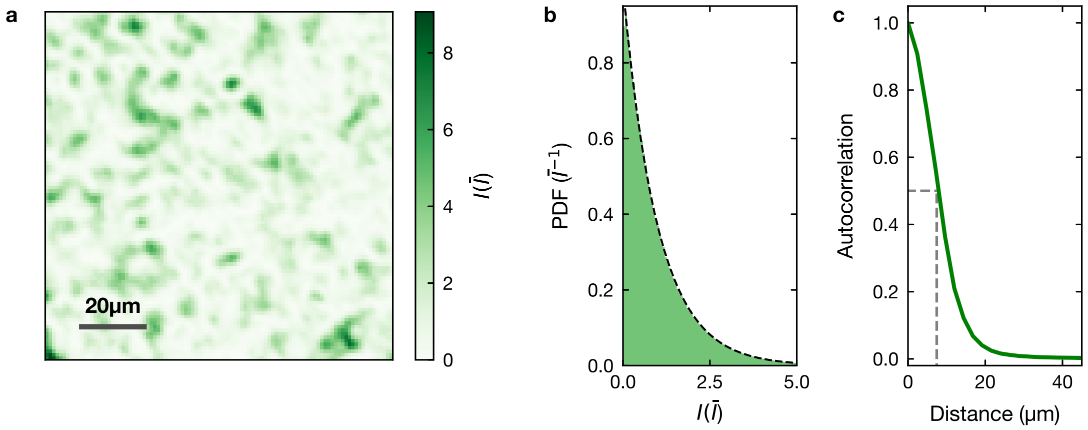

Figure 3.7 | Characteristics of the speckle potential. a Exemplary speckle image taken in the intermediary imaging plane between L_3 and L_4. The scale bar has a length of 20 µm. **b** Theoretically expected probability density function for an idealized speckle pattern (dashed line), together with a histogram of the intensity distribution in speckle patterns recorded in the intermediary image plane (in green). **c** Averaged radial autocorrelation of the speckle patterns recorded in the intermediary image plane. The dashed lines mark the half width half max width of 7.9 µm of the autocorrelation. Both **b** and **c** use the same dataset of 118 images recorded in the intermediary image plane.

$\theta_D = 1.6(2)°$. The fiber output is not collimated, but instead left to diverge, with the fiber tip being protected by a glass plate[25]. A PBS ensures a well-defined polarization, and a beam sampler is used to pick off a part of the beam as a signal for intensity stabilization. An electronically adjustable iris[26] allows to crop the beam size for adjusting the correlation length during measurements, but was not used for any of the results in this thesis. Finally, the beam illuminates a holographic diffuser[27], randomizing the phase profile of the beam. This diffuser is mounted in a rotation mount[28], which allows us to rotate the diffuser around an axis, which is different from the beam path. This way, the illuminated patch on the diffuser changes when it is rotated, allowing us to realize different speckle patterns. By optically Fourier transforming the plane of the diffuser using a lens with focal length $f_1 = 100\,\mathrm{mm}$, one now obtains a speckle pattern.

This pattern is subsequently demagnified by two telescopes. The first is formed by lenses L_2 and L_3 ($f_2 = 150\,\mathrm{mm}$, $f_3 = 100\,\mathrm{mm}$), and the second by L_4 and our microscope objective ($f_4 = 750\,\mathrm{mm}$, $f_{\mathrm{obj}} = 25\,\mathrm{mm}$), yielding a combined demagnification of 45. An exemplary speckle pattern, taken in the intermediary image plane between L_3 and L_4, is shown in Fig. 3.7a.

---

[25] Thorlabs WG41050-A

[26] Thorlabs Elliptec ELL15K

[27] Edmund Optics #35-693

[28] Thorlabs ELL14K

When, like in a speckle pattern generated by a diffuser, many electric field components with random phases are added together, the resulting distribution of the amplitude A of the electric field is known to follow a Rayleigh distribution

$$p(A) = \frac{A}{\sigma^2} e^{-A^2/(2\sigma^2)}, \tag{3.7}$$

where σ characterizes the width of the distribution. To determine the resulting probability density function of the intensity, one has consider the conservation of probability, ensuring that the probability for the amplitude to fall in range dA is equal to the probability for the intensity to fall in range dI,

$$\begin{aligned} p(A) \cdot dA &= p(I) \cdot dI. \\ \Rightarrow p(I) = p(A) \cdot \left| \frac{dA}{dI} \right| &= p(A) \frac{1}{2\sqrt{I}}, \end{aligned} \tag{3.8}$$

using that $A \geq 0$ and $A = \sqrt{I}$. Substituting this into Eq. 3.7 yields

$$p(I) = \frac{1}{2\sigma^2} e^{-I/(2\sigma^2)}. \tag{3.9}$$

By making use of the expectation value of the Rayleigh distribution $\langle I \rangle = \langle A^2 \rangle = 2\sigma^2$, we can express this as

$$p_{\bar{I}}(I) = \bar{I}^{-1} \exp\left(\frac{-I}{\bar{I}}\right), \tag{3.10}$$

with $\bar{I}$ being the average intensity of the speckle pattern [158].

To characterize the quality of our experimentally realized speckle pattern, we evaluate the probability density function (PDF), as shown in Fig. 3.7b: The measured intensity distribution (green histogram), evaluated on the central 720 µm × 720 µm region of images taken in the intermediary plane between L_3 and L_4, closely matches the expected distribution (dashed line). This verifies, that we are in the fully developed speckle regime, meaning that a large number of scatterers with sufficiently random phases contribute to the pattern formation [158].

Another important characteristic of the speckle pattern is the correlation length. We determine the correlation length in the intermediary image plane by evaluating the autocorrelation

$$\rho(i,j) = \frac{\sum_k \sum_l I(k,l) \cdot I(k+i, l+j)}{\sum_k \sum_l I(k,l)^2}, \tag{3.11}$$

where i and k as well as j and l are pixel indices in horizontal and vertical direction, respectively. We evaluate the autocorrelation on the same region of the images taken in the intermediary image plane as used in the PDF evaluation, and perform a radial average.

The result is shown in Fig. 3.7c: We find a radial correlation length, defined as the half width half max width of the autocorrelation, of 7.9 µm.

However, this value is insufficient to determine the correlation length in the atomic plane, as calculating the propagation through the optical system requires knowledge of the electric field, and not just the intensity. Instead, we determine the width of the Gaussian envelope in the back focal plane of the objective, and find a $1/e^2$ diameter of 33.3(2) mm. We then numerically propagate a speckle beam with identical parameters as in our experimental realization through an ideal objective with NA $= 0.5$, and find a correlation length of 296^{+11}_{-7} nm this way.

To estimate the axial correlation length, we determine an effective numerical aperture $\mathrm{NA}_{\mathrm{eff}}$, which yields the same correlation length $\sigma_r = 296\,\mathrm{nm}$ using the standard relation [158]

$$\sigma_r = \frac{\lambda}{4 \cdot \mathrm{NA}_{\mathrm{eff}}}. \tag{3.12}$$

The axial correlation length can now be related to the radial one through this effective numerical aperture [158]

$$\sigma_z \approx 0.89 \frac{\lambda}{\mathrm{NA}_{\mathrm{eff}}{}^2}, \tag{3.13}$$

obtaining $\sigma_z = 2.4\,\mu\mathrm{m}$. This correlation length is significantly larger than the harmonic oscillator length of the ground state in our crossed optical dipole trap in z-direction $\ell_z = 0.9\,\mu\mathrm{m}$.

Eq. 3.10 shows, that the intensity distribution of a fully developed speckle pattern is completely characterized by its mean potential strength $\overline{V}_D$. The precise calibration of this disorder strength however is a challenging task. Extracting the width of a speckle beam can be achieved by measuring the deflection [167] or the heating [170] due to the beam while translating it in space. To determine the strength of the potential, experiments so far have relied on extracting the mean potential strength by beam power measurements [104, 171–173]. In the case of the speckle beam being formed by close-detuned dipole potentials, spectroscopic measurements allow for an in-situ calibration of the potential strength [174]. As a result of the small detuning however, scattering rates are high, so that this approach is limited to low disorder strengths.

We have developed a method employing the diffraction of a noninteracting BEC on a speckle pattern to calibrate the potential strength $\overline{V}_D$ directly in situ. For this, we start with a BEC of ^{39}K at a scattering length of $6a_0$ in our crossed optical dipole trap. We then, analogously to Kapitza-Dirac diffraction of a BEC on a pulsed optical lattice [175, 176], apply a short pulse of the speckle beam with a duration on the order of 10 µs to 270 µs onto the atoms. Afterwards, we let the system expand in the dipole trap for 8 ms, with this evolution time being limited by the dipole trap frequency ∼ 40 Hz. Exemplary averaged images of the atomic cloud after this evolution are shown in Fig. 3.8a for a potential strength $\overline{V}_D/h = 2.8\,\mathrm{kHz}$. Here, one can see the separation into a bimodal system: The scattered atoms form a broad distribution, while in the center a fraction of unscattered atoms remains.

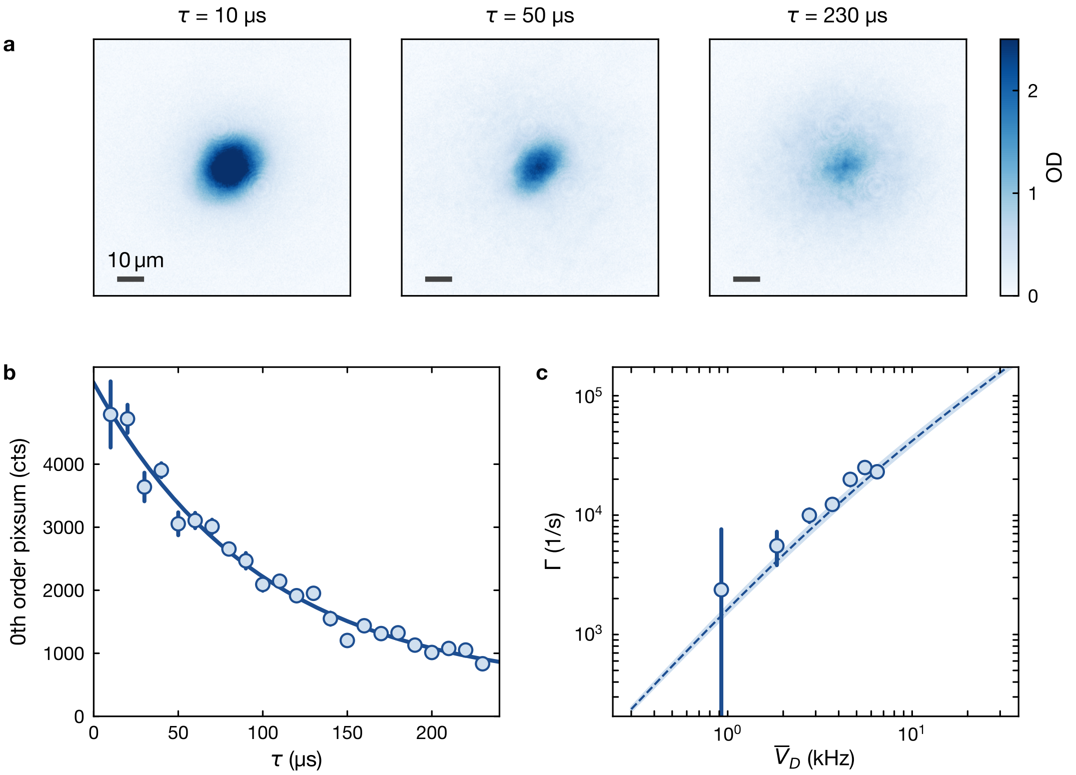

Figure 3.8 | Calibration of the speckle potential strength. a Averaged experimental shots of a BEC after pulsing on a speckle potential with $\overline{V}_D/h = 2.8$ kHz for different pulse durations τ. After the pulse, the atoms are left in the dipole trap to expand for 8 ms, before absorption imaging is performed. The scale bar in the bottom left corner indicates 10 µm. **b** The integrated signal in the undiffracted fraction of the atoms is plotted as a function of the pulse duration τ for $\overline{V}_D/h = 2.8$ kHz. The solid line is an exponential fit with an offset. Each data point is the average of 21-22 measurements, taken with a different speckle realization. The error bars have been extracted via bootstrapping. **c** The decay rates Γ together with the control voltage on the in-loop photodiode are fitted to the numerical simulation (dashed line) by fitting a proportionality factor between photodiode voltage and potential strength $\overline{V}_D$. The shaded area around the dashed line is the systematic uncertainty of the numerical simulation due to the choice of window length.

We extract this unscattered atom fraction using a two-component fit, combining a broad Gaussian (fitting the scattered atoms) with a narrow Thomas-Fermi distribution (for the unscattered fraction). A decay with a time constant increasing with beam power can be observed in the unscattered fraction, with an exemplary measurement for $\overline{V}_D/h = 2.8\,\mathrm{kHz}$ being shown in Fig. 3.8b. We perform a fit of form

$$N_{\mathrm{at}}\left(t\right) = a \cdot \exp\left(-\Gamma \cdot \tau\right) + b \tag{3.14}$$

with free parameters a, b and Γ, to extract the decay rate τ at each power setting. In this fit, we weigh each data point using an uncertainty in atom number, which we extracted via bootstrapping: From a set of N images taken with the same parameters, we randomly draw N images, where repetitions are possible. We then fit the unscattered atom fraction on the averaged image. We repeat this procedure 100 times, and take the inverse of the standard deviation of these atom numbers as a weight in the exponential fit for this data point.

To relate decay rate measured to the potential strength, we numerically simulate a BEC's response when exposed to a speckle pattern for varying pulse duration and potential strength. We determine the decay rates in the unscattered atom fraction analogously to the experimental data, and perform a fit of form

$$\Gamma\left(\overline{V}_D\right) = \overline{V}_D^{a+1} \cdot \left(b \cdot \overline{V}_D^{a} + c\right)^{-1} \tag{3.15}$$

to the numerically simulated decay rates Γ for disorder strength $\overline{V}_D$, with a, b and c being free parameters. We fit a proportionality constant α between the in-loop photodiode voltage and the potential strength, such that the experimental data collapses onto the numerical function. For our specific case, we obtain $\alpha = 9.24\,\mathrm{kHz/V}$.

Several factors contribute to the systematic and statistical uncertainties of this calibration: The fitted decay constant depends slightly on the choice of window length over which the decay of the unscattered fraction is observed. To account for this, we vary the length of this window on the numerical simulation, starting with a window length which allows us to capture the fast initial decay ($\tau\overline{V}_D \in [0.2, 0.6]$, depending on the disorder strength), and increasing the window length until the full decay is captured. We then perform a fit of Eq. 3.15 onto the largest and the smallest decay constants obtained at each potential strength, and fit these curves to the experimental data. This way, we obtain a systematic uncertainty of $\Delta_{\mathrm{decay}} = \left({}^{+0.64}_{-0.51}\right)\,\mathrm{kHz\,V^{-1}}$.

Another systematic contribution arises from the uncertainty in the speckle correlation length $\sigma_r = 296^{+11}_{-7}\,\mathrm{nm}$. We repeat the numerical simulations of the system for the upper and the lower estimate of the correlation length, and by fitting our experimental data to the calibration curves obtained this way, determine the systematic error due to this effect to be $\Delta_{\mathrm{corr}} = \left({}^{+0.24}_{-0.05}\right)\,\mathrm{kHz\,V^{-1}}$. Similarly, we repeat the numerical simulations while varying the size of the BEC by $\pm 2\,\mu\mathrm{m}$, yielding $\Delta_{\mathrm{BEC}} = \pm 0.05\,\mathrm{kHz\,V^{-1}}$.

Regarding statistical uncertainties, we first consider the fit error of the experimental data onto the calibration curve, Δ_{fit}. This error originates from the uncertainty in estimating the unscattered atom fraction, and is subsequently propagated as a fit uncertainty. Here, we obtain $\Delta_{\mathrm{fit}} = 0.22\,\mathrm{kHz\,V^{-1}}$. Additionally, the Gaussian envelope of the speckle beam leads to a spatially varying disorder strength across the system. We estimate this error based on the expected waist of the Gaussian envelope and the typical system sizes, obtaining $\Delta_{\mathrm{envelope}} = \pm 0.11\mathrm{kHz\,V^{-1}}$.

Combining these contributions, we obtain the final calibration constant

$$\alpha = \left(9.24 \pm (0.25)_{\mathrm{stat}} \left({}^{+0.93}_{-0.61}\right)_{\mathrm{sys}}\right)\,\mathrm{kHz\,V^{-1}}.$$

Here, Δ_{decay}, Δ_{corr} and Δ_{BEC} contribute as systematic errors to the measurement, such that $\Delta_{\text{sys}} = \Delta_{\text{decay}} + \Delta_{\text{corr}} + \Delta_{\text{BEC}}$, and Δ_{envelope} together with the fit error Δ_{fit} onto the calibration curve contribute as statistic errors via $\Delta_{\text{stat}} = \sqrt{\Delta_{\text{fit}}^2 + \Delta_{\text{envelope}}^2}$.

As these errors on the calibration constant are proportional to the error in any potential strength $\overline{V}_D$, so that the calculation is straightforward, they will in the following not be referenced in the text to ensure readability. However, when data is plotted, the error will be displayed as an error bar on the disorder strength.

3.3 Optical lattice

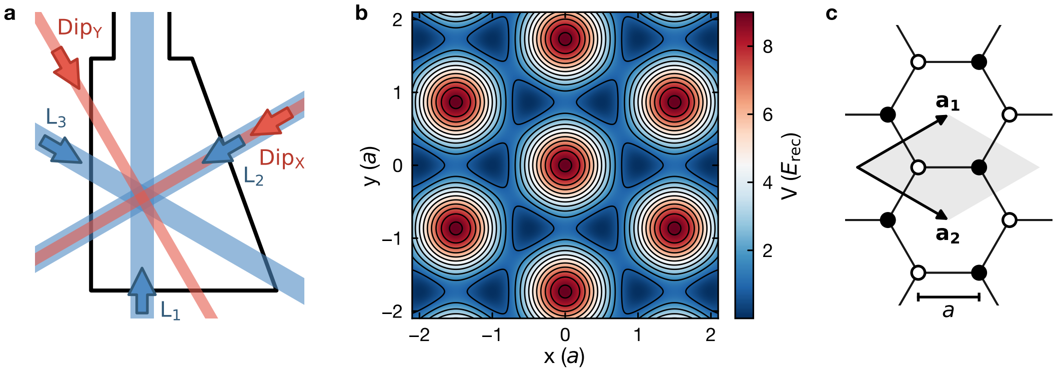

Figure 3.9 | Optical hexagonal lattice. a Top view of the glass cell used as a science chamber. The two red beams Dip$_X$ and Dip$_Y$ represent the dipole trap beams. The three blue beams L$_1$, L$_2$ and L$_3$ make up the optical lattice. The right side of the glass cell is angled to prevent back reflections from hitting the atoms. **b** Real-space potential formed by the three lattice beams for an exemplary lattice depth of $1E_{\text{rec}}$. Since the potential is repulsive, the atoms are trapped in the dark blue regions. **c** The unit cell of the hexagonal lattice (grey shaded area) together with the lattice vectors $\mathbf{a_1}$ and $\mathbf{a_2}$. It contains two lattice sites (one A- and one B-site), with a spacing of $a = 287$ nm between them.

In our experiment, we employ a titanium-sapphire laser[29] at 745 nm to generate the light for our optical hexagonal lattice. This wavelength is blue detuned both for the D_1 and the D_2 lines of ^{39}K at 770 nm and 767 nm, respectively, so that the resulting potential is repulsive.

The lattice consists of three free-running laser beams, intersecting under an angle of 120°, propagating along the directions

$$\mathbf{k_1} = k_L \begin{pmatrix} 0 \\ 1 \end{pmatrix}, \qquad \mathbf{k_2} = \frac{k_L}{2} \begin{pmatrix} -\sqrt{3} \\ -1 \end{pmatrix}, \qquad \mathbf{k_3} = \frac{k_L}{2} \begin{pmatrix} \sqrt{3} \\ -1 \end{pmatrix}, \qquad k_L = \frac{2\pi}{\lambda_L}. \tag{3.16}$$

Since the size of the beams at the location of the atoms is significantly larger than the system sizes we study (the waist of the beams is $w_{\text{hor}} \approx 400\,\mu\text{m}$ along the horizontal

---

[29] Sirah Matisse CS

direction, and $w_{vert} \approx 100\,\mu\text{m}$ along the vertical direction), we treat each laser beam as a plane wave with identical angular frequency ω_L:

$$E_j\left(\mathbf{r},t\right) = \sqrt{\frac{2I_j}{c\epsilon_0}} \cdot e^{i\left(\mathbf{k_j}\cdot\mathbf{r}-\omega_L t\right)} \left(\cos\left(\theta_j\right)\mathbf{e_z} + \sin\left(\theta_j\right) e^{i\alpha_j}\left(\mathbf{e_z}\times\mathbf{k_j}\right)\frac{1}{k_L}\right) \tag{3.17}$$

Here, the angle θ_j describes the polarization of the electric field, and α_j accounts for phase shifts between s- and p-polarization to describe elliptical polarizations. The resulting interference pattern can be decomposed into a s- and a p-polarized component:

$$I\left(\mathbf{r}\right) = I_s\left(\mathbf{r}\right) + I_p\left(\mathbf{r}\right) \tag{3.18}$$

$$I_s\left(\mathbf{r}\right) = \frac{c\epsilon_0}{2}\left|\sum_{j=1}^{3} E_{j,s}\left(\mathbf{r},t\right)\right|^2 = \frac{c\epsilon_0}{2}\sum_{j,l=1}^{3}\sqrt{I_j I_l}\cos\left(\theta_j\right)\cos\left(\theta_l\right)e^{-i\left(\mathbf{k_j}-\mathbf{k_l}\right)\mathbf{r}} \tag{3.19}$$

$$I_p\left(\mathbf{r}\right) = \frac{c\epsilon_0}{2}\left|\sum_{j=1}^{3} E_{j,p}\left(\mathbf{r},t\right)\right|^2 = \frac{c\epsilon_0}{2}\sum_{j,l=1}^{3}\sqrt{I_j I_l}\cos\left(\theta_j\right)\cos\left(\theta_l\right)\cos\left(\eta_j-\eta_l\right)e^{-i\left(\mathbf{k_j}-\mathbf{k_l}\right)\mathbf{r}}e^{i\left(a_j-a_l\right)}, \tag{3.20}$$

where $\eta = (0, 2\pi/3, 4\pi/3)$. Assuming the three beams are s-polarized and possess identical intensity I_0, the intensity distribution simplifies to

$$I\left(\mathbf{r}\right) = I_0\left(3 + 4\cos\left(\frac{\sqrt{3}}{2}k_L x\right)\cos\left(\frac{3}{2}k_L y\right) + 2\cos\left(\sqrt{3}k_L x\right)\right). \tag{3.21}$$

This intensity distribution is shown in Fig. 3.9b, and represents the distribution ideally obtained in our unmodulated lattice. It is directly proportional to the trapping potential (cf. Eq. 3.2). This lattice has a spacing of

$$a = \frac{4\pi}{3\sqrt{3}k_L} = 287\,\text{nm} \tag{3.22}$$

between the A- and B-sites of the lattice. A natural energy scale in optical lattices is given by the recoil energy [177, 178]

$$E_{\text{rec}} = \frac{\hbar^2 k_l^2}{2m}, \tag{3.23}$$

with m being the mass of a ^{39}K atom, $m_{\text{K}} = 6.47 \times 10^{-26}\,\text{kg}$, leading to a recoil energy of $E_{\text{rec}} = h \cdot 9.23\,\text{kHz}$.

3.3.1 Aligning the lattice and balancing the potential

We found the dynamics in the optical lattice potential to be quite sensitive on the precise alignment and the power balancing between the three beams. Because of this, we regularly

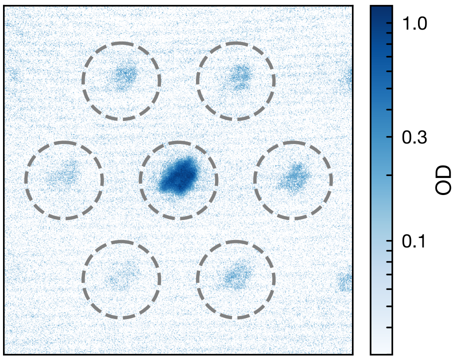

Figure 3.10 | Balancing of the optical lattice potential. Absorption picture of ^{39}K at $6a_0$ obtained after 3.5 ms time of flight following an abrupt switch-off of the lattice potential with a depth of $5.9\,E_R$. The dashed circles mark the initial position of the BEC as well as the positions of the diffracted peaks around it.

realign the beams before taking data, and optimize the power balancing by performing diffraction measurements.

For the alignment of the individual lattice beams, in-situ absorption pictures of the potassium BEC are taken along the optical axes of the lattice beams. Subsequently, the lattice beams are imaged and aligned to vertically overlap with the BEC on the camera. For this, electronically adjustable mirror mounts[30] are employed.

To align the beams horizontally, we take in-situ pictures of the BEC along the z-direction. Here, by turning a single beam on, one can observe a deflection due to its repulsive dipole potential. By aligning the beams, using the electronically adjustable mirror mounts, one can minimize this deflection when the center of the beam overlaps with the BEC.

To correct for intensity imbalances among the lattice beams, we employ Kapitza-Dirac diffraction [179]: The atoms are first loaded into the optical lattice at a depth close to the target value (typically $5.9E_R$), where we hold them for 10 ms. Subsequently, all confining potentials are abruptly switched off. After 3.5 ms time of flight, a characteristic diffraction pattern emerges (as shown in Fig. 3.10), which contains information about the coherence of the system and the momentum distribution in the optical lattice [180–182]. Each diffraction peak originates from the interference of a pair of lattice beams, and by adjusting the relative beam intensities, the peaks can be balanced such that they exhibit equal strength, determined from the integrated signal around each peak. Since fluctuations in the initial BEC position as well as mechanical vibrations introduce shot-to-shot variations, the measured signal is averaged over multiple realizations of the experiment.

---

[30] Newport New Focus 8807

3.3.2 Lattice depth calibration

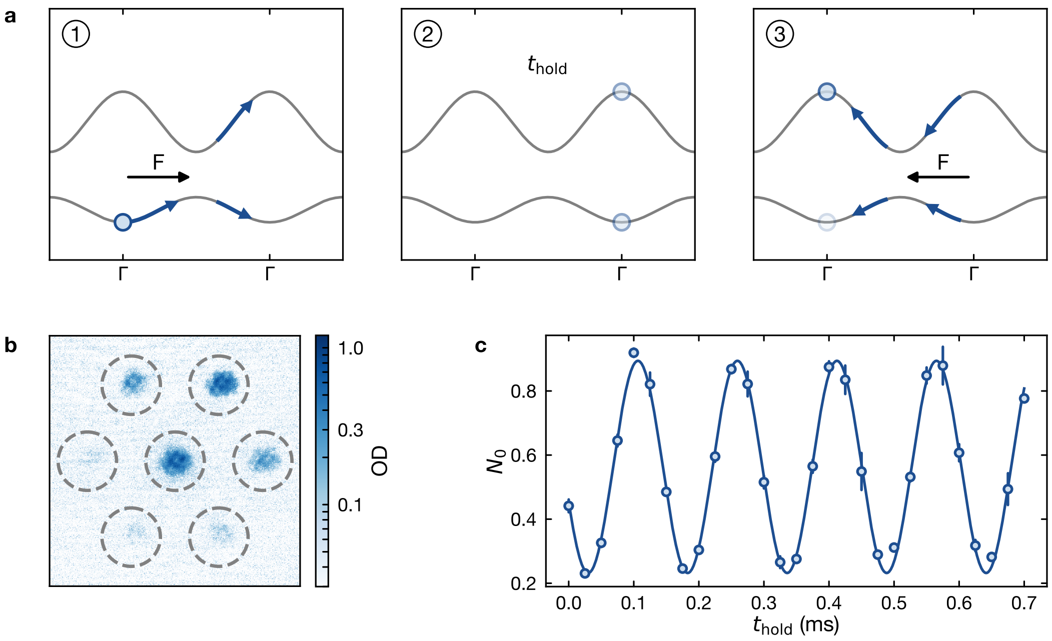

Figure 3.11 | Calibration of the lattice potential strength. a Illustration of the experimental sequence for performing Stückelberg interferometry to probe the energy gaps of our system. **b** Absorption picture of ^{39}K at $6a_0$ obtained after 3.5 ms time of flight in the calibration sequence for a lattice depth of 6.08 E_R. The central dashed circle marks the position of the atoms in the lowest band. The outer circles mark the location of atoms in the first excited band of the optical lattice. **c** Fraction of atoms remaining in the lowest band of the system as a function of hold time at $\mathbf{k} = \Gamma'$ for a 6.08 E_{rec} deep lattice.

To measure the depth of our opitical lattice, we employ Stückelberg interferometry [183–185]. For this, our optical lattice can be accelerated in arbitrary directions by detuning the frequency of one or two lattice beams via AOMs. In a reference frame co-moving with the lattice, this procedure is equivalent to accelerating the atomic cloud itself [69, 186]. For a constant acceleration of the lattice, the acceleration can be expressed as

$$\mathbf{a} = \frac{2}{3}\lambda_L \frac{\Delta f}{\Delta t}, \tag{3.24}$$

with $\Delta f/\Delta t$ being the rate at which the lattice beam detuning is changing. The force due to lattice acceleration can be written as

$$\mathbf{F} = \hbar\frac{\Delta \mathbf{k}}{\Delta t}. \tag{3.25}$$

By comparing Eq. 3.24 and Eq. 3.25, and making use of Newton's second law $\mathbf{F} = m \cdot \mathbf{a}$, one obtains

$$\Delta \mathbf{k} = \frac{2m\lambda_L \Delta f}{3\hbar}. \tag{3.26}$$

The experimental sequence to perform Stückelberg interferometry is schematically illustrated in Fig. 3.11a: We begin with a weakly interacting ($a_s = 6a_0$) BEC of ^{39}K prepared in the center of the lowest band at $\mathbf{k} = \Gamma$, in a state denoted $|\psi^1_\Gamma\rangle$. Subsequently, we accelerate the atoms nonadiabatically to $\mathbf{k} = \Gamma'$, the center of the neighboring Brillouin zone. If the force is large in comparison to the energy gap between the two lowest bands, this creates a coherent superposition of the two bands

$$|\psi_{\Gamma'}\rangle = a_1 |\psi^1_{\Gamma'}\rangle + a_2 |\psi^2_{\Gamma'}\rangle \,. \tag{3.27}$$

At this quasimomentum, the atoms are held in the superposition for a time t_{hold}, such that they acquire a phase according to

$$|\psi_{\Gamma'}\left(t_{\text{hold}}\right)\rangle = a_1 |\psi^1_{\Gamma'}\rangle \, e^{-iE^1_{\Gamma'} t_{\text{hold}}/\hbar} + a_2 |\psi^2_{\Gamma'}\rangle \, e^{-iE^2_{\Gamma'} t_{\text{hold}}/\hbar}, \tag{3.28}$$

with $E^1_{\Gamma'}$ and $E^2_{\Gamma'}$ being the energy of the lowest and first excited band at quasimomentum Γ'. Driving the atoms back nonadiabatically to the initial quasimomentum, one again obtains a superposition:

$$|\tilde{\psi}_\Gamma\left(t_{\text{hold}}\right)\rangle = a_1 e^{-iE^1_{\Gamma'} t_{\text{hold}}/\hbar} \left(b_1 |\psi^1_\Gamma\rangle + b_2 |\psi^2_\Gamma\rangle\right) + a_2 e^{-iE^2_{\Gamma'} t_{\text{hold}}/\hbar} \left(c_1 |\psi^1_\Gamma\rangle + c_2 |\psi^2_\Gamma\rangle\right) \tag{3.29}$$

The population in the lowest band of the system is now

$$\begin{aligned} N_0\left(t\right) &= \left|\langle\psi^1_\Gamma|\,|\tilde{\psi}_{\Gamma'}\left(t_{\text{hold}}\right)\rangle\right|^2 \\ &= \left|e^{-iE^1_{\Gamma'} t_{\text{hold}}/\hbar}\left(a_1 b_1 + a_2 c_1 e^{-i\left(E^2_{\Gamma'} - E^1_{\Gamma'}\right) t_{\text{hold}}/\hbar}\right)\right|^2 \\ &= \left|a_1 b_1\right|^2 + \left|a_2 c_1\right|^2 + 2\left|a_1 b_1 a_2 c_1\right| \cos\left(\left(E^2_{\Gamma'} - E^1_{\Gamma'}\right) t_{\text{hold}}/\hbar + \phi\right) \end{aligned} \tag{3.30}$$

We can measure the population in the lowest band by performing a band mapping measurement [187]. For this, we ramp down the lattice adiabatically, so on a time scale slow with respect to the energy gap of the lattice, but fast compared to the tunneling in the lattice to prevent momentum redistribution. Subsequently, we perform a time-of-flight measurement. An exemplary absorption picture taken after 3.5 ms is shown in Fig. 3.11b: Here, the population in the lowest-lying band of the system is located at the center, marked by a grey dashed circle. The surrounding circles contain the population in the first excited band of the system. We can now repeat this measurement for varying hold times t_{hold}, observing an oscillation with frequency $\left(E^2_{\Gamma'} - E^1_{\Gamma'}\right) t_{\text{hold}}/\hbar$ in the population of the lowest band, allowing us to determine the energy gap $\Delta E_{\Gamma'} = E^2_{\Gamma'} - E^1_{\Gamma'}$. To calibrate the lattice depth, we then compare the result to numerical data extracted from a six-band model. An exemplary measurement yielding $\Delta E = 6.54(1)$ kHz, corresponding to a $6.08\,E_{\text{rec}}$ deep lattice, is shown in Fig. 3.11c. This technique can be applied analogously to determine the energy gap at any arbitrary quasimomentum, with energy gap measurements at different quasimomenta shown in the supplementary information of [61].

3.4 Imaging

To gather information about the system under investigation, ultracold atom experiments typically rely on taking images. The two primary approaches are absorption imaging and fluorescence imaging. Absorption imaging measures the shadow cast by atoms when a resonant probe beam passes through the atomic cloud, providing direct access to the column density of the system. This technique is particularly well-suited for imaging large ensembles and for performing time-of-flight measurements [132, 182, 188–190].

Fluorescence imaging, by contrast, collects photons scattered by atoms which are being excited by a resonant imaging beam, using an objective with a large numerical aperture (NA). This technique is especially suitable for the detection of individual atoms [191, 192], and has been essential for the development of quantum gas microscopy [47, 193–196] and the imaging of individual atoms in tweezer arrays [53, 54, 197–201].

In recent years, additional techniques, which achieve even better resolution with larger depth of field have been developed, using an electron microscope [202] or an ion microscope [203], or by magnifying the system before performing absorption imaging [204].

In the experiments presented in this thesis, we employ absorption imaging. This technique relies on Beer's law

$$\frac{dI}{dz} = -n\left(x,y,z\right)\sigma_0 \cdot I, \tag{3.31}$$

where $n\left(x,y,z\right)$ is the density of the atomic cloud, σ_0 the scattering cross section, and I the intensity of the imaging beam [128], which is much lower than the saturation intensity of the transition. When a resonant probe beam passes through the atomic cloud, atoms absorb photons proportional to their local density, throwing a shadow which contains information about the spatial distribution of the gas. In this regime, one can extract the column density of the system as

$$n_{\mathrm{col}}(x,y) = -\frac{1}{\sigma_0}\ln\left(\frac{I_{\mathrm{out}}\left(x,y\right) - I_{\mathrm{BG}}\left(x,y\right)}{I_{\mathrm{in}}\left(x,y\right) - I_{\mathrm{BG}}\left(x,y\right)}\right), \tag{3.32}$$

where $I_{\mathrm{out}}(x,y)$ is the intensity of an image taken of the system of interest at location (x,y), $I_{\mathrm{in}}(x,y)$ is the intensity of an image taken without any atoms in the system, and $I_{\mathrm{BG}}(x,y)$ is the intensity of a dark image taken without the imaging beam. Note that this equation is however only valid for imaging intensities much smaller than the saturation intensity I_{sat}.

On the main imaging system, which images the atoms perpendicular to both dipole trap beams, light transmitted through the atomic cloud is collected by a high-resolution microscope objective[31]. The light is then directed through a dichroic[32], and a 500 mm focal length lens[33], which together with the objective form a telescope with a magnification of 20.21(2). Here, images are typically either taken after a time of flight after switching all confining potentials off, and letting the system expand, or in situ, while the atoms are held in the trap.

For time-of-flight imaging, the Feshbach fields are turned off before imaging, allowing us to image at close to zero magnetic field. The imaging frequencies used here are indicated in Fig. 3.1: For both species, we image on the $F = 2$ to $F' = 3$ transition, with atoms in $F = 1$ being pumped to $F' = 2$. As these two lasers form a closed transition, and as the features to be imaged are relatively large, we image for 40 µs.

3.4.1 High signal-to-noise absorption imaging at nonzero magnetic field

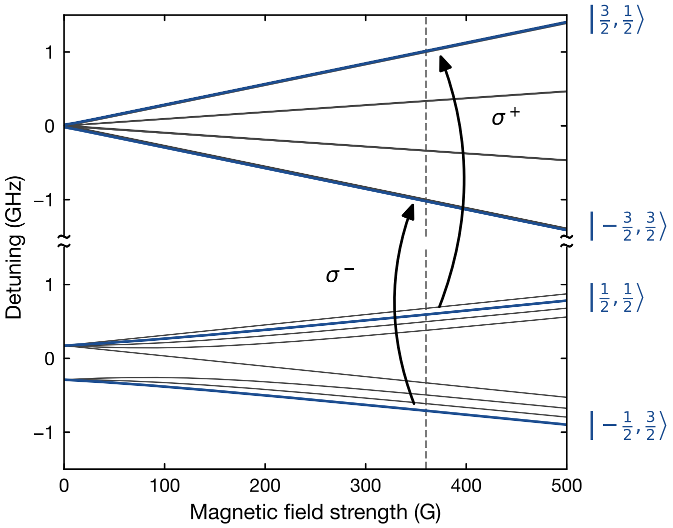

Figure 3.12 | **High-field imaging scheme.** Breit-Rabi diagram of the $4P_{3/2}$ (top) and the $4S_{1/2}$ (bottom) manifold in ^{39}K. The dashed line marks the magnetic field strength we typically work at, 360 G. The curved arrows denote the transitions we drive for imaging here. The states used in our imaging scheme are additionally marked in blue, and their respective quantum numbers $|m_J, m_I\rangle$ are written next to them.

In the experiments presented in Chapter 4 and Chapter 5 of this thesis, we want to work with close to noninteracting atoms, so that we tune the s-wave scattering length between ^{39}K atoms to $a_s = 6a_0$ using the Feshbach resonance at 403 G for atoms in $|F = 1, m_F = 1\rangle$ (described in more detail in Sec. 3.1.3). Having the scattering length at a slightly positive value prevents atom loss, while interactions between the atoms can still be neglected.

---

[31] a custom objective with NA 0.5 and focal length 25 mm manufactured by Special Optics

[32] Optoman PAN3842

[33] Thorlabs AC508-500-B

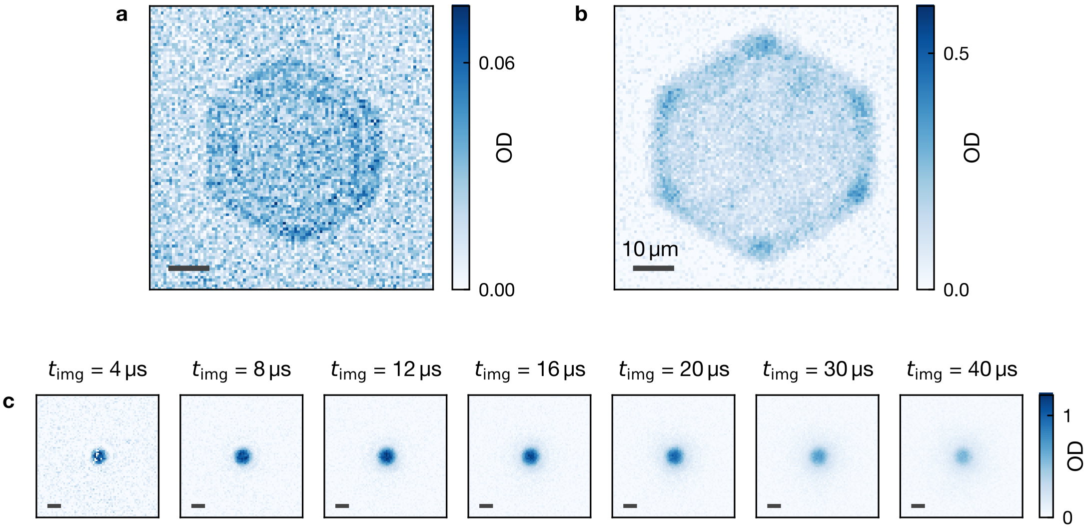

Figure 3.13 | Taking absorption pictures with the high field imaging scheme. a, b Absorption pictures obtained after releasing atoms from the optical tweezer into the amplitude-modulated lattice at $\omega/(2\pi) =$ 16 kHz and $m = 0.25$. **a** shows the average over 45 absorption pictures taken with the old in-situ imaging setup after an evolution time of 3 ms. **b** shows the average over 23 absorption pictures taken with the updated imaging setup after a slightly longer evolution time of 3.75 ms. The scale bar in the bottom left of both figures has a length of 10 µm. **c** Absorption pictures taken 10 µs after releasing atoms from the optical tweezer into the dipole trap. From left to right the imaging duration is varied. Data was taken at an imaging intensity of $2.8 I_{\mathrm{eff}}^{\mathrm{sat}}$. Each picture is averaged over 14 experimental realizations, except the first one, where only 10 shots were used due to file corruption. The scale bar in the bottom left of each figure has a length of 2.5 µm.

While the first experiments on this machine were performed in reciprocal space [61, 69, 186, 205, 206], it is essential for investigating the edge properties of topological systems to be able to resolve their features in real space. Performing experiments at this magnetic field strength however also necessitates imaging at this magnetic field strength – a rampdown of the field would not only be slow in comparison to the timescales present in the experiment, but would also cross a second Feshbach resonance at 26 G, destroying the state to be imaged and which, due to its narrow width, is not suitable for performing measurements.

After performing a measurement utilizing the Feshbach resonance at 403 G, one is in the $|m_J = -1/2, m_I = 3/2\rangle$ state, which adiabatically connected to the $|F = 1, m_F = 1\rangle$ state at low magnetic field. For the measurements presented in Chapter 4, we drova a σ^--transition to the $|m'_J = -3/2, m'_I = 3/2\rangle$ state in the $^2\mathrm{P}_{3/2}$ manifold. Unfortunately, at 403 G we are not yet in the Paschen-Back regime, so that the $|m_J = -1/2, m_I = 3/2\rangle$ in $^2\mathrm{S}_{1/2}$ is not pure, but has a $\sim 2.4\%$ admixture of $|m_J = 1/2, m_I = 1/2\rangle$. This limited the imaging duration to only 4 µs, after which all the atoms occupied a dark state.

To improve the observable signal, we decided to install a second imaging laser driving the $|m_J = 1/2, m_I = 1/2\rangle \rightarrow |m'_J = 3/2, m'_I = 1/2\rangle$ transition, inspired by similar schemes in absorption [207] and fluorescence [208] imaging at large magnetic fields, where a second laser was added to generate a closed optical cycle. The benefit of using this particular transition is, that the $|m'_J = 3/2, m'_I = 1/2\rangle$ state can only decay back to the $|m_J = 1/2, m_I = 1/2\rangle$ state via a dipole transition, closing the cycle in our case, too.

For the work in Chapter 5 this light used for this transition was generated by a separate diode laser[34]. This additional transition requires σ^+ polarized light, while the initial transition uses σ^-. This allows us to combine both beams on a polarizing beam splitter, send them through the same AOM, and couple them into the same polarization-maintaining fiber. We found that an equal power splitting between the two beams leads to a significant improvement in signal-to-noise, as shown in Fig. 3.13b.

To investigate the improvement in accessible imaging duration, we vary the imaging duration, imaging atoms 10 µs after releasing them from the optical tweezer into the dipole trap, as shown in Fig. 3.13c. We find, that for imaging durations longer than 16 µs, the detected optical density drops, and the cloud starts to undergo spatial diffusion, limiting the imaging resolution. We therefore settled on an imaging duration of 15 µs for the measurements in Chapter 5.

3.4.2 Calibration of the absorption imaging

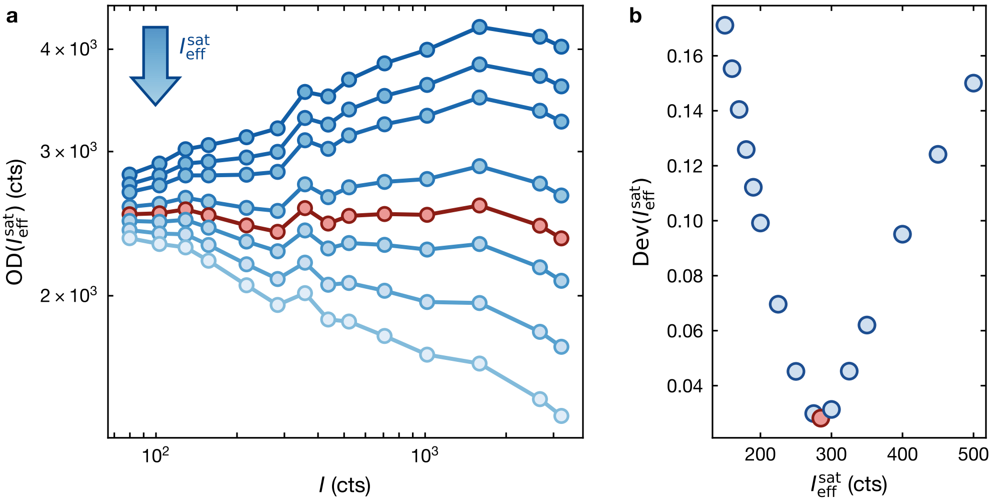

Figure 3.14 | **Imaging calibration a** Optical density of a BEC extracted for varying intensities I of the imaging beam, using Eq. 3.34 for varying parameters $I_{\mathrm{eff}}^{\mathrm{sat}}$. Shown are, from top to bottom, $I_{\mathrm{eff}}^{\mathrm{sat}} = [160\,\mathrm{cts}, 180\,\mathrm{cts}, 200\,\mathrm{cts}, 250\,\mathrm{cts}, 285\,\mathrm{cts}, 325\,\mathrm{cts}, 400\,\mathrm{cts}, 500\,\mathrm{cts}]$. **b** Dev $\left(I_{\mathrm{eff}}^{\mathrm{sat}}\right)$ as defined in Eq. 3.35, evaluated at different values for $I_{\mathrm{eff}}^{\mathrm{sat}}$. The red data in both **a** and **b** marks the data evaluated at $I_{\mathrm{eff}}^{\mathrm{sat}} = 285$ cts, which we use to calibrate our results acquired with the new imaging setup.

---

[34] Toptica DL Pro

Absorption imaging of ultracold quantum gases relies on the Beer-Lambert law, as defined in Eq. 3.31. This equation is, however, only valid for intensities $I \ll I_{\text{sat}}$, where I_{sat} is the saturation intensity of the transition. In this case, the column density of the system can be extracted according to Eq. 3.32.

To achieve the optimal signal-to-noise ratio, it is however typically favorable to use intensities on the order of the saturation intensity, because the interrogation time is limited. In this regime, Beer's law must be modified to

$$\frac{dI}{dz} = -n(x,y,z)\sigma_{\text{eff}} \frac{1}{1 + I(x,y,z)/I_{\text{eff}}^{\text{sat}}} I(x,y,z) \tag{3.33}$$

with $\sigma_{\text{eff}} = \frac{\sigma_0}{\alpha}$ being the effective cross-section, and $I_{\text{sat}}^{\text{eff}} = \alpha I_{\text{sat}}$ being the effective saturation intensity [209]. Integrating this equation along z yields

$$\begin{aligned} \text{OD}\left(x,y\right) &= \sigma_{\text{eff}} \int_{-\infty}^{\infty} n\left(x,y,z\right) dz \\ &= -\ln\left(\frac{I_{\text{out}}\left(x,y\right)}{I_{\text{in}}\left(x,y\right)}\right) + \frac{I_{\text{in}}\left(x,y\right) - I_{\text{out}}\left(x,y\right)}{I_{\text{eff}}^{\text{sat}}} \end{aligned} \tag{3.34}$$

To determine $I_{\text{eff}}^{\text{sat}}$ for the new setup for taking absorption pictures at large magnetic fields, we compared in-situ images of a BEC in a shallow dipole trap taken with varying intensities of the imaging beam, as described in [210]. Here, for the imaging system to be calibrated properly, the observed optical density should be independent of the intensity of the imaging beam. We evaluate Eq. 3.34 for varying values of $I_{\text{eff}}^{\text{sat}}$, as illustrated in Fig. 3.14a. To quantify the dependence of the detected optical density on the ingoing intensity $I_{\text{in}}\left(x,y\right)$, we calculate a weighted relative standard deviation, defined as

$$\text{Dev}\left(I_{\text{eff}}^{\text{sat}}\right) = \frac{1}{\text{OD}_{\text{avg}}} \cdot \sqrt{\frac{\sum_I w_I \left(\text{OD}_I - \text{OD}_{\text{avg}}\right)^2}{\sum_I w_I}}. \tag{3.35}$$

Here, I denotes the intensity at which an optical density has been measured, and the weight

$$w_I = \frac{\text{OD}_{\text{I}}}{\Delta\text{OD}_{\text{I}}} \tag{3.36}$$

is the relative measurement error of this optical density. The error in this measurement $\Delta\text{OD}_{\text{I}}$ has been extracted via bootstrapping. The average detected optical density for a given choice of parameter $I_{\text{eff}}^{\text{sat}}$ is denoted as OD_{avg}, and is determined via a weighted average

$$\text{OD}_{\text{avg}} = \frac{\sum_I w_I \text{OD}_I}{\sum w_I} \tag{3.37}$$

with the same weights as defined in Eq. 3.36.

The evaluation of Eq. 3.35 is shown in Fig. 3.14 for a range of parameters $I_{\text{eff}}^{\text{sat}}$, with a minimum at $I_{\text{eff}}^{\text{sat}} = 285\,\text{cts}$ visible, marked in red. We use this value to calibrate the absorption images taken with the new in-situ imaging setup. When taking data with this imaging system, we typically work at an intesity of $\sim 3.5 I_{\text{eff}}^{\text{sat}}$, as this both still provides a good signal for lower optical densities while being able to reliably determine the peak optical density of atoms just released from the optical tweezer. When studying systems with lower or higher optical densities, the imaging intensity must be adjusted accordingly to achieve a good signal-to-noise ratio.

CHAPTER 4

Detection and manipulation of topological edge states

A remarkable feature of topological systems is, that the topological properties of their bulk are directly tied to the existence of gapless states at the edge of the system, a principle known as the bulk-boundary correspondence [211–216]. Its existence can be understood from the integer quantum Hall effect [5, 6], which exhibits two of its main features: A precisely quantized transverse conductance, as determined by the Chern number $\mathcal{C}$ [16, 217], and the existence of chiral edge modes on the boundary.

In out-of-equilibrium systems, where the Hamiltonian is time-dependent, a generalized form of the bulk-boundary correspondence predicts edge states even in situations, where the Chern number of the bulk band vanishes. Such systems have been realized in photonic waveguides [91, 92], resonator arrays [93, 94, 97] as well as in cold atoms [61].

To study the bulk properties of topological systems on ultracold atom platforms, a variety of techniques has been developed, using interferometric or state-tomography techniques [68, 69, 71, 186], transport measurements [59, 70, 218] as well as methods based on spectroscopy or quench dynamics [60, 72].

The edge modes of such systems have so far been studied in real-space in photonic, mechanical or electrical devices [219–223], where a sharp natural boundary exists at the edge of the system. On ultracold atom platforms, edge states have been observed in 1D systems using engineered lattices [152, 224] or in Rydberg atom arrays [225]. Alternatively, the concept of synthetic dimensions [226, 227] could be used, treating internal atomic degrees of freedom as a real-space dimension [228–230], with the finite number of coupled levels again providing a naturally sharp boundary. Even though several strategies have been proposed [156, 231–233] for observing edge modes in two real-space dimensions, their experimental realization has remained elusive until recently [79, 234].

This chapter will describe, how we populate the edge mode in three different topological regimes of our driven honeycomb optical lattice, and determine their properties. For this, we start in Sec. 4.1, discussing the sequence and the techniques utilized for populating the edge state in our optical lattice. In Sec. 4.2, we first observe topological edge states in the anomalous Floquet regime of our system, tracking their chiral movement. In Sec. 4.3, we develop a strategy for populating the edge state of the Haldane regime, and optimize the parameters used. Sec. 4.4 cosiders the effects which the height and shape of the topological boundary has on the propagation of the edge state. For this, a method for determining the velocity of the edg state is developep in Sec. 4.4.1. In Sec. 4.4.2 the emergence of the edge state is investigated by varying the height of the topological interfacte, and the relevant energy scales for the different regimes are determined. Finally, Sec. 4.4.3 studies the effect that the width of the topological interface has on the propagation of the edge mode.

> The following chapter is based on the joint work of Christoph Braun, Raphaël Saint-Jalm, Alexander Hesse, Johannes Arceri, Immanuel Bloch and Monika Aidelsburger [79].

4.1 Population of the edge state

The experimental sequence for populating the edge mode of our systems is illustrated in Fig. 4.1a: About 200 weakly interacting ($a_s = 6a_0$) ^{39}K atoms are trapped in an optical tweezer (cf. Sec. 3.2.2). Next to the tweezer, we generate a topological interface, by displaying a binary repulsive pattern on our digital micromirror device (DMD, cf. Sec. 3.2.3). We release the atoms into our optical lattice, while breaking time-reversal-symmetry by modulating the tunneling of the lattice in a chiral manner (cf. Sec. 2.3).

The modulation scheme of our optical lattice allows us, to populate three distinct topological regimes in our experiment, illustrated in Fig. 4.1b: The Haldane-like regime, with $(W^0, W^\pi) = (0, 1)$, the anomalous regime with $(W^0, W^\pi) = (1, 1)$, as well as the Haldane regime with $(W^0, W^\pi) = (1, 0)$. We choose lattice modulation parameters for for each regime, which produce reasonably sized bandgaps in the system: In the Haldane-like regime, we choose $\omega/(2\pi) = 5\,\mathrm{kHz}$, as here the energy gaps in the 0- and in the π-gap are of same size. Similarly, in the anomalous regime $\omega/(2\pi) = 7\,\mathrm{kHz}$ leads to equally sized gaps. In the Haldane regime, where we are approaching the high-frequency limit, the size of the π-gap will not decrease again for increasing modulation frequency, so that we choose as $\omega/(2\pi) = 16\,\mathrm{kHz}$, which leads to a relatively large 0-gap, while simultaneously being well separated from the transition into the anomalous regime. These parameters are marked in the phase diagram by colored hexagons, with the color being used to refer to the regime results were taken in throughout this chapter: Results plotted in green were taken in the Haldane regime, results marked in blue were taken in the Haldane regime, and results in red were taken in the Haldane-like regime. The parameter m in the figure describes tunneling modulation scheme introduced in Sec. 2.3 in terms of an intensity modulation of individual lattice beams. The parameter is chosen to be $m = 0.25$ for all measurements presented in this thesis, but is fully captured by the constants A, B and C in Eq. 2.44.

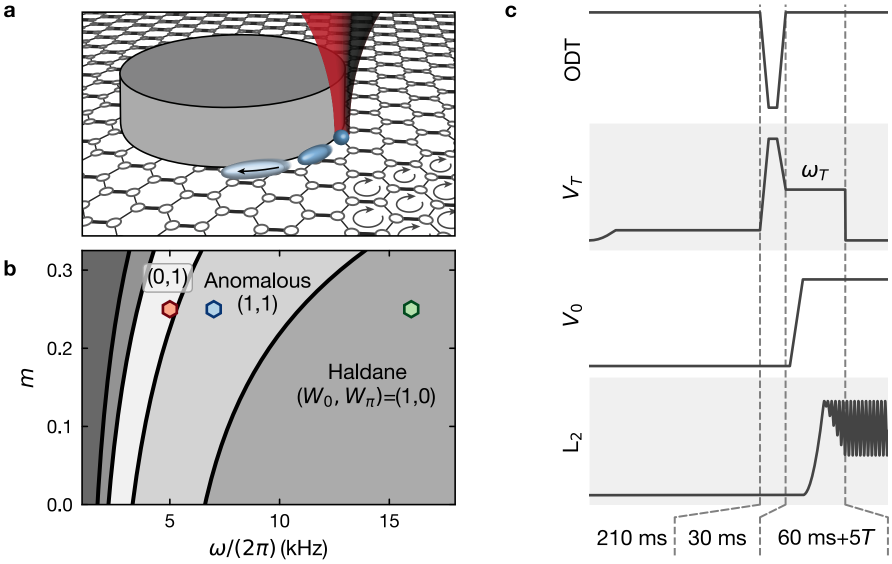

Figure 4.1 | **Populating the edge state a** Illustration of the experimental sequence for populating the edge state: An optical tweezer (red) releases atoms (blue) into the hexagonal optical lattice. The tunneling of the lattice is modulated in a chiral manner, breaking time-reversal symmetry. The location where the atoms are released is close to a topological interface (grey), projected by a DMD. This leads to chiral movement of the atoms along the interface. **b** The three phases we will study as well as the precise modulation parameters we employ are marked in the phase diagram: The Haldane-like with $(W^0, W^\pi) = (0, 1)$ is populated at $\omega/(2\pi) = 5$ kHz, the anomalous regime with $(W^0, W^\pi) = (1, 1)$ is populated at $\omega/(2\pi) = 7$ kHz, and the Haldane regime with $(W^0, W^\pi) = (1, 0)$ is populated at $\omega/(2\pi) = 16$ kHz. **c** The power in the optical dipole trap (labelled ODT), the optical tweezer (V_T), the hard-wall-potential (V_0), as well as in one of the optical lattice beams L_2 is plotted against time. The final trap frequency of the optical tweezer ω_T is marked. After the last dashed line the atoms are abruptly released from the tweezer, such that the evolution begins.

In Fig. 4.1c the time sequence of various optical potentials throughout the preparation of the edge state is shown. We start our sequence with a BEC of ^{39}K in our crossed optical dipole trap. We quadratically ramp up our optical tweezer potential, and hold it at a constant strength for 180 ms to load atoms from the optical dipole trap into the tweezer. The tweezer position is aligned to be centered onto the BEC before measurements are started to ensure a good loading rate, and to later on probe a flat region of our system.

After this, the crossed optical dipole trap is briefly ramped down, while the power in the tweezer is simultaneously increased. This ensures that atoms, which were not transferred into the tweezer, are expelled from the dipole trap, and do not contribute to a background signal. The system is held in this state for 10 ms, with a 10 ms linear ramp in both potentials used for increasing and decreasing the potential.

After this ramp, the optical tweezer is ramped down to its final trap depth $\omega_T/(2\pi) = 2$ kHz unless denoted otherwise. Here, the atoms are held while first the hard-wall potential imposed by the DMD is ramped up to its final value V_0 within 30 ms. After this, the optical lattice is exponentially ramped up to a depth $5.9E_{\mathrm{rec}}$ within 30 ms. The optical lattice potential has, like the optical tweezer, been aligned to be centered onto the BEC before each experimental run, to ensure that the potential landscape probed by the atoms is as flat as possible.

Once all potentials are ramped up, the amplitude modulation of the optical lattice is linearly ramped up within five modulation cycles. Now, the optical tweezer is abruptly switched off to release the atoms, and the system is left to evolve.

4.2 Observation of edge states in an anomalous Floquet system

In Fig. 4.2, the time evolution of the edge state in the anomalous regime at $\omega/(2\pi) = 7\,\mathrm{kHz}$ is shown. For this, the system is prepared as described in Sec. 4.1, with the interface forming a straight potential step with a height $V_0/h = 16.7(3)\,\mathrm{kHz}$. The position of the tweezer with respect to the topological interface was varied before taking data in order to find a good overlap with the edge mode of the system. The evolution time of the system is listed both in ms as well as in multiples of the tunneling in the unmodulated lattice $\tau = \hbar/J_0 = 145\,\mathrm{ms}$ above the absorption pictures, with data in the same column being taken after the same evolution time.

Fig. 4.2a shows the propagation of the system for a lattice modulation with chirality $\kappa = 1$. Here, one initially observes a wavepacket populating few lattice sites close to the topological interface. If the system is left to evolve, this wavepacket starts to propagate along the topological interface, moving upwards as time progresses. Additionally, the wavepacket disperses while propagating. This can be explained by the non-linear dispersion relation of the edge mode, as well as by the finite width of the edge [154–156]. To underline the chiral nature of this propagation, the chirality of the modulation is reversed in Fig. 4.2b. Here, the wavepacket also propagates along the topological interface, this time in the opposite direction.

To further illustrate the chiral nature of the propagation, we additionally evaluate the difference signal

$$\Delta\mathrm{OD} = \mathrm{OD}_{\kappa=1} - \mathrm{OD}_{\kappa=-1}, \tag{4.1}$$

where $\mathrm{OD}_{\kappa=\pm1}$ denotes the optical density obtained at chirality κ. This difference signal is shown in Fig. 4.2c, highlighting the chiral nature of the propagation.

When now comparing the absorption pictures taken at different times, one can see a clear movement along the wall for the atoms – in the system modulated with $\kappa = 1$ the atoms move in positive y-direction, and in the system modulated with $\kappa = -1$ the atoms move in negative y-direction. This becomes even more obvious when looking at the difference signal, which highlights the chiral nature of the movement. Additionally, the edge mode

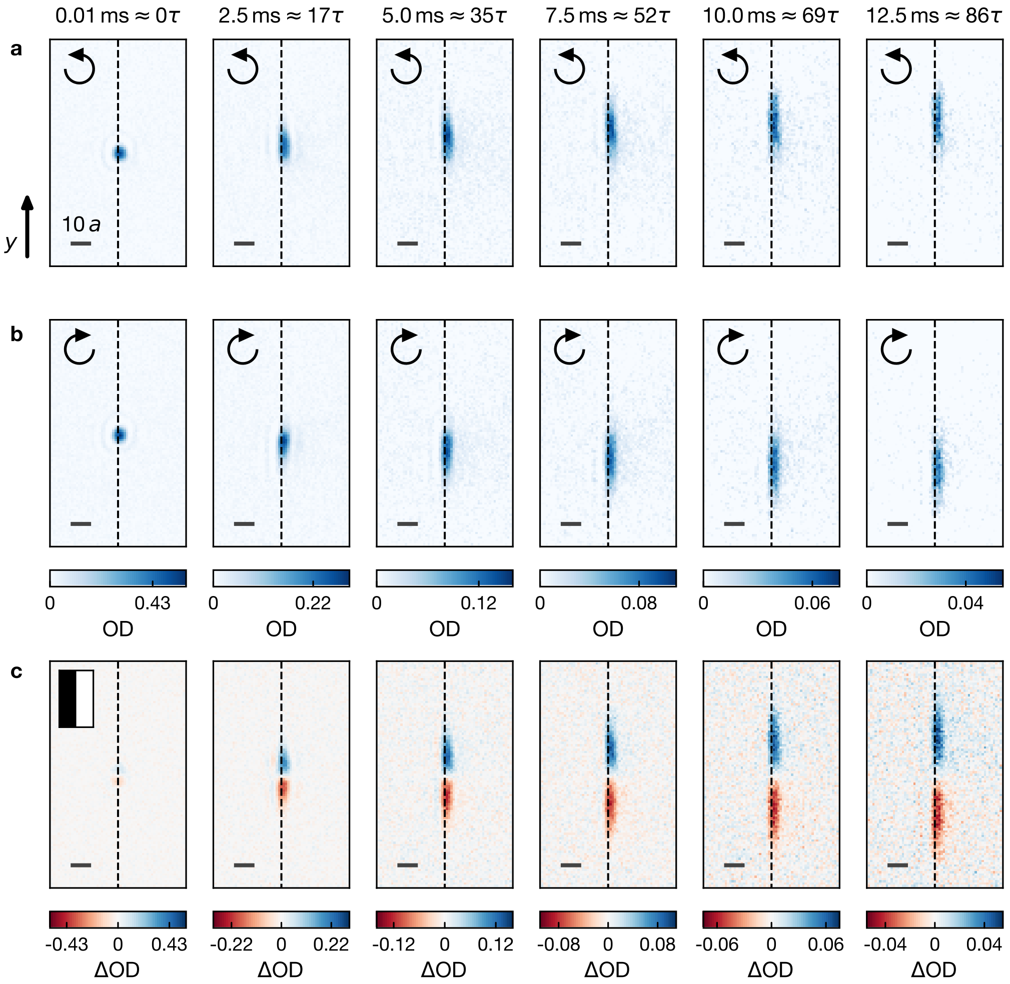

Figure 4.2 | Observing the anomalous edge state Absorption pictures obtained after releasing the atoms next to the topological interface while modulating the optical lattice with chirality **a** $\kappa = 1$ and **b** $\kappa = -1$. **c** shows the difference ΔOD between the absorption pictures for both chiralities. Each picture is the average over 100-300 experimental realizations. The arrow in the upper left corner of **a** and **b** marks the chirality of the tunneling modulation, while the inset in the upper left corner of the first difference picture displays the mask projected onto the atoms via the DMD, with dark areas marking the regions of higher potential energy. The scale bar has length $10a = 2.87$ µm, and the vertical dashed line indicates the location of the topological interface. The evolution time is both indicated in ms, and in multiples of the tunneling in the unmodulated lattice τ.

disperses while propagating. This is an effect due to the finite width of the hard wall potential, leading to a non-linear dispersion relation for the edge mode [154–156]. In this measurement, the atoms propagate on average over more than $20a$, not scattering into the bulk, which is indiciative of the preparation protocol providing a good overlap with the edge state of the syste.

As in principle also external forces or gradients in the system could mimick the behavior of the edge mode, we also investigate the propagation of the edge mode in other geometries.

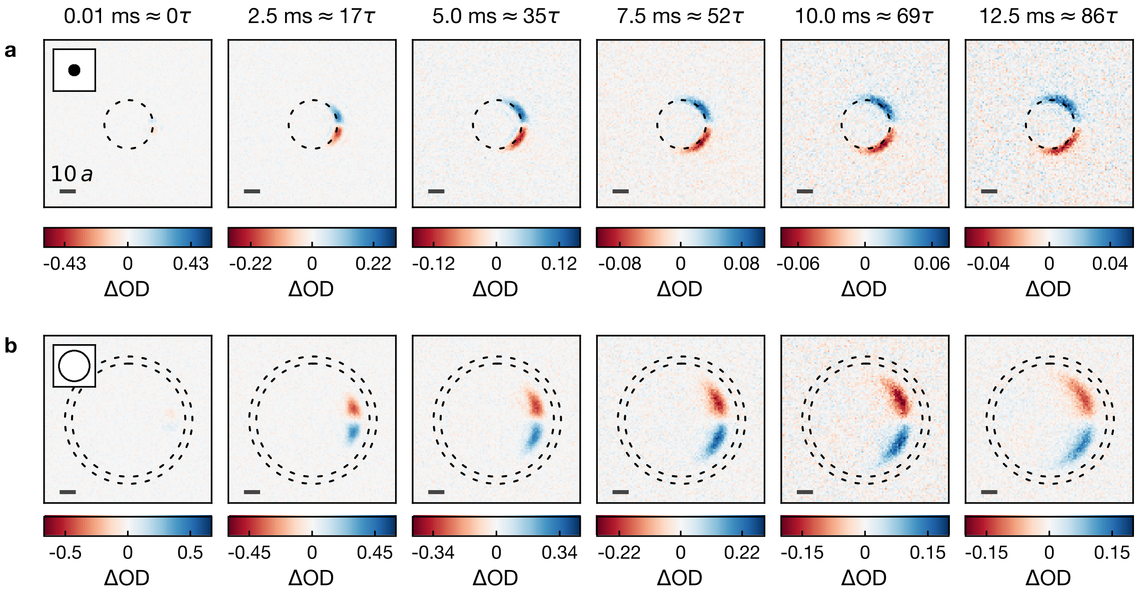

Figure 4.3 | Anomalous Edge state on the outside of a disk and inside a confining ring Difference pictures ΔOD of the edge state in the anomalous regime obtained when preparing the edge state **a** on the outside of a repulsive disk, and **b** inside a repulsive ring potential. The potential is indicated by the dashed lines, with the inset in the top left of the first difference pictures displaying the mask projected into the atomic plane by the DMD, with black regions corresponding to a higher potential energy. All scale bars have length $10a$. The evolution time is both given in ms as well as in multiples of the tunneling τ in the unmodulated lattice. Note, that the optical densities for the measurements in **b** are significantly larger, as the improved in-situ imaging system described in Sec. 3.4.1 was utilized here. The data in **a** is averaged over 100-300 absorption pictures per chirality, while **b** only required 40-160 averages due to the improved imaging system.

In Fig. 4.3a, the wavepacket was not initialize on a straight wall, but insteaad placed on the outside of a disk with a diameter of $11.6\,\mu\mathrm{m} \approx 40a$, with a potential height of $V_0/h = \cdot 16.7(3)\,\mathrm{kHz}$. The geometry of this potential is illustrated both by a dashed line in all difference pictures as well as by a mask displayed as an inset in the first difference picture.

Here, we again observe chiral propagation of the atoms, with the measurements at $\kappa = 1$ leading to a counterclockwise propagation of the atoms, and $\kappa = -1$ to a clockwise propagation. Even though the disk does not cut the lattice in any specific way, the fastest atoms propagate over $9\,\mu\mathrm{m} \approx 31a$, demonstrating the robustness of the edge mode to imperfections in the lattice potential, and to backscattering.

In Fig. 4.3b, the results of a similar measurement are displayed, with the edge state being populated on the inside of a ring potential with a diameter of $\sim 27\,\mu\mathrm{m} \approx 94a$, illustrated by the mask inset and dashed lines in the difference pictures. The potential height of the ring is $V_0/h = 17.0(3)\,\mathrm{kHz}$. Here, the confining potential is situated to the right of the initial location of the wavepacket, this leading to clockwise propagation for $\kappa = 1$, and counterclockwise propagation for $\kappa = -1$. This underlines that the evolution of the system is driven by the topological properties of the Bloch bands, and not by external forces or a gradient driving Bloch oscillations, as this would lead to equal propagation on both sides of the wall.

4.3 Populating the edge state in the Haldane regime

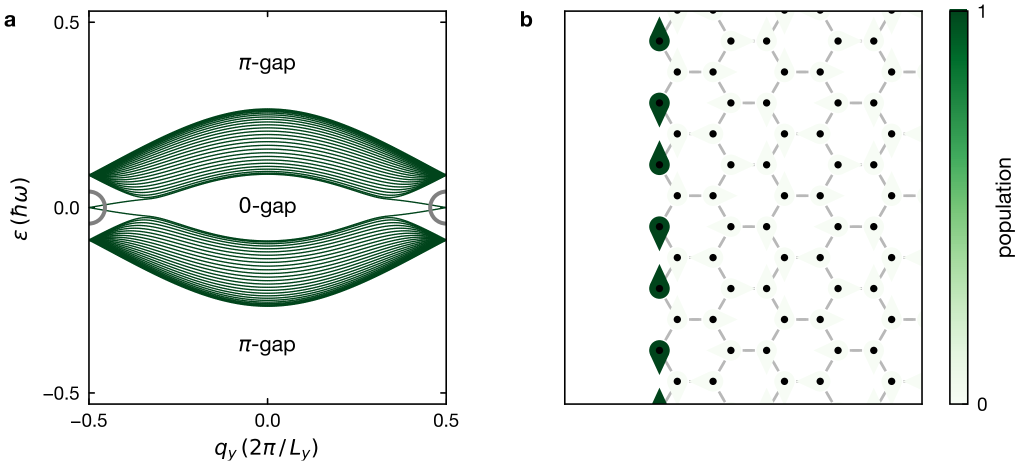

Figure 4.4 | **Edge states in the Haldane regime a** Dispersion of a Haldane system evaluated on a semi-infinite strip, terminated with a zigzag edge in the finite direction. The edge modes, wich are encircled, are situated at the edge of the Brillouin zone. **b** The edge state in the center of the circle is illustrated on the lattice. Here, the hue of the arrows encodes the population of the state on each lattice site, while its direction illustrates the phase.

So far, the population of the edge modes in the anomalous regime was demonstrated, where $W^0 = 1$ and $W^\pi = 1$. The Haldane regime with $W^0 = 1$ and $W^\pi = 0$, does not exhibit an edge state in the π-gap of the system any more, but instead only has an edge state in the 0-gap. However, the edge mode in the 0-gap is located near the edge of the Brillouin zone, as shown in Fig. 4.4a. To understand the effect this has on the lattice site population, the state located exactly at the edge of the Brillouin zone has been illustrated in Fig. 4.4b: Here, each lattice site is marked by an arrow, where the hue marks the population of the state on this site, while the phase of the state is encoded in pointing direction of the arrow.

Releasing the atoms from a relatively large tweezer, which places atoms on several lattice sites with identical phase, will clearly not yield a good overlap of the initial state with the edge mode. To improve the overlap, a nonadiabatic kick can be applied by abruptly moving the tweezer along the topological interface in y-direction, releasing the atoms immediately after this kick.

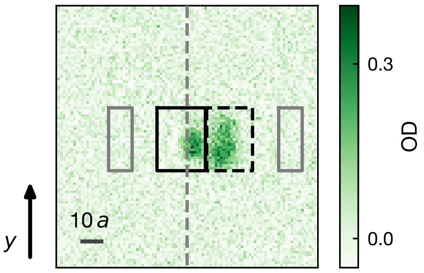

Figure 4.5 | Evaluation of the edge state fraction Averaged absorption picture taken of the edge state in the Haldane regime after 1.5 ms evolution time with a tweezer trap frequency $\omega_T/(2\pi) = 1.3(1)$ kHz and a phase gradient of 0.38 π/a applied. The picture is the average over 5 experimental runs. The drawn in boxes show the edge state signal region (black continuous line), the bulk region (black dashed line), and the background region (grey continuous line) used for evaluating the fraction of atoms populating the edge state. The background region consists of two separate regions which have the same combined size as the other two. A dashed line indicates the location of the topological interface.

The fraction of atoms in the edge mode can be extracted from absorption pictures to deterministically find settings which produce a good overlap, as illustrated in Fig. 4.5. Here, an exemplary absorption picture taken after a 1.5 ms evolution time at a lattice tunneling modulation frequency of $\omega/(2\pi) = 16\,\mathrm{kHz}$ is shown. For the preparation of the illustrated state, a tweezer trap frequency of 1.3(1) kHz was used in combination with a kick yielding a phase gradient of $0.38\pi/a$ along the topological interface. The height of the topological interface was chosen to be $V_0/h = 2.2(1)\,\mathrm{kHz}$.

To quantify the atom number populating the edge mode, the optical density is integrated inside a region close to the wall, illustrated by a black box, yielding signal S_{edge}. As atoms populating bulk states are well separated from the edge state after this evolution time, their optical density can be determined by integrating a separate region, marked by a dashed box (yielding signal S_{bulk}). To ensure that the precise choice of region does not influence the measured signals, it was ensured that the extracted signal remains constant with small variations of the size of the regions.

Additionally, the integrated optical density in a region where no atoms are present is subtracted to prevent shifts due to a constant offset in the images. This region is marked by two grey boxes in Fig. 4.5, and is in the following denoted by S_{BG}. This allows to extract the fraction of atoms populating the edge state according to

$$p_{\mathrm{edge}} = \frac{S_{\mathrm{edge}} - S_{\mathrm{BG}}}{(S_{\mathrm{edge}} - S_{\mathrm{BG}}) + (S_{\mathrm{bulk}} - S_{\mathrm{BG}})}. \tag{4.2}$$

Fig. 4.6a shows the obtained fraction of atoms populating the edge mode for varying phase gradients. The potential step height was chosen to be $V_0/h = 2.2(1)\,\mathrm{kHz}$ for all measurements.

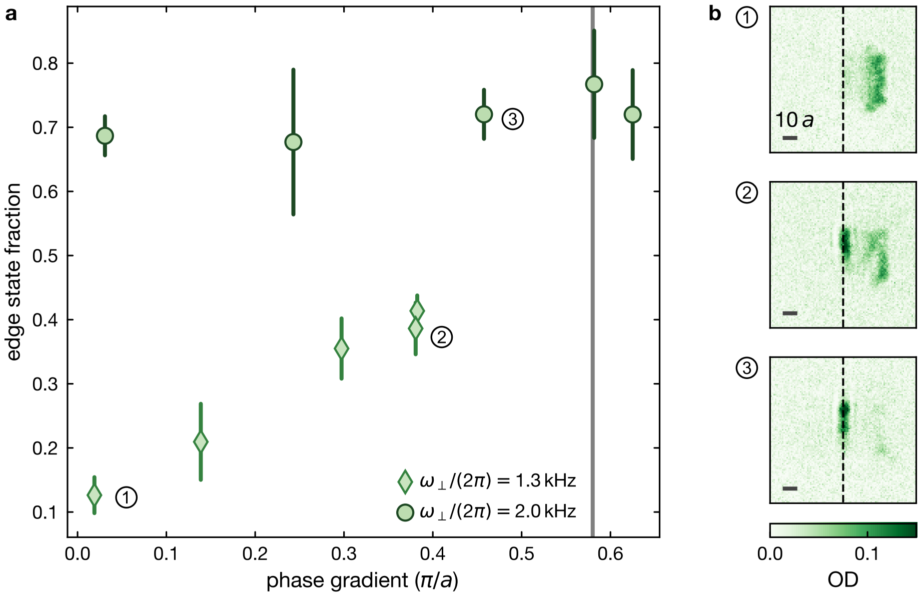

Figure 4.6 | Tuning the wavepacket phase gradient a Fraction of the atoms populating the edge state after 1.5 ms plotted against the phase gradient applied by nonadiabatically moving the tweezer before releasing the atoms. The diamond shaped data points have been taken at a tweezer trapping frequency $\omega_T = 1.3(1)$ kHz, the round data points have been taken at $\omega_T = 2.0(1)$ kHz. The grey line indicates the edge of the Brioullin zone $k_y = \pi/L = \pi/(\sqrt{3}a)$, where the edge state in the zero gap is centered. Each data point is the average over 4-5 experimental realizations. **b** Averaged absorption pictures taken after an evolution time of 3 ms at the same settings as a data point, indicated by a number marker. Each picture is the average over 88-90 experimental runs. All pictures were taken for $\kappa = 1$, with the dashed lines marking the location of the topological interface, and scale bars having length $10a$.

We start our investigation by tracking the edge state fraction, using a tweezer trap frequency $\omega_T = 1.3(1)$ kHz, as this trap frequency was initially used for populating the anomalous edge state, yielding a strong signal. If no phase gradient is applied, the overlap with the Haldane edge state is however negligible. This can be understood in terms of the tweezer populating multiple lattice sites with identical phase, leading to a vanishing overlap with the edge mode in the 0-gap. By introducing a phase gradient into the wave packet however, this overlap can be increased, up to the data point at a phase gradient of $0.39\pi/a$. At this point, the anharmonicity of the tweezer trap leads to atom loss, preventing the application of a stronger kick.

As the edge of the Brillouin zone is located at $1/\sqrt{3}\pi/a \approx 0.58\pi/a$, increasing the trap frequency of the tweezer to apply stronger phase gradients is a logical next step. In the data taken at $\omega_T/(2\pi) = 2.0(1)$ kHz one indeed observes the maximum overlap of the wave packet with the edge mode at a phase gradient of $0.58\pi/a$. However, for all applied phase gradients, a strong overlap with the edge state is visible. We interpret this as an effect of the reduced extent of the wavefunction, as when approaching a single populated lattice site,

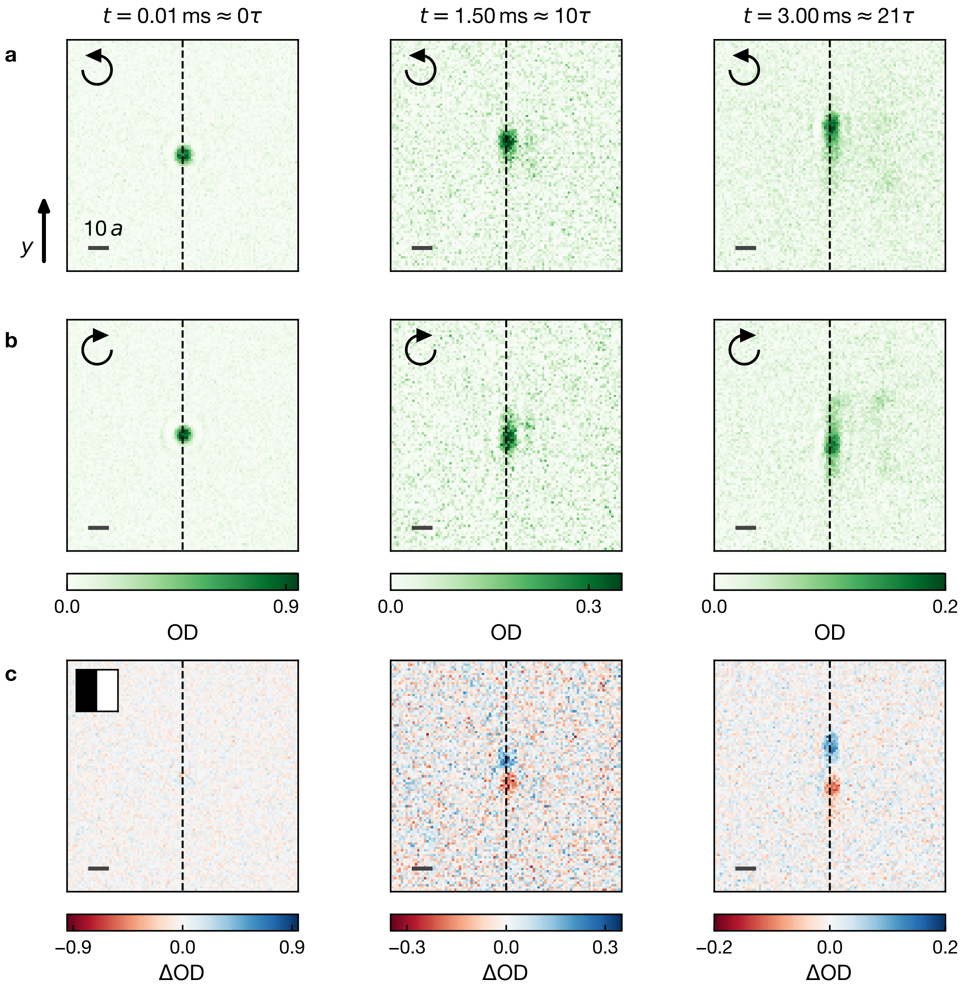

Figure 4.7 | Observation of edge states in the Haldane regime Absorption pictures as well as difference picture of the edge states at a lattice amplitude modulation frequency of $\omega/(2\pi) = 16$ kHz. Each picture is the average over 4-90 individual experimental realizations. **a** shows data taken for chirality $\kappa = 1$, **b** shows $\kappa = -1$, and **c** shows the difference ΔOD of the two. The evolution time of the system is varied, displaying data taken after 0.01 ms, 1.5 ms and 3 ms. The arrow in the upper right corner indicates the chirality $\kappa = \pm 1$ of the lattice modulation. The dashed line marks the location of the topological interface, and each scale bar has a length of $10a$.

the phase gradient between neighbouring lattice sites is not well defined anymore. This feature will be significant for the results presented in Chapter 5 of this thesis, as this allows us to distinguish the anomalous Floquet- and the Haldane regime simply by populating the edge mode of the system with different tweezer trap frequencies.

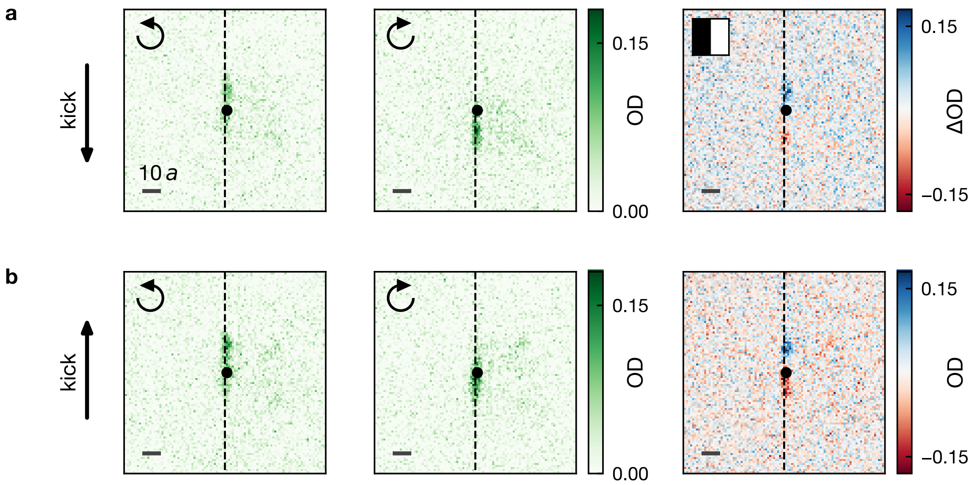

Figure 4.8 | **Reversing the kick direction** Absorption pictures as well as difference picture obtained after an evolution time of 3 ms in the Haldane regime, at $\omega/(2\pi) = 16$ kHz. The direction of the kick is varied, with **a** showing data for the kick being applied down and **b** up along the wall. The phase gradient imposed by the tweezer kick is $k_y \approx \pm 0.43\pi/a$. The straight arrow on the left indicates the direction of the kick, and the curved arrow in the absorption pictures indicates the chirality of the lattice amplitude modulation $\kappa = \pm 1$. The dashed line marks the location of the topological interface, and the scale bar has a length of $10a$.

The validity of the evaluation method defined in Eq. 4.2 is further underlined by the absorption pictures shown in Fig. 4.5b. Here, each absorption picture taken for the same settings as a data point in Fig. 4.5a, with pairs numbered. For the shallow tweezer trap with no kick applied, no atom fraction in the edge mode of the system is discernible, and all atoms are well separated from the wall, populating bulk states. If a kick is applied for the shallow tweezer, a fraction of the atoms is transferred into the edge state of the system, while the remaining atoms still populate bulk states. If the deep optical tweezer is used in combination with a strong kick, basically all atoms populate the edge state of the system, with only a minor fraction leaking into the bulk.

This result allows us, to now reliably populate the edge state in the Haldane phase, too. As Fig. 4.6b only displays the propagation of the system for $\kappa = 1$ and at fixed time, we investigate the chiral nature of the transport in Fig. 4.7. In the measurements displayed here, we prepare the edge state using the tweezer trap frequency $\omega_T/(2\pi) = 2.0(1)\,\mathrm{kHz}$ while applying a phase gradient of $0.45\pi/a$. The kick used for generating the phase gradient is applied in positive y-direction for all measurements.

In Fig. 4.7a, the propagation of the wave packet for chirality $\kappa = 1$ is shown. The measurement displays a good overlap with the edge state, with all atoms staying in the vicinity of the potential step, and moving up the wall potential. For $\kappa = -1$, shown in Fig. 4.7b, the atoms move in the opposite direction, such that in the difference picture in Fig. 4.7c the chiral transport is clearly visible.

While this measurement already implicitly showed, that the direction the momentum kick is applied to does not impact the direction in which the wave packet propagates, we investigate this behavior explicitly in Fig. 4.8. Here, the edge state is populated using the same parameters as before, observing the system after an evolution time of 3 ms. In Fig. 4.8a, the kick is applied in negative y-direction, while in Fig. 4.8b, the kick is applied in the oppsite direction. Independently of the direction of the kick, chiral movement can be observed along the topological interface. This illustrates, that while applying a kick can be helpful to engineer an overlap with the correct quasi momentum, it is the chirality of the lattice modulation, and not the direction the kick is applied to, which determines the subsequent movement in the edge mode.

4.4 Varying the edge properties

In most experimental platforms investigating the behavior of topological edge states, a sharp natural boundary serves as the topological interface, along which the edge states can propagate [219–223, 228–230]. While this clearly simplifies the state preparation, our experimental platform allows us to study the behavior of the edge mode, if the properties of the topological interface are changed. In the following, we will discuss how the velocity of the edge mode can be extractedin Sec. 4.4.1. We will then use the velocity as an observable while the height of the potential step forming the topological interface is varied, investigating the relevant energy scale for the emergence of the edge state in three different topological regimes in Sec. 4.4.2. We will further investigate, how the width of the topological interface influences the velocity of the edge mode in the Haldane regime in Sec. 4.4.3.

4.4.1 Determining the edge state velocity

To systematically investigate the propagation of the edge state under changing properties of the topological interface, it is necessary to define a good observable. For this, we extract the velocity of the transport in the edge channel, as illustrated in Fig. 4.9. Fig. 4.9a shows five different initial tweezer positions at which the system is probed, i.e. in steps of 0.48 µm in x-direction. Even though the location of the topological interface is marked by a dashed line, this potential was turned off for taking this data, so that the location of the wavepacket is not affected by it.

At each of these location, we take data at three evolution times, shown exemplarily in Fig. 4.9b and c for the chiralities $\kappa = 1$ and $\kappa = -1$, respectively. This data was taken in the anomalous Floquet regime, at a tunneling modulation frequency $\omega/(2\pi) = 7\,\mathrm{kHz}$, using a potential step height $V_0/h = 19.0(3)\,\mathrm{kHz}$. We extract the location of the atomic cloud for each time via a Gaussian fit. To quantify the error made in this position estimate, we employ a bootstrapping scheme: From a set of N images taken with the same parameters, we randomly draw N images, where repetitions are possible. We then evaluate the position

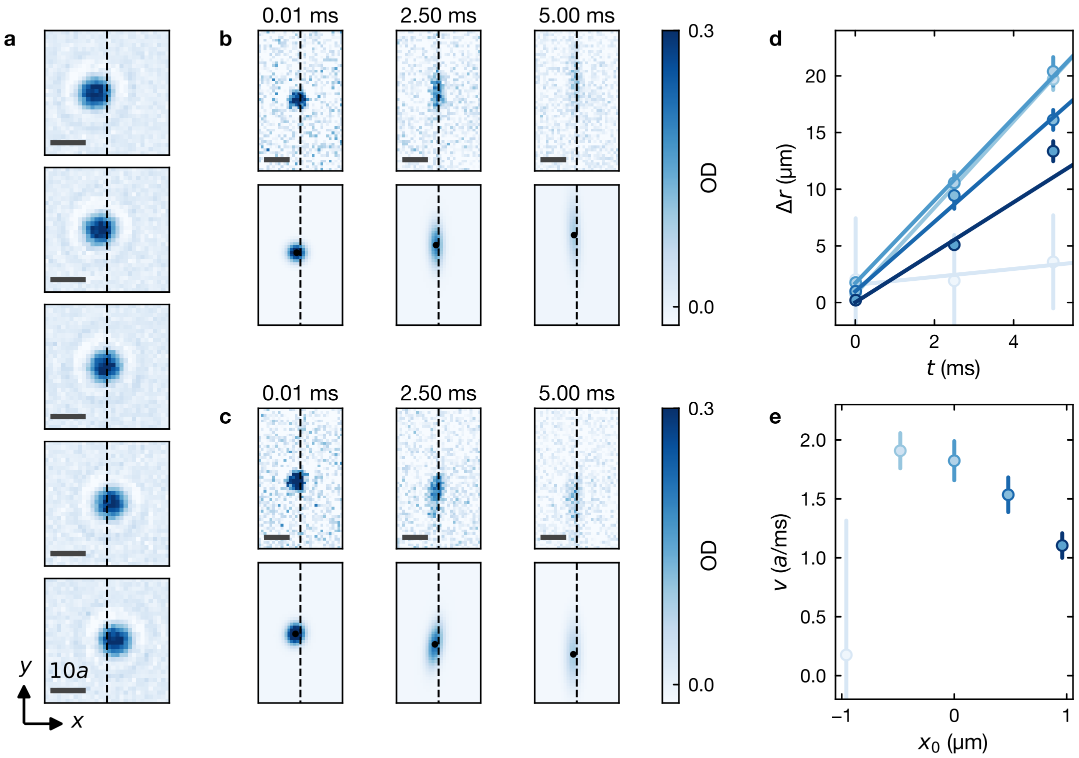

Figure 4.9 | **Determining the edge state velocity a** Absorption picture of the initial wavepacket 10 μs after release from the tweezer at five different positions perpendicular to the topological interface, increasing in steps of 0.48 μm in x-direction. **b, c** Exemplary absorption pictures on the top row as well as Gaussian fits to the atomic cloud on the lower row for **b** $\kappa = 1$ and **c** $\kappa = -1$. The black point in the fit marks the central position of the fitted Gaussian. The scale bar in the bottom left of each image has length $10a = 2.87$ μm. The dashed line indicates the location of the topological interface. **d** The distance between the centers of the Gaussian fits is plotted against the evolution time of the system for the 5 different initial positions perpendicular to the wall, being spaced by 0.48 μm. Error bars are extracted via bootstrapping. The solid lines are linear fits to the data taken at each initial position. **e** The velocity extracted via the linear fit is plotted against the initial position. The error bars are the fit error.

of the atomic cloud via a Gaussian fit. We repeat this procedure 20 times, and take the standard deviation of the results obtained this way to be the error in determining the clouds central position.

The distance Δr between the positions measured for opposite chirality but otherwise identical parameters is shown in Fig. 4.9d. As the distance between the clouds grows linearly with time, we can perform a linear fit of form $\Delta r\,(t) = a + bt$ to the measured positions, and this way extract the velocity of the edge mode.

When plotting the velocity of the edge mode against the position perpendicular to the wall, as done in Fig. 4.9e, there is a clear maximum visible, with the edge transport slowing down when moving further away from the interface. For the data taken closest to the wall, the atoms were placed on top of the topological interface, leading to atom loss, and localization of the remaining atoms in the speckle on top of the potential step. For investigating the transport properties along the wall, we then use the data taken at the location showing the largest transport velocity.

4.4.2 Varying the edge height

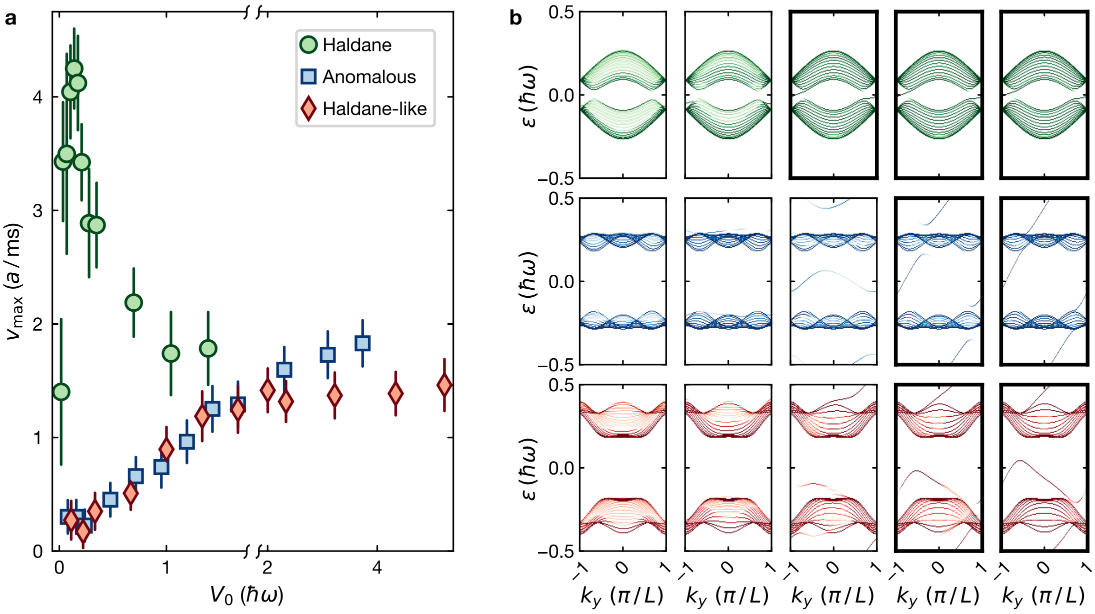

Figure 4.10 | Emergence of the edge state with increasing potential step a The height of the potential step applied to the system is varied for an edge state prepared in the Haldane-like regime ($\omega/(2\pi) = 5$ kHz), the anomalous Floquet regime ($\omega/(2\pi) = 7$ kHz), as well as the Haldane regime ($\omega/(2\pi) = 16$ kHz). The data shown is the average of three data sets taken separately, the error bars are estimated as the fit error for the velocity determination for the individual data sets, and are combined with the standard deviation of the results of the different data sets. **b** Quasi energy spectrum simulated on a step-wise modulated, quasi-infinite system. The system has an infinitely sharp potential step of height V_0 applied along the center in the infinite direction of the system. The potential steps illustrated are, from left to right, $V_0/(\hbar\omega) = [0.05, 0.1, 0.5, 1.5, 2.5]$. Spectra, in which we believe an edge state can be identified are highlighted by a black frame.

When two topologically distinct materials are brought into contact, edge modes arise – the most common example being the transition from a topologically non trivial system to a trivial system at its edge. In experiments on ultracold quantum gases, the natural edge of the optical lattice is very large, leading to a smooth confinement which makes observing edge modes on it hard.

Instead, we employ a potential step generated via a DMD, allowing us to create sharp interfaces. Even though both subsystems on the two sides of the step ideally have the same topological properties, a similar interface can be created if the energy difference between the subsystems is large enough. We study this effect in the three different topological regimes, using the parameters for the tunneling modulation scheme illustrated in Fig. 4.1b: We probe the Haldane regime at $\omega/(2\pi) = 16\,\mathrm{kHz}$, the anomalous regime at $\omega/(2\pi) = 7\,\mathrm{kHz}$, and the Haldane-like regime at a modulation frequency $\omega/(2\pi) = 5\,\mathrm{kHz}$.

In Fig. 4.10a the velocities measured for different wall heights are displayed.

In the Haldane regime, a rapid initial increase in transport velocity can be observed. The velocity exhibits a local maximum at a potential step height $V_0 =\approx 0.14\hbar\omega$, matching the characteristic energy scale of the tunneling in the modulated lattice. If the potential height is further increased, this velocity however decreases again. We expect, that this is due to the intensity profile of the step potential having a smaller slope at the bottom, effectively reducing the sharpness of the potential step as its height is increased. Additionally, corrugations at the bottom of the potential might further slow down transport.

In the anomalous Floquet regime, the velocity shows a fundamentally different response to the height of the potential step: Here, a rather slow increase of the velocity can be observed, starting to flatten off as the potential height reaches a value of $V_0 \approx 2\hbar\omega$. Similar behavior can be observed in the Haldane-like regime, where the velocity exhibits a stable plateau for $V_0 \geq 2\hbar\omega$.

To support these experimental results, we numerically simulate the quasi-energy spectrum of our system in a tight-binding model realizing a stepwise modulation of the tunnelings. For this, we consider a quasi-infinite strip, with the zig-zag edge of the system being terminated in the finite direction. The potential energy of half the system is increased by a value V_0, forming a potential step, separating the system in two along the finite direction. The eigenenergies of this system in the low-potential region are shown for $V_0 = [0.05, 0.1, 0.5, 1.5, 2.5]\,\hbar\omega$, extracted by projecting onto the low-potential region of the system, with the color at each point in the spectrum encoding the overlap. As the height of the potential step increases, one can now see the edge state emerge. In the Haldane regime, the edge state in the 0-gap is fully developed from $V_0 = 0.5\hbar\omega$ on, in agreement with our experimental observation. At this potential height, no edge mode is visible in both the anomalous-Floquet as well as in the Haldane system. Instead, the edge mode appears to develop around $V_0 = 1.5\hbar\omega$, supporting our experimental results. The spectra, in which we believe that edge modes can clearly be identified, are highlighted by a black frame.

These measurements illustrate the different behavior of Floquet-driven systems for modulation frequencies larger (as in the Haldane regime) and smaller (as in the anomalous- and the Haldane-like regime) than the system's bandwidth: In the Haldane regime, the emergence of the edge transport is governed by the parameters of the static Hamiltonian that the driven system maps to, specifically the effective tunneling. In the anonmalous- and the Haldane-like regime, which have the same effective tunneling as the Haldane system, the energy scale when edge transport emerges is related to the drive frequency of the system, underlining the out-of-equilibrium nature of these systems.

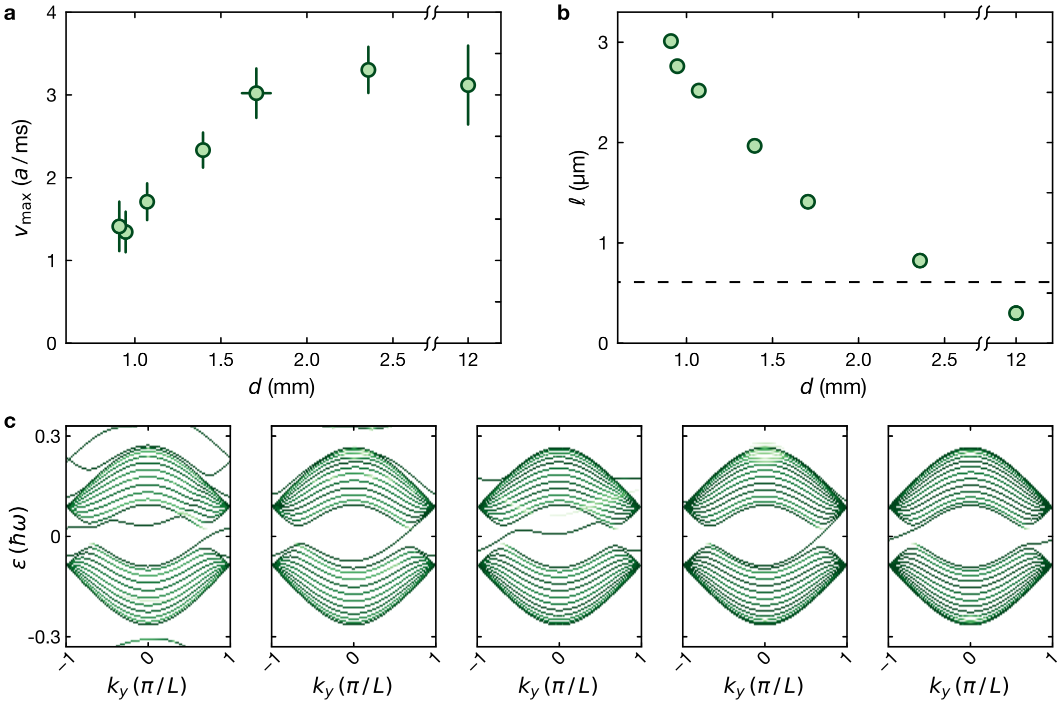

Figure 4.11 | Behavior of edge mode velocity with varying edge width a The edge mode velocity is plotted against the iris diameter. The edge state was populated at $\omega/(2\pi) = 16$ kHz, with a height of the potential step $V_0 = 1.10(2)$ kHz and a tweezer trap frequency $\omega_T/(2\pi) = 2$ kHz applying a phase gradient of $0.43\pi/a$ via a kick. The data shown is the average of three data sets taken independently, and the error bars are estimated as the fit error for the velocity determination for the individual data sets, and are combined with the standard deviation of the velocities extracted on the different data sets. **b** The edge width for a given iris diameter is estimated from measurements of the edge width in an intermediary imaging plane together with the system demagnification. The dashed line indicates the inverse of the largest spatial frequency transmitted through the optical system, and gives a lower bound on the edge witdh achievable. **c** Quasi energy spectrum simulated on a semi infinite strip in a stepwise modulated tight binding model. The edge width is varied from left to right from $l/a = [6, 4, 2, 1, 0.1]$, while the edge height remains fixed at $V_0/(\hbar\omega) = 1.5$. The color of the spectrum encodes the overlap of the states with the low potential region of the system.

4.4.3 Reducing the width of the interface

The width of a topological interface has a large impact on the group velocity of the edge transport [154–156], as the dispersion of the edge modes hybridizes with the bulk modes for finite widths, reducing the transport velocity.

To investigate this effect we tune the width of the hard wall potential by opening and closing an iris in the Fourier plane of the DMD (cf. Sec. 3.2.3). Due to the incoherent illumination of the DMD, closing the iris also leads to a reduction in potential height. To compensate for this, we measure the optical power of the beam after the iris for each iris setting, and readjust it to its initial value. This also means, that only the edge state in the Haldane regime could be probed, as in the other two regimes optical power constraints prevent us from increasing the potential height significantly past the point, where the fastest transport could be observed, cf. Fig. 4.10.

To characterize the width of the potential step, we imaged the projected potential in an intermediary image plane, and extracted the characteristic width ℓ of the potential step, defined as the distance across which the height of the potential increases from 8% to 92% of its maximum value. We divide this length by the demagnification of the following imaging system, which we independently calibrated to be 29.9. The results of this measurements are shown in Fig. 4.11b. As abberations as well as diffraction in this subsequent imaging system are not captured by this measurement, it only gives a lower bound on the actual characteristic width of the potential step in the atomic plane. Another lower bound on the width is given by the diffraction limit of the objective we use for projecting the potential into the atomic plane, which is marked by a dashed line.

In Fig. 4.11a we show the velocity of the Haldane edge state measured at each iris opening. We find, that a larger width of the potential step leads to a reduced velocity of the edge transport, as expected from literature [154–156].

This observation is further supported by numerical simulations of the dispersion of our system in a step-wise modulated tight binding model of a semi-infinite strip, with the zig-zag edge being terminated at the numerical edge in the finite direction. Here, we introduce a potential step with tunable width shaped as an error function, and with a step height $V_0 = 1.5\hbar\omega$. The potential step is oriented along the zigzag direction of the lattice, like in the experimental realization, separating the system in two equal-sized regions in the finite direction. The simulated dispersion for $\ell/a = [6, 4, 2, 1, 0.1]$ is shown in Fig. 4.11c. In the case of a narrow wall width, the edge state just connects the two bands across the edge of the Brillouin zone, as already expected from our simulations utilizing an infinitely sharp edge. For an increasing wall width however, the edge mode starts to hybridize with bulk states, and wraps around the Brillouin zone. This leads to an overall reduced group velocity for the edge transport, supporting our observations.

CHAPTER 5

Disorder-driven phase transitions in Floquet-engineered honeycomb lattices

Topological phases of matter have contributed to our understanding of condensed matter systems, showing that disorder can play an important role in determining material properties beyond being simply an imperfection [13, 14]. As discussed in Sec. 2.5.1, it was previously believed, that disorder prevents electronic transport via a reduced mobility due to diffusive processes, weak localization or Anderson localization [114]. Within the framework of topology however, disorder can even play a stabilizing role, with the paradigmatic example for this being the quantum Hall effect [5–7], where the precise quantization of the observed plateaus in conductivity are not only robust against weak disorder, but in fact require it for their stability [13–15].

The experimental investigation of topological phenomena on platforms working with ultracold atoms in optical lattices pose significant challenges though, as most established techniques for characterizing topological band structures rely on the system's translational invariance, using momentum space measurements to extract the geometric properties of Bloch bands [59, 60, 68, 70–72, 117].

This chapter explores an alternative approach, probing topology directly in real space through the edge modes of the system. As the bulk-boundary correspondence guarantees the existence of these modes at topological interfaces, their robustness against perturbations provides an unambiguous signature of topology that remains valid even when the bulk is disordered.

While disorder-driven phase transitions have been observed between topologically trivial and nontrivial phases [74–78], observations of disorder-driven transitions between distinct topologically nontrivial phases have remained elusive. This chapter reports on the first experimental observation of such a transition. Additionally, we study the systems in the limit of large disorder, observing the transition into a topologically trivial regime.

We begin in Sec. 5.1 by introducing the state preparation method employed, describing a technique to selectively populate the chiral edge modes characteristic of either the anomalous regime or of both the anomalous and Haldane regimes by tailoring the properties of the initial wavepacket using an optical tweezer. This selectivity enables us to distinguish between the two topological phases. Sec. 5.2 investigates the fundamental effect of disorder on topological transport in a Chern insulator. We measure the transport in the edge mode if disorder is applied to the system, and observe a reduced overall transport velocity. In Sec. 5.3, we employ the edge modes of the system to probe and track the location of a topological phase transition. After benchmarking the method against conventional gap-closing measurements in the clean system, we map the phase boundary as a function of disorder strength. Our results reveal that disorder shifts the transition point, demonstrating a disorder-driven phase transition between two topologically nontrivial phases. Sec. 5.4 explores the strong disorder limit, where topological protection eventually breaks down. Here, we observe the transition from topological phases to a trivial localized phase, characterized by the complete suppression of chiral motion. We close the chapter in Sec. 5.5 by observing the expansion and diffusion in the bulk in both the anomalous- and Haldane-regime, if disorder is applied.

> The following chapter is based on the joint work of Alexander Hesse, Johannes Arceri, Moritz Hornung, Christoph Braun and Monika Aidelsburger [80].

5.1 State preparation

The population of the edge state is illustrated in Fig. 5.1a: A small BEC is confined by an optical tweezer (cf. Sec. 3.2.2). Adjacent to the tweezer is a hard-wall potential step, projected by the DMD (cf. Sec. 3.2.3). The atoms are released from the tweezer into the optical lattice (cf. Sec. 3.3), which is amplitude modulated in a time reversal symmetry breaking manner (cf. Sec. 2.3). Subsequently, the atoms populate the edge mode of the system, and perform chiral movement along the wall.

In a past project (cf. Chapter 4, [79]), we employed a kick to transfer quasimomentum to the atoms, which could be used to populate the edge mode in the 0-gap in the Haldane regime. However, in a disordered potential landscape, this method fails. Instead, we found that by only varying the final trap depth of the optical tweezer, we can selectively populate the Haldane edge state alone (by using the deep tweezer trap frequency ω_d), or both Haldane- and anomalous edge state (by using the shallow tweezer trap frequency ω_s), as can already be seen in Fig. 4.6. In the following, we will exploit this trap-depth-dependent selectivity by using different settings for populating the edge state in the Haldane- and in the anomalous regime.

The sequence we employ to populate the edge modes of our system is illustrated in Fig. 5.1b: In both cases, we start our sequence by loading atoms from a BEC containing $\sim 2 \times 10^5$ ^{39}K atoms into our optical tweezer. The transfer begins with a quadratic increase of the tweezer potential strength over 40 ms, followed by a constant hold for 170 ms. Within the next 30 ms, we briefly increase the power in the tweezer trap, while the optical dipole trap

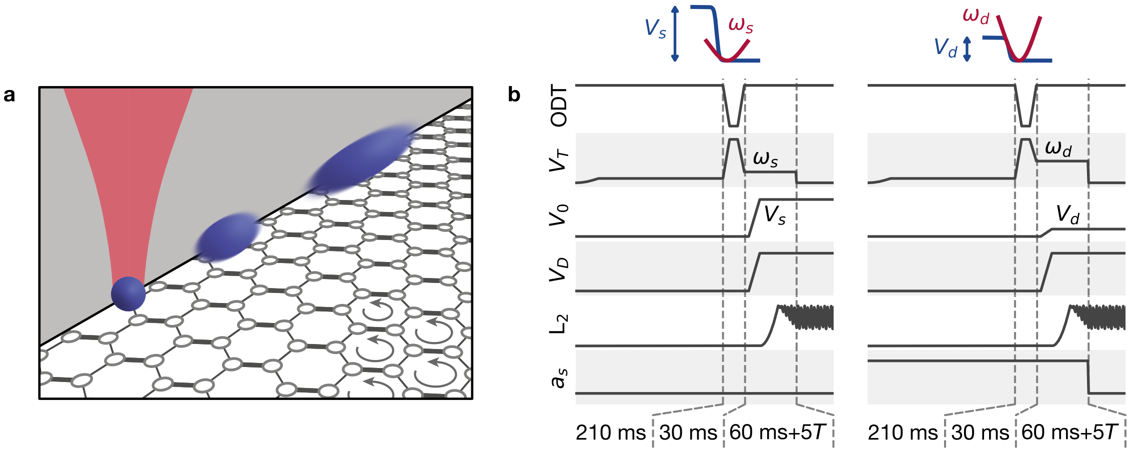

Figure 5.1 | **Edge state population in the presence of disorder. a** Schematic of the population scheme at a topological interface: A tightly-focused optical tweezer (red) confines a BEC (blue), which is released near a repulsive potential step (gray). The atoms subsequently evolve in the tunneling-modulated optical lattice. **b** Experimental sequence used for populating the edge state in the anomalous regime, using the shallow tweezer settings ω_s, V_s (left), as well as in the Haldane regime, using the deep tweezer settings ω_d, V_d (right), schematically illustrated by the sketch on top of the column. ODT denotes the potential of the optical dipole trap, V_T the potential imposed by the optical tweezer, V_0 the hard-wall potential projected by the DMD, $\overline{V}_D$ the average strength of the speckle potential, and a_s the s-wave scattering length set via the Feshbach resonance. The duration of three time intervals is marked at the bottom.

power is reduced. This allows us to expel remaining atoms from the dipole trap, which would otherwise contribute to a background signal.

When preparing the atoms in the shallow tweezer trap, the trap frequency of the optical tweezer is ramped down to $\omega_s/(2\pi) = 1.3(1)\,\mathrm{kHz}$, while when preparing the deep tweezer we ramp it to $\omega_d/(2\pi) = 2.0(1)\,\mathrm{kHz}$.

After this, the additional potentials are subsequently ramped up: First, we ramp up the hard-wall potential V_0 projected by the DMD linearly within $30\,\mathrm{ms}$. Because the edge state velocity is highly dependent on the height of the hard-wall potential [79], we choose a relatively low potential height $V_d/h = 2.8\,\mathrm{kHz}$ for the Haldane regime, and a larger value $V_s/h = 13.2\,\mathrm{kHz}$ in the anomalous regime, maximizing the observable signal. Where applicable, we ramp up the speckle potential $\overline{V}_D$ simultaneously with the hard wall.

After these potentials reached their final value, we exponentially ramp up the optical lattice to a depth of $5.9E_R$ within $30\,\mathrm{ms}$. Subsequently, we linearly ramp up the modulation of the lattice potentials within five modulation cycles, and afterwards release the atoms by abruptly switching off the tweezer.

We found that increasing the scattering length during the loading of atoms into the deep tweezer significantly increases the atom number trapped, and thus improves the signal strength for the edge state, as illustrated in Fig. 5.2. Here, we compare the edge state

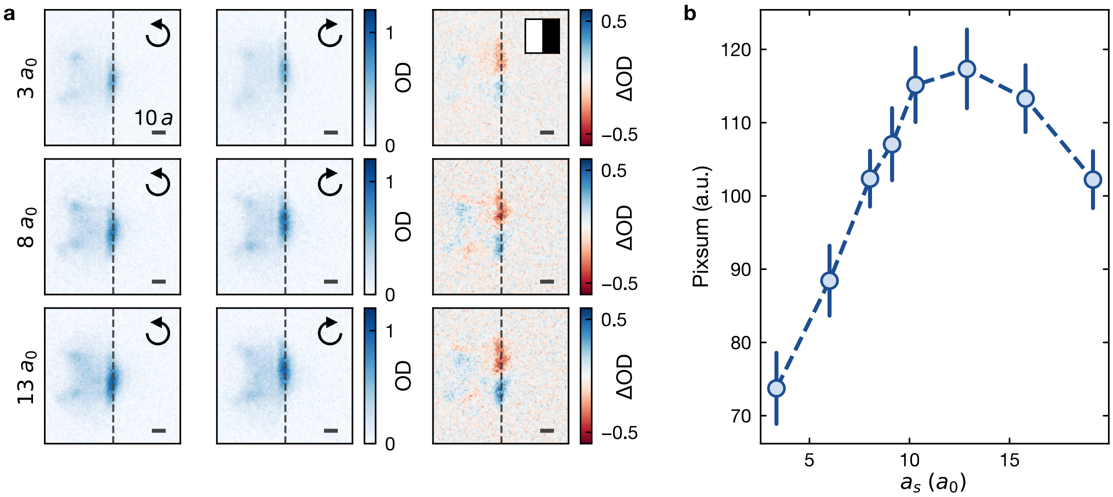

Figure 5.2 | **Effect of increasing the Feshbach field during loading.** **a** Averaged absorption pictures (26-27 averages each) of the edge state in the Haldane regime ($\omega/(2\pi) = 16$ kHz, $m = 0.25$) after 3 ms evolution time. Each line shows the absorption pictures for $\kappa = 1$ (left) and $\kappa = -1$ (center), as indicated by the arrows in the top right corner, and their difference ΔOD on the right. From top to bottom the scattering length is increased, with the scattering length being set to $6a_0$ 5 ms before releasing the atoms from the tweezer for this measurement. The dashed line indicates the location of the topological intercafe. The inset in the top right corner of the difference picture for $a_s = 3a_0$ shows the mask projected by the DMD, with dark areas in the mask marking regions of higher potential energy. The scale bars have length $10a = 2.87$ µm. **b** Pixsum of the absolute value of the edge state difference signal $|\Delta\text{OD}|$ plotted against the scattering length.

signal obtained after an evolution time of 3 ms at an amplitude modulation frequency of $\omega/(2\pi) = 16$ kHz for different magnetic field strengths, tuning the s-wave scattering length between $a_s = 3a_0$ and $a_s = 18a_0$. For this, a BEC was prepared at the chosen scattering length, and loaded into the optical tweezer. To ensure that interaction effects do not impact the propagation of the edge mode, the scattering length was ramped down to a value of $6a_0$ 1 ms before releasing the atoms from the tweezer. We independently ensured by measurements of the Feshbach coil current, that this time is sufficient for the magnetic field to settle befor the atoms are released from the tweezer.

By integrating the absolute difference signal $|\Delta\text{OD}|$ in a region close to the projected edge, we find that the signal is maximized if the scattering length is held at a value $a_s = 13a_0$ while the atoms are in the tweezer. We attribute this to a suppression of loss mechanisms present in the deep tweezer due to the decrease in atomic density. When comparing the number of atoms near the projected edge to the number of atoms scattering into the bulk, it becomes apparent that the increased scattering length does not significantly alter the overlap with the Haldane edge mode or its propagation, supporting that this primarly increases the overall atom number in the tweezer.

In contrast to this, for measurements using the shallow tweezer with a trap frequency ω_s, the BEC is already prepared at $a_s = 6a_0$, and held constant at this value for the remainder of the measurement.

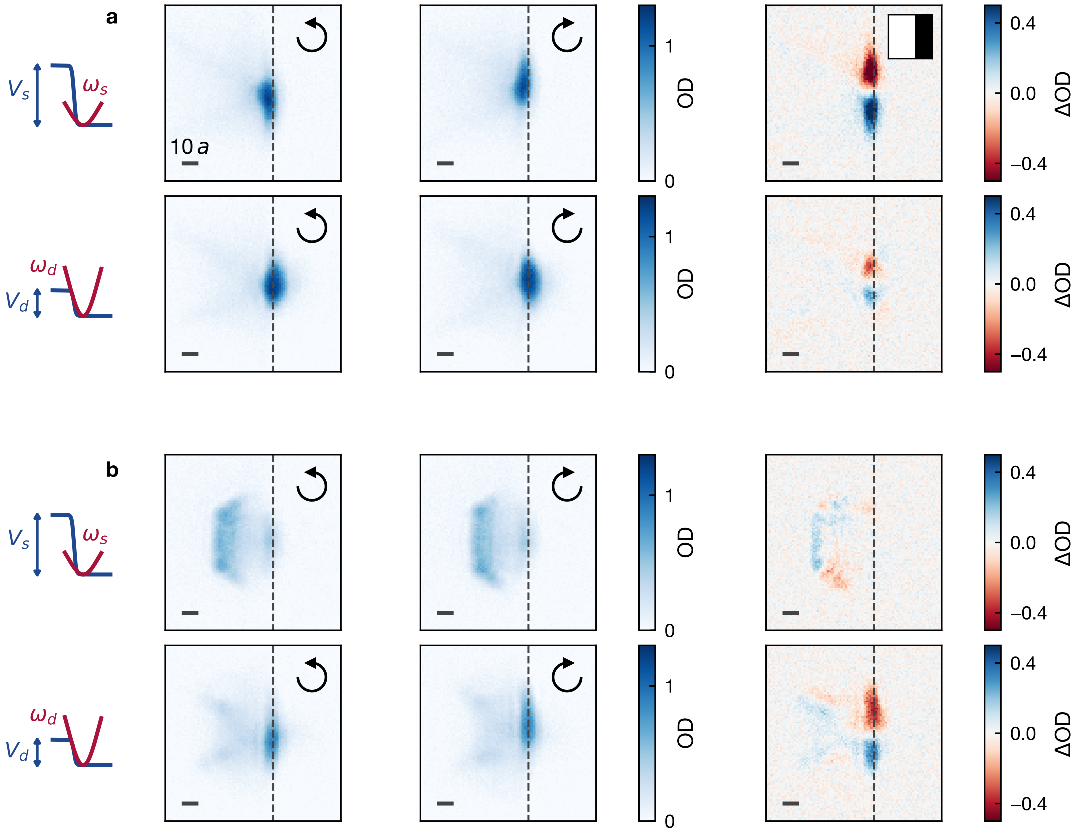

Figure 5.3 | Detecting the topological regime using edge states. The edge state in the anomalous- and Haldane regime is populated using both the narrow- and the deep tweezer settings, with absorption pictures being taken after 50 modulation cycles. **a** shows data taken deep in the anomalous regime at $\omega/(2\pi) = 7\,\text{kHz}$, while **b** shows data deep in the Haldane regime, at $\omega/(2\pi) = 16\,\text{kHz}$. The top row in both subfigures shows data taken with the shallow tweezer settings (ω_s, V_s), while the lower row shows data taken with the deep tweezer settings (ω_d, V_d), as is also illustrated by the sketch to the left of the absorption pictures. Shown is, from left to right, averaged absorption pictures (100 averages each) for modulation chirality $\kappa = 1$, for $\kappa = -1$, and their difference, $\text{OD}_{\text{diff}} = \text{OD}_{\kappa=1} - \text{OD}_{\kappa=-1}$. The arrows in the top right corner illustrate the modulation chirality. The dashed line marks the location of the potential step. The potential step is also illustrated in the inset in the top right corner of the uppermost difference picture, with dark regions corresponding to regions with higher potential energy in the atomic plane. All scale bars have a length of $10a \approx 2.87\,\mu\text{m}$.

The obtained edge state propagation is shown in Fig. 5.3: If the shallow tweezer settings (ω_s, V_s) are used to populate the edge state deep in the anomalous regime at a modulation frequency $\omega/(2\pi) = 7\,\text{kHz}$, one observes strong chiral motion, with most atoms populating the edge mode, and only few leaking into the bulk. This is is further highlighted by a strong chiral signal, as can be seen in the corresponding difference picture. If the deep tweezer settings (ω_d, V_d) are used to populate the edge state at the same modulation parameters, one observes a slightly smaller, albeit still large atom number near the edge, with again only few atoms leaking into the bulk. A chiral signal is clearly visible, although the transport velocity appears to be smaller, leading to an overall weaker signal in the difference picture.

Deep in the Haldane regime, at a modulation frequency $\omega/(2\pi) = 16\,\mathrm{kHz}$, the edge state behaves quite differently: If the shallow tweezer settings are used to place atoms close to the potential step, most atoms scatter into the bulk of the system, with a few atoms staying close to the wall. In the difference picture, no chiral movement can however be observed for these atoms, not even for data taken after a longer evolution time. When using the deep tweezer settings, most atoms remain close to the potential step, with few atoms leaking into the bulk. The atoms at the edge of the system again populate the edge state of the system, undergoing chiral movement, as can be seen in the difference picture.

5.1.1 Alignment of the tweezer position with respect to the potential step

The overlap between the edge mode of the system and the wavepacket placed by the optical tweezer is highly dependent on the alignment of the tweezer position with respect to the potential step. Wehen taking data in disordered systems, taking data at multiple locations would have however compromised our ability to perform disorder averaging: Either a reduction of the number of disorder realizations averaged for each parameter combination, or a reduction of the resolution of parameter scans would have been necessary to take all data for one data set in a single experimental run, consisting of a few thousand measurements with a cycle time of $33\,\mathrm{s}$ inbetween.

Instead, we decided to align the tweezer to the hard wall potential for both tweezer settings before starting measurements: For the deep tweezer settings (ω_d, V_d), we placed atoms close to the potential step deep in the Haldane regime, at a modulation frequency $\omega/(2\pi) = 16\,\mathrm{kHz}$, alternating the chirality of the lattice modulation, and taking absorption pictures after an evolution time of $50T$. Analogously, for the shallow tweezer settings (ω_s, V_s) we performed the same measurement deep in the anomalous regime, at $\omega/(2\pi) = 7\,\mathrm{kHz}$. The strength of the edge state signal was evaluated as the integrated optical density of $|\mathrm{OD}_{\mathrm{diff}}|$ in a region close to the potential step, and the tweezer position with respect to the wall was optimized to maximize this signal.

To ensure that this alignment procedure does not introduce systematic bias into the data taken, we also performed measurements with a coarser parameter sampling and fewer disorder averages at multiple tweezer positions simultaneously. These measurements confirm that the qualitative behavior observed in this chapter remains consistent across different tweezer positions, with two such measurements presented in App. A.

5.1.2 Determining the edge state position

In order to investigate the effect disorder has on the propagation of the edge modes of our systems, it is essential to extract information about their location. For this, we determine the center of mass position $\bar{y}$ along the topological boundary, which we extract from the absorption pictures via a weighted average:

$$\bar{y} = \frac{\sum_i y_i w_i}{\sum_i w_i}, \tag{5.1}$$

with y_i being the corresponding position along the topological boundary of each camera pixel in the atomic plane, and the weight w_i being the optical density at this position. The optical density is determined taking saturation effects for large imaging intensities into account [209, 210] (cf. Sec. 3.4.2). The region evaluated for this calculation was chosen such, that all atoms populating the edge state are captured for all disorder strengths applied, while atoms leaking into the bulk are neglected. To ensure that no systematic bias was introduced by the concrete choice of a region, we ensured that $\bar{y}$ is insensitive to small variations in the size of the region of interest.

Because this signal itself is susceptible to systematic shifts of the initial position and gradients in the system, we evaluate the difference between the center of mass obtained for the two modualtion chiralities, $\bar{y}_{\kappa=1}$ and $\bar{y}_{\kappa=-1}$:

$$\begin{aligned}\Delta\bar{y} &= \bar{y}_{\kappa=1} - \bar{y}_{\kappa=-1} \\ &= \frac{\sum_i y_i w_{i,+1}}{\sum_i w_{i,+1}} - \frac{\sum_i y_i w_{i,-1}}{\sum_i w_{i,-1}}.\end{aligned} \tag{5.2}$$

As typically several images are taken for each parameter combination, this allows us to quantify the uncertainty in $\Delta\bar{y}$, via a bootstrap resampling method: For a given set of experimental parameters, we acquire N absorption pictures, with N typically being in the range from 19 to 40, depending on the measurement. Each of this absorption pictures has been taken for a different disorder realization, with data for different chiralities but otherwise identical parameters being taken in succession, using the same disorder realization.

We now randomly select N_{boot} sets of absorption pictures, each having length N, allowing individual pictures to appear mutliple times in a given bootstrap set. For each set i, we then calculate the center of mass distance $\Delta\bar{y}_i$. Now, one can estimate the statistical error $\sigma_{\Delta\bar{y}}$ on the center of mass distance $\Delta\bar{y}$ by calculating the standard deviation of the distribution obtained this way,

$$\sigma_{\Delta\bar{y}} = \sqrt{\frac{1}{N_{\text{boot}}} \sum_{i=1}^{N_{\text{boot}}} (\Delta\bar{y}_i - \Delta\bar{y})^2}. \tag{5.3}$$

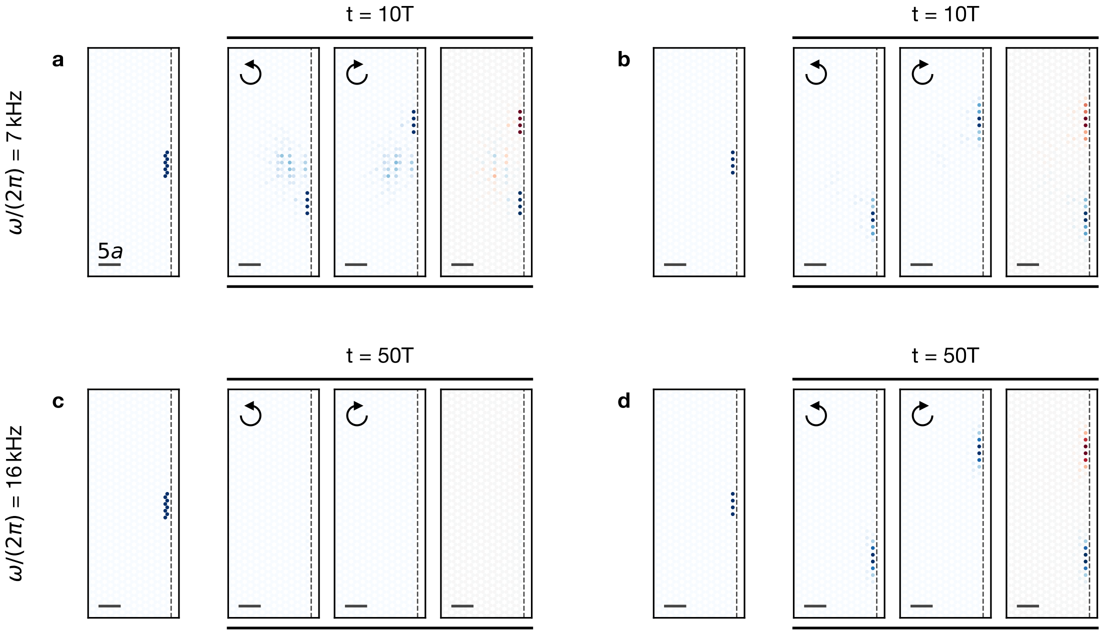

Figure 5.4 | Different preparation protocols for the numerical edge state. The edge state is prepared on the lattice sites at the numerical edge of the system, and evolves in the anomalous (**a**, **b**) and Haldane regime (**c**, **d**). The lattice site population of the initially prepared state is shown on the left of each subfigure, and to the right the evolved system for both chiralities as well as their difference picture. **a** and **c** show the evolution for a system, where the lattice sites at the numerical edge were populated in a zig-zag pattern with constant phase, and **b** as well as **d** for a system, where only the lattice sites closest to the edge were populated with alternating phases. The evolution time is $t = 10T$ in the anomalous, and $t = 50T$ in the Haldane regime. The arrows in the top left corner of the plot denote the chirality of the tunneling modulation. The colormap for the initial states is normalized to the peak lattice site population, and in the evolved systems to half that value. Lattice sites close to the initial preparation position are shown, with removed sites in the lattice having no significant population. All scale bars have length $5a$.

5.1.3 Numerical preparation protocol

To benchmark our experimental results in this chapter, we often times numerically investigate the evolution of a wavepacket close to the numerical edge of a tunneling-modulated lattice. Here, we follow the modulation scheme introduced in Sec. 2.3, only considering nearest neighbor tunneling, as next nearest neighbor tunneling amplitudes are about an order of magnitude smaller. The continuous modulation of the tunneling in the lattice is approximated by discretizing the modulation into 21 steps in the simulations. Where applicable, disorder is sampled from a numerically generated speckle pattern, having the same correlation length $\sigma_r = 296\,\mathrm{nm}$ as the experimentally realized speckle pattern (cf. Sec. 3.2.4).

In Fig. 5.4, we investigate the population of the numerical edge mode of the system, in analogy to Fig. 5.3. The system we study consists of 3806 lattice sites and an side-length-ratio of ≈ 2.8, with the long side being the zig-zag edge, where we populate the edge state. Shown is only the central part of the system around to the location where the initial state is situated, the system is a factor two larger in both directions. The duration of the evolution was adjusted for different modulation frequencies for illustrative purposes, similar behavior can be observed for different evolution times.

We test two different preparation protocols for the numerical edge state: In the first, we populate 8 lattice sites along the zig-zag edge of the system, each with the same phase and amplitude. When populating the edge mode deep in the anomalous regime, at $\omega/(2\pi) = 7\,\mathrm{kHz}$, as shown in Fig. 5.4a, we observe a clear chiral signal, with few atoms populating bulk states. Repeating the same preparation protocol deep in the Haldane regime, at $\omega/(2\pi) = 16\,\mathrm{kHz}$, displayed in Fig. 5.4c, it is immediately clear that this approach is not successful, with the population rapidly spreading out and populating bulk states, and no chiral signal discernible.

Studying the dispersion in the anomalous and in the Haldane regime – for instance illustrated in Fig. 2.3 – it is clear, why this approach is not successful: The prepared state has a constant phase across all lattice sites, and is therefore at zero quasimomentum. While the edge state in the π-gap in the anomalous regime is situated at zero quasimomentum, this edge state is absent in the Haldane regime. To taylor a state which has an overlap with the edge state in the 0-gap of the system, we populate four lattice sizes directly at the numerical edge, alternating the phase on the lattice sites between 0 and π.

When preparing the edge state in the anomalous regime using this protocol, shown in Fig. 5.4b, we again observe an edge state, this time with no significant fraction of atoms scattering into the bulk. As we will see later however, this time not the edge state in the π-gap of the system has been populated, but the edge state in the 0-gap. This is the reason why this preparation protocol also functions deep in the anomalous regime, allowing us to numerically study the edge state propagation in both regimes, shown in Fig. 5.4d.

A more systematic approach for investigating these preparation protocols is illustrated in Fig. 5.5. Here, the overlap of the states prepared with the eigenstates of the system at modulation frequencies of $\omega/(2\pi) = 7\,\mathrm{kHz}$, $\omega/(2\pi) = 10\,\mathrm{kHz}$, and $\omega/(2\pi) = 16\,\mathrm{kHz}$ shown.

For the first preparation protocol, populating 8 lattice sites with equal phase, one can see that deep in the anomalous regime, there is a strong overlap with the initial state in the π-gap, where the edge state is located. For the other edge state in the 0-gap however, no overlap is visible. Upon increasing the modulation frequency and approaching the phase transition into the Haldane regime, located near $\omega/(2\pi) = 10.5\,\mathrm{kHz}$ in the two-band model simulated, the π-gap shrinks. This leads to some overlap of the initial state with bulk states, while still having good overlap with the edge mode in the π-gap. Deep in the Haldane regime however, the edge state in the $\pi - gap$ has vanished, so that the initial state only couples to bulk states of the system, still not having any overlap with the edge mode in the 0-gap.

For the second preparation protocol however, where four lattice sites are populated with alernating phases, the initial state has for all modulation frequencies investigated good overlap with the edge states in the 0-gap of the system, and no significant overlap with any other states.

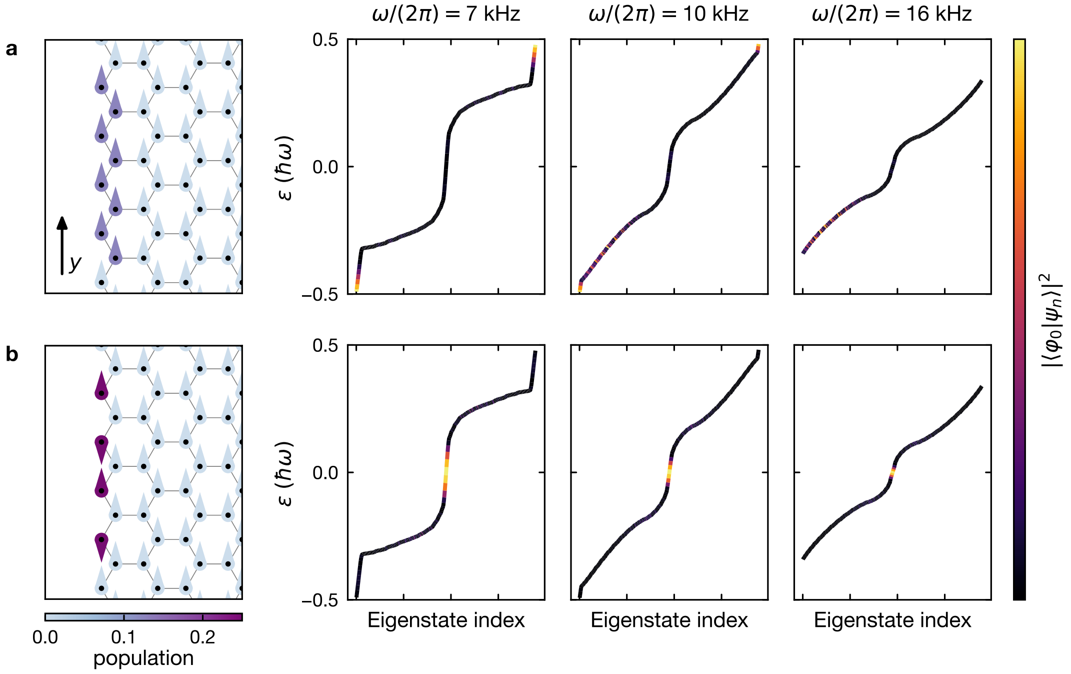

Figure 5.5 | Eigenstate overlap for the different preparation protocols. **a** investigates the preparation protocol, where 8 lattice sites along the zig-zag edge are populated with equal phase, while **b** studies the preparation protocol where only the lattice sites directly at the numerical edge are populated with opposite phase. On the left of each subfigure, the initial state is illustrated, with the hue of each of the arrows connected to the lattice sites encoding the lattice site population, and the direction the arrow is facing encoding the phase. To the right of that, the overlap of this state with the eigenstates of the system, sorted by energy, at modulation frequencies $\omega/(2\pi) = 7$ kHz, $\omega/(2\pi) = 10$ kHz, and $\omega/(2\pi) = 16$ kHz is illustrated.

This different overlap of the two initial states allows us to also distinguish the two regimes numerically, by observing the propagation of the states prepared with these two methods.

5.2 Propagation of edge states in the presence of disorder

We start our investigation by studying the effect disorder has on the propagation of the edge modes on our platform. For this, we focus on the Haldane regime, as the paradigmatic example of a Chern insulator. We take data deep in the Haldane regime at $\omega/(2\pi) = 16\,\mathrm{kHz}$, and utilize the deep tweezer settings (ω_d, V_d) to populate the edge mode, as discussed in Sec. 5.1. The tunneling modulation frequency was chosen such that we are sufficiently far in the Haldane regime, away from the phase transition to the anomalous regime. Simultaneously, the 0-gap remains reasonably large at this frequency, resulting in a large group velocity of the edge mode.

In Fig. 5.6a we investigate the propagation of the Haldane edge mode in a clean system with no disorder applied. In the single-chirality pictures one can clearly see the atoms propagate along the potential step, performing chiral movement. Even though a fraction of the atoms leaks into the bulk of the system, most atoms stay close to the topological interface. This chiral movement becomes even more apparent in the difference pictures, where the non-chiral bulk propagation is cancelled out. For propagation times longer than $80T$ a drop in atom number in the edge mode becomes apparent. This atom loss occurs at the same time scale as the life time of the edge mode, determined for the same modulation parameters in [79].

If we introduce disorder into the system, as illustrated in Fig. 5.6b for $\overline{V}_D/h = 0.92\,\mathrm{kHz}$, the edge mode dynamics are fundamentally altered: Instead of propagating in a straight line along the potential step, the atoms now propagate towards the bulk of the system, and the overall transport velocity along the edge appears to be significantly reduced. Because of this, it is much harder to make out any chiral movement in the single-chirality pictures, and one has to rely on the difference picture instead.

To more systematically investigate the effect disorder has on the propagation of the edge states, we extract the center-of-mass distance $\Delta\bar{y}$ from the experimental data, shown in Fig. 5.7a. Here, the evolution of the edge mode was studied for $\overline{V}_D/h = [0\,\mathrm{kHz}, 0.46\,\mathrm{kHz}, 0.92\,\mathrm{kHz}, 1.39\,\mathrm{kHz}]$, limiting the evolution times up to $t = 80T$ due to the atom loss at longer times. From this, it is apparent how the introduction of disorder leads to a reduction of transport velocity in the edge mode. In the limit of weak disorder, this can be understood in terms of disorder introducing couplings between different quasimomenta in the dispersion, leading to a renormalization of the edge mode velocity [235].

We additionally simulate the propagation of the edge mode at $\omega/(2\pi) = 16\,\mathrm{kHz}$ in a two-band tight-binding model to support our experimental findings, as described in Sec. 5.1.3. We let the system evolve, and extract the center of mass position following the same routine as established for the experimental measurements (cf. Sec. 5.1.2). We additionally apply disorder to the system via numerically generated speckle potentials, having the same potential strengths and correlation length as experimentally realized. Here, we observe qualitatively similar behavior as in the experimental data: Increasing disorder leads to a reduction of the propagation velocity.

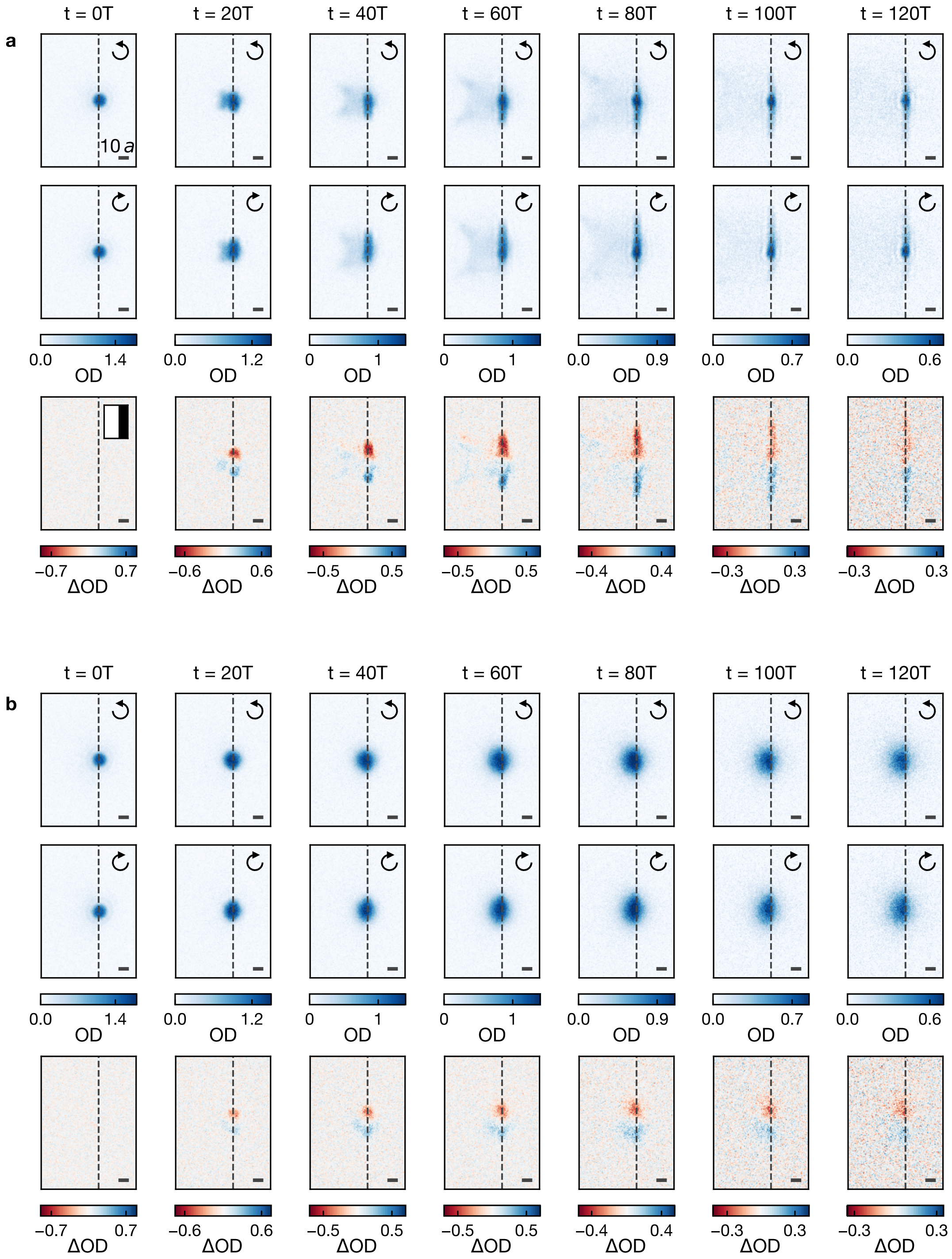

Figure 5.6 | Effect of disorder on Haldane edge mode propagation. Averaged absorption pictures (39-40 averages each) of the edge state deep in the Haldane regime ($\omega/(2\pi) = 16\,\mathrm{kHz}$) for different evolution times. **a** shows the results obtained for a clean system (at disorder strength $\overline{V}_D = 0$), while **b** shows the results obtained for $\overline{V}_D/h = 0.92\,\mathrm{kHz}$. The top line of each subfigure displays the absorption pictures obtained for chirality $\kappa = 1$, while the line in the middle shows the results for $\kappa = -1$, as indicated by the arrows in the top right corner of the absorption images. Their difference ΔOD is shown in the bottom line. The scale bar in the bottom right corner of each plot has length $10a$. The dashed line illustrates the location of the potential step. The inset in the top right corner of the difference picture for $t = 0T$ and $\overline{V}_D = 0$ shows the mask displayed on the DMD, with black regions corresponding to regions of higher potential energy in the atomic plane.

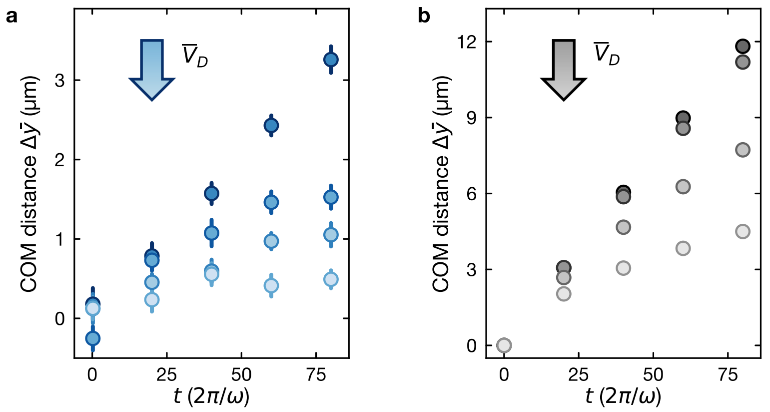

Figure 5.7 | Propagation in the disordered Haldane system. Center of mass distance $\Delta\bar{y}$ for varying evolution times t and for varying disorder strengths $\overline{V}_D$ in the Haldane regime ($\omega/(2\pi) = 16$ kHz). **a** shows experimental data, while **b** shows numerical simulations for the edge state propagation. The disorder is encoded in the color of the data points, with $\overline{V}_D/h = [0\,\text{kHz}, 0.46\,\text{kHz}, 0.92\,\text{kHz}, 1.39\,\text{kHz}]$ for both data sets. For the experimental results, each data point is averaged over 39-40 disorder realizations, while the numerical data is averaged over 100 disorder realizations. The error bars of the data points are extracted via bootstrapping.

In comparison to the experimental data however, significantly larger distances are traversed by the edge mode. We attribute this to the finite width of the experimentally realized potential step, which reduces the transport velocity due to hybridization of the edge mode with bulk states [154–156].

5.3 Probing phase transitions in Floquet driven systems

While multiple methods exist for probing the geometric properties of optical lattice systems, they almost exclusively make use of the translational invariance of the underlying lattice [59, 60, 68, 70–72, 117]. This prevents the application of these techniques to disordered systems, where the translational symmetry is broken.

Edge modes, which are directly related to the topological properties of the system via the bulk-boundary connection, do however not rely on the translational symmetry of the system, and thus also can be used as a marker for the topological properties of a system in the presence of disorder. In the following, we will introduce the edge states of our system as a tool for determining the location of the phase transition, allowing us to determine the location of the phase transition in the presence of disorder, and enabling us to observe a disorder-driven phase transition between two distinct topological regimes. While disorder-driven phase transitions have already been observed on multiple platforms in the context of topological Anderson insulators [74–78], this is to our knowledge the first experimental observation of a disorder-driven phase transition between two topologically nontrivial regimes.

5.3.1 Probing a phase transition using gap-closing measurements

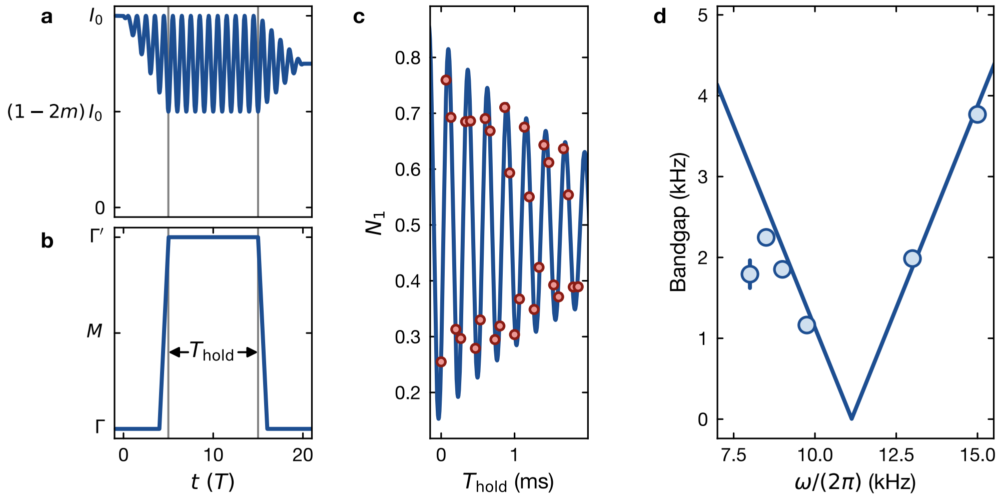

Figure 5.8 | Determining the location of a phase transition using gap closing measurements. a Intensity modulation of the lattice beams during a gap closing measurement in the modulated lattice: The modulation amplitude is ramped up in $5T$. Afterwards, the modulation amplitude is kept constant for an integer number of modulation cycles. Subsequently, the modulation amplitude is again ramped down in $5T$, now settling on an intensity $(1-m)I_0$. **b** Quasi momentum of the atoms loaded in the lattice during the gap closing measurement: Initially at $\mathbf{k}=\Gamma$, the atoms are then accelerated to $\mathbf{k}=\Gamma'$ of the adjacent Brillouin zone nonadiabatically, such that the atoms arrive at Γ' at the same time the amplitude modulation is fully ramped up. The atoms are now held at Γ' for T_{hold}, and subsequently accelerated back to the Γ-point of the initial Brillouin zone. **c** Oscillations observed in the population of the first band when varying the hold duration T_{hold}. The data was taken at a lattice amplitude modulation frequency $\omega/(2\pi)=15$ kHz. The solid line is a fit described by Eq. 5.4 used to extract the bandgap. **d** Measured energy gap at different modulation frequencies. The solid line is a fit of form $|\omega-\omega_c|$. Error bars are the fit error from fitting the bandgap.

In the absence of disorder, multiple established methods for determining the location of a topological phase transition exist. One such method employs bandgap measurements using Stückelberg interferometry, (cf. Sec. 3.3.2): The experimental sequence starts with a weakly interacting BEC at $6a_0$ at $\mathbf{k}=\Gamma$ in the lowest band of the unmodulated lattice. To adiabatically transfer the system into the ground state of the modulated lattice, the modulation is ramped up linearly within $5T$.

In the following, we apply a strong force to drive the atoms to $\mathbf{k}=\Gamma'$ in the neigbouring Brillouin zone. Performing this acceleration nonadiabatically coherently transfers population from the lower band into the upper band. As discussed in Sec. 3.3.2, the atoms in the two bands acquire a differential phase $\phi_t=(\omega_{\mathrm{upper}}-\omega_{\mathrm{lower}})/(2\pi)\cdot T_{\mathrm{hold}}$ during the hold time at Γ', where $E_{\mathrm{upper}}=\hbar\cdot\omega_{\mathrm{upper}}$ is the energy of the upper band, $E_{\mathrm{lower}}=\hbar\cdot\omega_{\mathrm{lower}}$ is the energy of the lower band, and T_{hold} is the hold duration.

Now, a rampdown of the amplitude modulation within $5T$ with $(1-m)I_0$ as a final intensity is started. Simultaneously, we transfer the atoms back to the initial quasimomentum $\mathbf{k}=\Gamma$

nonadiabatically, again coupling the population of the two bands coherently. Due to the differential phase acquired, this leads to different populations in the first and the second band, which can be extracted via a bandmapping measurement [187]. For this, the lattice potential is ramped down adiabatically, such that the population in the different bands can be obtained after a time-of-flight measurement.

By varying the hold duration T_{hold}, one can now oberserve oscillations in the bandpopulation with frequency $\omega_{\text{gap}} = (E_{\text{upper}} - E_{\text{lower}})/\hbar$, illustrated in Fig. 5.8c. We extract the size of the gap by fitting a damped cosing function to the population remaining in the first band:

$$N_1(t) = N_0 + A \exp\left(\frac{t - t_0}{\tau}\right) \cos\left(\omega_{\text{gap}}(t - t_0)\right) \tag{5.4}$$

To determine at which modulation frequency the transition from anomalous- to Haldane-regime occurs, we measure the energy gap Γ at different modulation frequencies on both sides of the transition, and fit a function of form

$$\omega_{\text{gap}} = |\omega - \omega_c|, \tag{5.5}$$

as depicted in Fig. 5.8d. This way, we obtain a transition frequency between the anomalous- and the Haldane regime of $\omega_c/(2\pi) = 11.13(8)\,\text{kHz}$, where the error of the measurement is estimated to be the fit error. This is in agreement with numerical simulations of a six-band model, which predicts the transition between the two regimes to occur at $\omega_{c,\text{6-band}}/(2\pi) = 10.92\,\text{kHz}$.

5.3.2 Probing a phase transition using edge states

In Sec. 5.1 we already discussed how different preparation protocols for the edge state can be employed as a marker to determine whether our system is in the anomalous- or in the Haldane-regime. In the following, we will establish how they can also be used to measure the concrete location in the phase diagram, at which the transition between the two regimes occurs.

Here, we make use of the shallow tweezer settings ($\omega_s = 1.3(1)\,\text{kHz}$, $V_s/h = 13.2\,\text{kHz}$), while scanning the amplitude modulation frequency ω of the optical lattice.

In Fig. 5.9a, averaged absorption pictures after an evolution time of $50T$ are shown together with their difference pictures for several lattice amplitude modulation frequencies. At $\omega/(2\pi) = 7\,\text{kHz}$, deep in the anomalous regime and far away from the phase transition to the Haldane regime, most atoms placed near the potential step by the optical tweezer populate the edge state, and contribute to a differential signal. By increasing the modulation frequency, one approaches the phase transition, and more atoms end up populating bulk states, while the transport velocity of the atoms populating the edge state simultaneously decreases, as visible in the data taken at $\omega/(2\pi) = 9\,\text{kHz}$. At an even larger modulation frequency of $11\,\text{kHz}$, almost all atoms from the tweezer populate states in the bulk of the system, and the atoms remaining near the edge do not exhibit observable chiral motion any more.

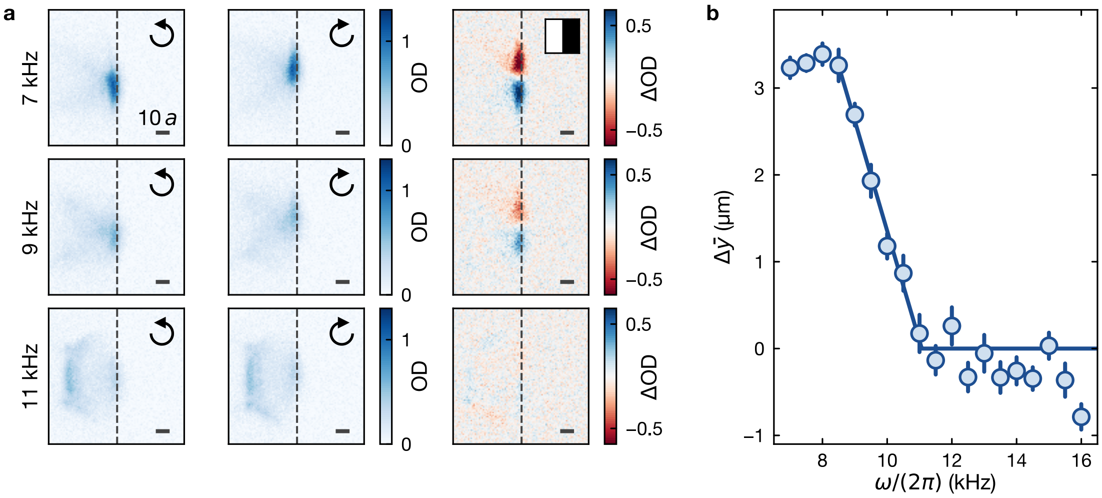

Figure 5.9 | Determining the anomalous-Haldane phase transition using edge states. **a** Averaged absorption pictures obtained after 50 modulation cycles for $\omega/(2\pi) = [7\,\text{kHz}, 9\,\text{kHz}, 11\,\text{kHz}]$, each taken after $t = 50T$. From left to right: $\kappa = 1$, $\kappa = -1$, and the difference picture $\Delta\text{OD} = \text{OD}_{\kappa=1} - \text{OD}_{\kappa=-1}$. Every image is the average of 19-20 experimental realizations. The scale bars correspond to $10a$. The arrow in the top right corner of the single chirality pictures indicates the chirality of the lattice modulation, while the inset in the top right corner of the difference picture for $\omega/(2\pi) = 7$ kHz illustrates the mask displayed on the DMD, with black regions corresponding to regions of higher potential energy in the atomic plane. **b** Center of mass distance $\Delta\bar{y}$ traversed by the edge modes after $50T$. Each data point is the average of 19-20 disorder realizations, with error bars being extracted via bootstrapping. The solid line is a fit of form $\Delta\bar{y} = \max\left(-\eta(\omega - \omega_c), 0\right)$ to data points with $\omega/(2\pi) \geq 8.5$ kHz.

To quantitatively evaluate this reduction in transport velocity, we calculate the center of mass distance $\Delta\bar{y}$ for the atoms in the edge state, as shown in Fig. 5.9b. To ensure that atoms in the bulk of the system do not influence the determined center of mass, the size of the evaluation region was slightly varied, and no significant change in the determined center-of-mass location was observed.

The extracted center-of-mass distances demonstrate that the edge state velocity initially remains constant, but undergoes a progressive reduction at higher modulation frequencies, ultimately leading to complete suppression of transport. By fitting a function of form

$$\Delta\bar{y}\,(\omega) = \max\left(-\eta(\omega - \omega_c), 0\right) \tag{5.6}$$

to data points with $\omega/(2\pi) \geq 8.5\,\text{kHz}$, we extract the transition frequency $\omega_c/(2\pi) = 11.1(2)\,\text{kHz}$ as the point where the transport vanishes. This result is in excellent agreement with the transition frequency obtained by gap-closing measurements in Sec. 5.3.1 as $\omega_{c,\text{gap}}/(2\pi) = 11.13(8)\,\text{kHz}$, as well as the numerical result obtained via a six-band model, $\omega_{c,\text{6-band}}/(2\pi) = 10.92\,\text{kHz}$.

5.3.3 Tracking the phase transition for nonzero disorder

In the previous section, we have established the propagation of the edge state prepared using the shallow tweezer settings (ω_s, V_s) as a probe for the topological regime. While bulk measurements of the topological invariants fail in the presence of disorder, the existence of edge modes is directly connected to the topological properties of the system via the bulk-boundary correspondence. In the following, we will utilize this to to explore the phase diagram of our system in the presence of disorder.

In Fig. 5.10 we investigate the feasability of determining the location of the phase transition using the topological edge states of the system at nonzero disorder. For this, we probe the system at two disorder strengths, $\overline{V}_{D,1} = 0.23\,\text{kHz}$, and $\overline{V}_{D,2} = 0.46\,\text{kHz}$. We probe the system at 8 modulation frequencies of the optical lattice, displayed in blue, choosing the modulation frequency such that data is taken both in the anomalous- as well as in the Haldane regime.

When observing the center of mass distance $\Delta\bar{y}$ for these disorder strengths, the qualitative behavior remains identical to that of the clean system: At low modulation frequencies, far away from the phase transition into the Haldane regime, one observes clear chiral transport. As the modulation frequency is increased however, approaching the transition

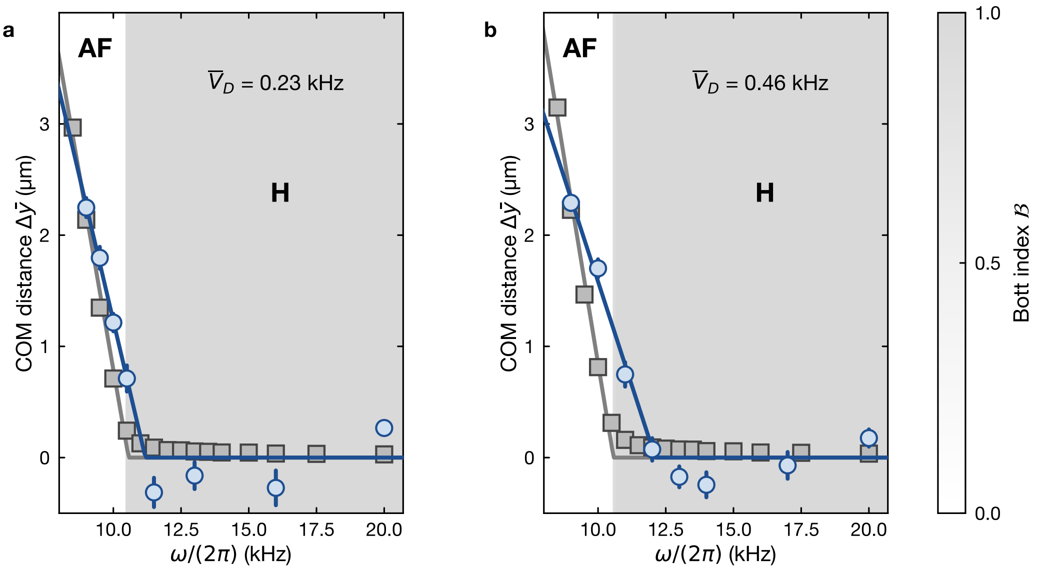

Figure 5.10 | Probing the anomalous-Haldane phase transition in the presence of disorder. Center-of-mass distance $\Delta\bar{y}$ observed after $50T$ for varying modulation frequencies at **a** $\overline{V}_D/h = 0.23\,\text{kHz}$ and **b** $\overline{V}_D/h = 0.46\,\text{kHz}$. The blue data points mark the experimentally measured center of mass distances $\Delta\bar{y}$. The grey squares represent the center of mass distance observed in a numerical simulation after $20T$. The experimental data is averaged over 19-20 measurements per chirality, while the numerical data is averaged over 100 disorder realizations. For both, error bars have been determined via bootstrapping. The solid lines are fits of the form $\Delta\bar{y}\,(\omega) = \max\left(-\eta(\omega-\omega_c), 0\right)$. The grey shading in the background encodes the Bott index $\mathcal{B}$, evaluated for 100 disorder realizations on $N_s = 576$ lattice sites. The labels (AF) and (H) indicate the anomalous ($\mathcal{B} = 0$) and Haldane regime ($\mathcal{B} = 1$) respectively.

between the two regimes, the edge transport weakens and the signal diminishes, eventually entirely vanishing as the system enters the Haldane regime. When comparing the results obtained one notices, that the transition to the Haldane regime appears to occur at a larger modulation frequency for the measurement performed at $\overline{V}_{D,2}$ compared to the measurement at $\overline{V}_{D,1}$. To investigate this systematically, we again perform a fit using Eq. 5.6 in order to extract the transition frequency. This fit yields $\omega_c(\overline{V}_{D,1})/(2\pi) = 11.18(31)\,\mathrm{kHz}$, and $\omega_c(\overline{V}_{D,2})/(2\pi) = 12.11(20)\,\mathrm{kHz}$, supporting the observed shift of the transition frequency. The errors on these transition frequencies were obtained as the fit errors, considering the errors on $\Delta\bar{y}$ obtained via bootstrapping.

As gap-closing measurements already fail at this level of disorder, we instead benchmark the result against numerical simulations. For this, we calculate the Bott index [116, 236] (as introduced in Sec. 2.5.2) in a rectangular system consisting of $N_s = 576$ lattice sites, enforcing periodic boundary conditions. The obtained results are encoded in the grey background shading of Fig. 5.10. The tunneling modulation described in Sec. 2.3 was implemented in a two-band model, discretizing the continuous modulation of the lattice beams into 21 steps. Next-nearest neighbor tunneling, having amplitudes about an order of magnitude smaller, was neglected. We ensured via convergence tests, that this system size is sufficient to accurately describe the topological properties of the system [80]. Similar to the the numerical propagation simulations, disorder has been sampled from a numerically generated speckle pattern with the same correlation length and disorder strength as experimentally realized. We repeated this calculation for different disorder realizations with the same characteristics, averaging the obtained Bott indices over 100 different results. These simulations predict transition frequencies between the two regimes of $\omega_{c,\mathrm{Bott}}(\overline{V}_{D,1}) = 10.51(8)\,\mathrm{kHz}$, as well as $\omega_{c,\mathrm{Bott}}(\overline{V}_{D,2}) = 10.62(9)\,\mathrm{kHz}$, extracted via a logistic fit to the simulated Bott indices.

These transition frequencies are significantly smaller than the transition frequencies obtained experimentally. We attribute this discrepancy to the Bott index only considering a two-band model: Already for a clean system, the Bott index predicts a transition frequency of $\omega_{c,\mathrm{Bott}}(\overline{V}_D/h = 0)/(2\pi) = 10.44\,\mathrm{kHz}$, which is not compatible with the transitition frequency obtained from a six-band model, $\omega_{c,\text{6-band}}(\overline{V}_D/h = 0)/(2\pi) = 10.92\,\mathrm{kHz}$. It is however identical to the Chern number $\mathcal{C}$, calculated independently on the same system in a two-band model. We therefore expect the results obtained from the two-band model to systematically underestimate the transition frequency between the two regimes, as higher-band corrections are not captured. Due to system size constraints, the numerical simulation of models with higher-band corrections is unfortunately not feasible, so that we instead compare our experimental results to the two-band model, keeping the corrections in mind.

To support the results obtained from the Bott index, we also numerically simulate the edge state propagation along the zig-zag edge in a system consisiting of $N_s = 952$ lattice sites, with a side length ratio between propagation direction and the perpendicular direction of $L_y/L_x \approx 2.8$. Here, we use the preparation scheme populating 8 lattice sites along the edge with equal phase, introduced in Sec. 5.1.3. Due to system size constraints, we perform

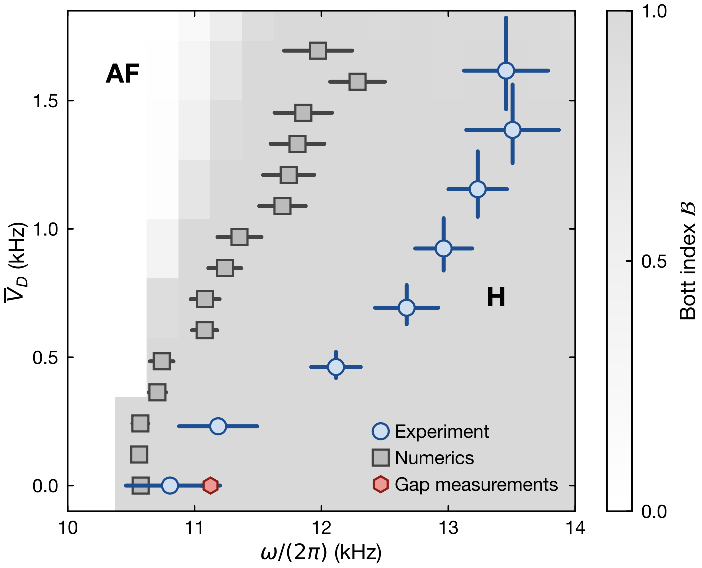

Figure 5.11 | Measurement of the disorder-induced shift of the topological phase transition. Shift of the topological phase transition obtained from experimental measurements (blue) and numerical simulations (gray) extracted by fitting the modulation frequency at which the edge transport $\Delta\bar{y}$ vanishes. The horizontal errorbars are the fit error, taking the uncertainty in determining $\Delta\bar{y}$, extracted via bootstrapping, into account. The vertical error bars on the experimental data reflect the calibration error of the disorder strength. The red data point indicates the gap-closing measurement for $\overline{V}_D/h = 0$ kHz from Sec. 5.3.1. The grey shading in the background encodes the Bott index $\mathcal{B}$, with the labels (AF) and (H) again indicating the anomalous Floquet ($\mathcal{B} = 0$) and the Haldane ($\mathcal{B} = 1$) regime.

the simulation only for $20T$, instead of the experimentally realized $50T$. In analogy to the treatment of the experimental data, we determine the center-of-mass distance between the propagated edge state for both chiralities, extracting an error on the distance via bootstrapping. The center-of-mass distances determined this way are displayed as grey squares in Fig. 5.10. The observed larger propagation distance, given the shorter evolution time, can be attributed to the edge mode propagating along the infinitely sharp numerical edge of the system instead of the finite-width experimentally realized potential step, which leads to a slow-down of the edge mode propagation [154–156]. From these center-of-mass distances, we extract the transition frequency, again using Eq. 5.6. This way, we yield $\omega_{c,\mathrm{num}}(\overline{V}_{D,1})/(2\pi) = 10.56(5)$ kHz, and $\omega_{c,\mathrm{num}}(\overline{V}_{D,2})/(2\pi) = 10.57(6)$ kHz, with the error of the transition frequency being the fit error. These transition frequencies, while also being lower than the experimentally observed transition frequencies, are in excellent agreement with the transition frequencies obtained from the Bott index. With the results obtained from the propagation as well as from the Bott index, both in a two-band model, being in such good agreement, we expect the experimentally observed vanishing point of the edge transport to be a reliable probe for the location of the phase transition.

We now make use of this probe to investigate the location of the phase transition at even larger disorder strengths, shown in Fig. 5.11. Here, the blue data points represent the experimentally measured location at which the edge transport vanishes. Horizontal error bars on these data points are the fit error, taking into account the uncertainty in determining the center-of-mass distance extracted via bootstrapping. The vertical error bars are the uncertainty in the calibration of the disorder potential strength, described in more detail in Sec. 3.2.4. In these results, one can see a rather drastic shift of the transition frequency between the anomalous and the Haldane regime, moving from close to 11 kHz in the clean limit to over 13 kHz for disorders larger than $\overline{V}_D/h = 1\,\mathrm{kHz}$ being applied.

The results of the transition frequency obtained via numerical propagation simulations are displayed as grey data points, with the horizontal error bars representing the fit error of Eq. 5.6, also considering the error on $\Delta\bar{y}$ obtained via bootstrapping. The grey shading in the background encodes the Bott index $\mathcal{B}$, averaged over 100 different disorder realizations for $\overline{V}_D/h < 1\,\mathrm{kHz}$ and averaged over 200 disorder realizations for $\overline{V}_D/h \geq 1\,\mathrm{kHz}$. Here, a shift of the transition frequency to larger values is also observed, although the shift is not as drastic. For disorder strengths larger than $\overline{V}_D/h = 0.5\,\mathrm{kHz}$, the transition frequendy extracted from the numerical propagation appears to diverge slightly towards larger modulation frequencies compared to the results obtained via the Bott index. Altogether, the numerically simulated transition frequencies from a two-band model however predict a lower transition frequency for all disorder strengths compared to the experimental results, which we interpret as the two-band model underestimating the transition frequency also in the presence of disorder. The observed behavior matches the theoretical predictions [109], confirming that disorder indeed favors the anomalous Floquet topological regime over conventional Chern insulators systems.

5.4 Suppression of topological edge transport in the strong disorder regime

After establishing the robustness of topological edge modes to weak and moderate disorder, we now investigate the breakdown of topological protection in the presence of strong disorder. This trivial regime is characterized by the absence of chiral motion, independent of the preparation of the initial state.

We start our investigation by performing measurements deep in the anomalous Floquet phase at $\omega/(2\pi) = 7\,\mathrm{kHz}$, at a disorder strength $\overline{V}_D/h = 11.1\,\mathrm{kHz}$. For this, we place atoms near the potential step using different preparation protocols, and take absorption pictures of the system after an evolution time $t = 50T$. In Fig. 5.12a the system is probed for the shallow tweezer experimental settings ($\omega_s = 1.3(1)\,\mathrm{kHz}$, $V_s/h = 13.2\,\mathrm{kHz}$), optimized for an overlap with the edge mode in the anomalous regime. In the single-chirality pictures, the atoms placed at the topological interface spread out towards the bulk of the system, with no chiral motion discernible when comparing the two chiralities. This is further highlighted by their difference picture, where also no signature of chiral motion can be observed.

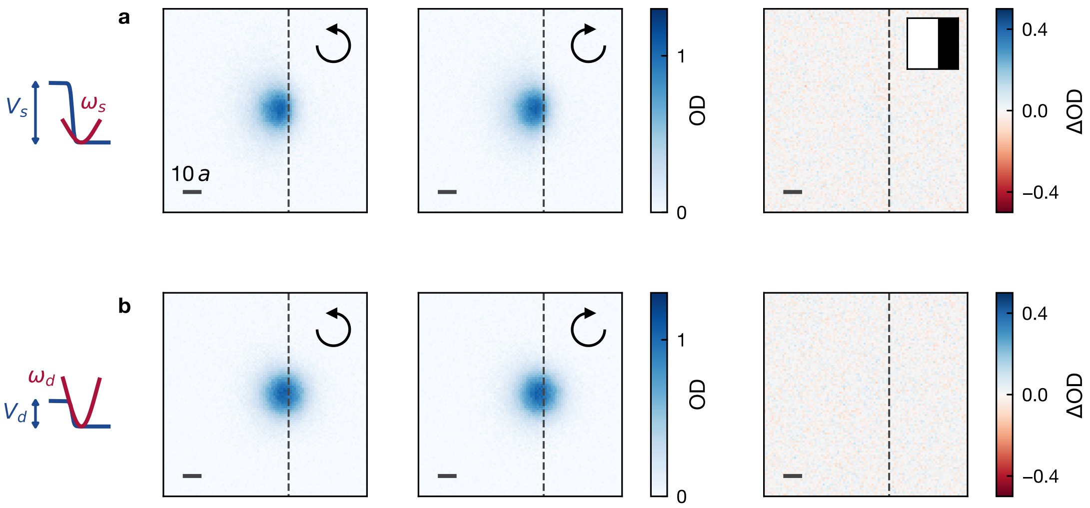

Figure 5.12 | **Suppression of topological edge transport at strong disorder.** Single chirality pictures as well as difference picture obtained after $50T$ when preparing the edge state with the **a** shallow tweezer settings or **b** with the deep tweezer settings at $\omega/(2\pi) = 7$ kHz and $\overline{V}_D/h = 11.1$ kHz. The differences in the tweezer settings are illustrated on the left. The pictures are averaged over 100 different disorder realizations. The dashed line marks the location of the potential step, while the arrows in the upper right corner of the single-chirality plots indicate the chirality of the lattice modulation. The mask displayed on the DMD is illustrated in the inset in the difference picture for the shallow tweezer settings, with black regions corresponding to regions of higher potential energy in the atomic plane.

For the deep tweezer settings($\omega_d = 2.0(1)\,\mathrm{kHz}$, $V_d/h = 2.8\,\mathrm{kHz}$) optimized for populating the edge mode in the Haldane regime, the measurement results are shown in Fig. 5.12b. Here the atoms also propagate into the bulk, and no chiral motion is apparent in the difference picture. We interpret the absence of chiral motion for both experimental preparation protocols as a sign that the system has entered a topologically trivial regime.

To more systematically investigate the transition into the topologically trivial regime, we perform scans of the disorder strength $\overline{V}_D$ at different modulation frequencies of the lattice, observing the center-of-mass distance $\Delta\bar{y}$ after $50T$. The paths we chose for this investigation are illustrated in a schematic of the phase diagram we expect in Fig. 5.13a: At modulation frequencies much smaller than 11 kHz and for weak disorder, the system is in the anomalous Floquet regime. If we choose the modulation frequency to be significantly larger than 11 kHz while staying at weak disorder, the system is in the Haldane regime. Close to the transition frequency between the two regimes, the disorder-driven phase transition we studied in Fig. 5.11 can be observed. For large disorder, one expects both systems to end up in a topologically trivial regime. However, the anomalous Floquet topological insulator is expected to show greater robustness due to the protection of topological properties by Floquet symmetry, while Chern insulators are only robust to disorder on the order of magnitude of the bandgap [96]. Our results presented in Chapter 4 also indicate that the

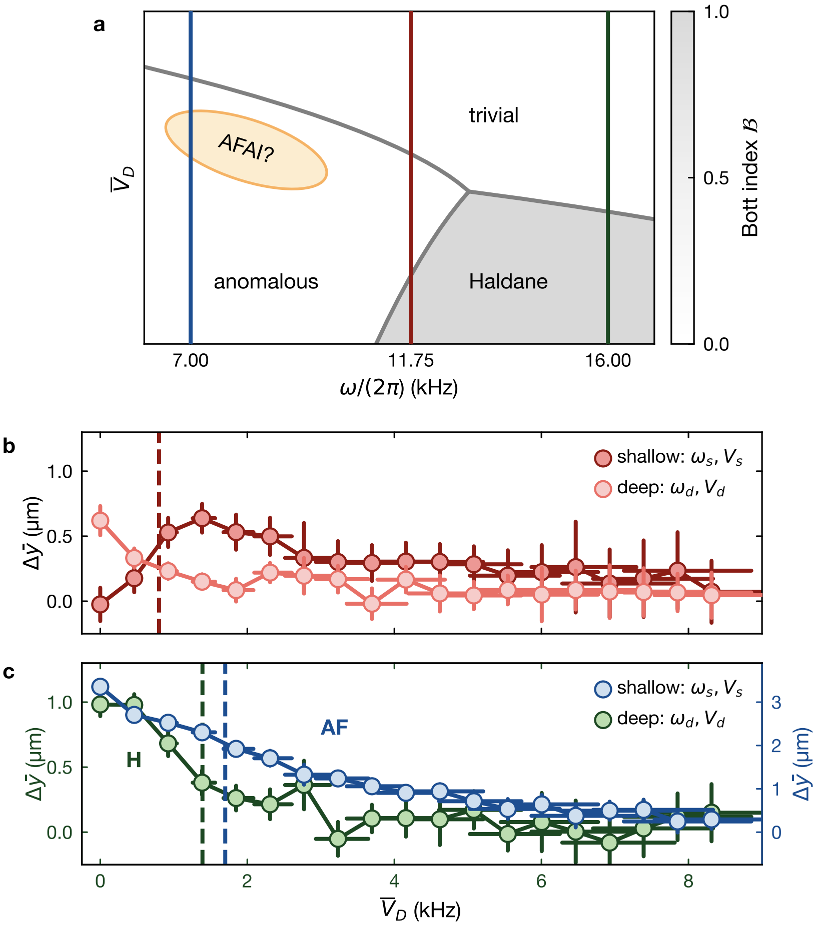

Figure 5.13 | Exploring the topological phase diagram for large potential disorder. a Schematic phase diagram illustrating three different phases: anomalous Floquet, Haldane and topologically trivial. The orange ellipse indicates the potential region of an anomalous Floquet Anderson insulator (AFAI) phase. The vertical lines indicate the parameter regime for the experimental data shown in **b**, **c**. **b**, **c** Center of mass distance $\Delta\bar{y}$ after $50T$ for variable disorder strength and different modulation parameters. The dashed vertical lines indicate the corresponding minimal energy gap without disorder obtained from a 6-band calculation. **b** Re-entrance behavior of the edge mode signal for two different experimental settings optimized for the anomalous (dark red) and Haldane (light red) regime, respectively. The modulation frequency $\omega/(2\pi) = 11.75$ kHz is chosen to lie above, but close to the phase transition at zero disorder. **c** Transition to the topologically trivial regime deep in the anomalous [blue, $\omega/(2\pi) = 7$ kHz] and Haldane regime [green, $\omega/(2\pi) = 16$ kHz]. Error bars on $\Delta\bar{y}$ have been extracted by bootstrapping. The error bars in $\overline{V}_D$ give the calibration error of the disorder strength. The blue trace has been plotted on a separate axis on the right due to the much larger center of mass distance traversed. Each data point is the average of 19-20 measurements per chirality, with different disorder patterns applied.

relevant energy scale in the anomalous regime is determined by the width of the Floquet Brillouin zone, which is much larger than the bandgap. Anomalous Floquet systens also support novel phases, where all bulk states are localized, coexisting with extended edge modes, so-called anomalous Floquet Anderson insulators [66, 67, 108]. This phase is symbolized by the ellipse at the large-disorder end of the anomalous Floquet regime in the phase diagram (AFAI?) in Fig. 5.13a.

In Fig. 5.13b, the results obtained for both the shallow tweezer settings as well as for the deep tweezer settings at a modulation frequency $\omega/(2\pi) = 11.75\,\mathrm{kHz}$ are shown. This modulation frequency was chosen to be right next to the phase transition between the anomalous and the Haldane regime, situated in the Haldane regime in the absence of disorder. The path along which data was acquired here is marked in red in the phase diagram in subfigure a. For the shallow tweezer setting, we do not observe any chiral transport if no disorder is applied, as expected. If the disorder strength is now increased, the emergence of chiral transport becomes apparent, marking the transition from the Haldane- into the anomalous Floquet regime, which we already observed in Sec. 5.3.3. This re-entrant behavior occurs for disorder strengths on the same order of magnitude as the minimal band gap in this measurement, illustrated by the red dashed line. The measured center-of-mass distance $\Delta\bar{y}$ becomes maximal near $\overline{V}_D/h \approx 1.5\,\mathrm{kHz}$, and subsequently decreases gradually, which we interpret as a transition into the topologically-trivial phase.

If the system is instead probed using the deep tweezer settings, one does observe chiral transport if no disorder is applied. This is expected, as the system is initially in the Haldane regime, for which the deep tweezer settings optimize the overlap with the edge mode. If the disorder strength is however increased, the measured center-of-mass distance decreases rather quickly, and edge transport is no longer observable, further supporting that at large disorders the system enters the trivial regime.

In a second set of measurements, displayed in Fig. 5.13c, we study the propagation of the edge mode populated using the shallow tweezer settings deep in the anomalous Floquet regime ($\omega/(2\pi) = 7\,\mathrm{kHz}$, marked by the blue cut in the phase diagram) as well as the propagation of the edge mode populated using the deep tweezer settings in the Haldane regime ($\omega/(2\pi) = 16\,\mathrm{kHz}$, marked by the green cut in the phase diagram). The modulation frequencies were chosen to ensure a realtively large 0-gap, while not being in the vicinity of the phase transition between the anomalous- and the Haldane regime.

When populating the edge mode at $\omega/(2\pi) = 16\,\mathrm{kHz}$ using the deep tweezer settings, one observes chiral transport in the absence of disorder. If disorder is applied, the center-of-mass distance $\Delta\bar{y}$ starts to decrease, with no clear signal recognizable past $\overline{V}_D/h = 4\,\mathrm{kHz}$. The green dashed line in the subfigure marks the smallest energy gap between the two bands at these modulation parameters, which is at a comparable energy scale as the decrease in edge transport. This supports the expectation, that for the Haldane system the topological protection of the system breaks down when disorder closes the band gap.

In the anomalous Floquet regime, when probing the edge mode using the shallow tweezer settings at $\omega/(2\pi) = 7\,\mathrm{kHz}$, qualitatively similar behavior can be observed: A strong signal is visible in the absence of disorder, with $\Delta\bar{y}$ decreasing if disorder is introduced. However, the overall transport is significantly faster – note that the vertical scale is different for data taken in the Haldane- and in the anomalous Floquet regime. It is also striking, that, even though the minimal energy gap is comparable to the minimal energy gap at

$\omega/(2\pi) = 16\,\mathrm{kHz}$, transport persists for significantly longer when disorder is introduced. Previous work [79, 96, 109] indicates, that the relevant energy scale for anomalous Floquet systems is determined by the width of the Floquet Brillouin zone, which in this case is $\omega/(2\pi) = 7\,\mathrm{kHz}$, being significantly larger than the minimal energy gap of the system.

This observation further supports work suggesting an enhanced robustness of anomalous Floquet topological insulators (AFTIs) compared to conventional Chern insulators [96, 109].

5.5 Effect of disorder on the bulk propagation

While the previous sections of this chapter focused on the effect disorder has on the propagation of edge modes, and on the phase diagram of our Floquet-modulated system, in the following we will focus on the transport properties in the bulk, if the system is subjected to disorder.

The transport properties of non-interacting bosons in an optical lattice are fundamentally determined by the system's band structure [237, 238]. Here, in the absence of disorder, the band velocity $v_g(\mathbf{k})$ is determined by the gradient of the dispersion relation,

$$v_g(\mathbf{k}) = \frac{1}{\hbar}\frac{\partial E(\mathbf{k})}{\partial \mathbf{k}}. \tag{5.7}$$

As discussed in Sec. 2.5.1, this behavior will be modified if disorder is introduced into the system: Here, scattering events will lead to diffusive propagation, and weak localization will reduce the propagation velocity even further. While Anderson localization is expected to occur in any given infinitely sized non-interacting two-dimensional system for arbitrarily low disorder, it is especially hard to observe in 2D systems: Here, the localization length can reach scales on the order of the system size, making it hard to unambiguously observe localization.

We start our investigation in the Haldane regime, at $\omega/(2\pi) = 16\,\mathrm{kHz}$. To probe bulk transport here, we place atoms on a few lattice sites of our system, using the optical tweezer at the shallow tweezer depth, $\omega_s/(2\pi) = 1.3(1)\,\mathrm{kHz}$. Remaining atoms have been expelled by reducing the potential of the crossed dipole trap briefly, with the sequence is identical to the one presented in Fig. 5.1, with the exception of the DMD potential not being turned on.

First, we focus on the expansion in the absence of any disorder, with averaged absorption pictures for $t \in [0T, 20T, 40T, 60T, 80T, 100T, 120T]$ being presented in Fig. 5.14a. At $t = 0T$, the initial state released from the tweezer is displayed, populating a few lattice sites. If the system is left to evolve, one sees the atoms spread out according to Eq. 5.7, evolving into a hexagonal shape, which stays observable even for the longest observation time, expanding over $25\,\mu\mathrm{m} \approx 87a$ from the initial position.

Introducing disorder into the system alters the propagation drastically, as shonw in Fig. 5.14b for $\overline{V}_D/h = 0.46\,\mathrm{kHz}$, and c for $\overline{V}_D/h = 0.92\,\mathrm{kHz}$: Here, only for the lower disorder value and for the shortest evolution time $t = 20T$ a slightly hexagonal shape is still observable. For longer evolution times, the atoms spread out isotropically, with the transport for

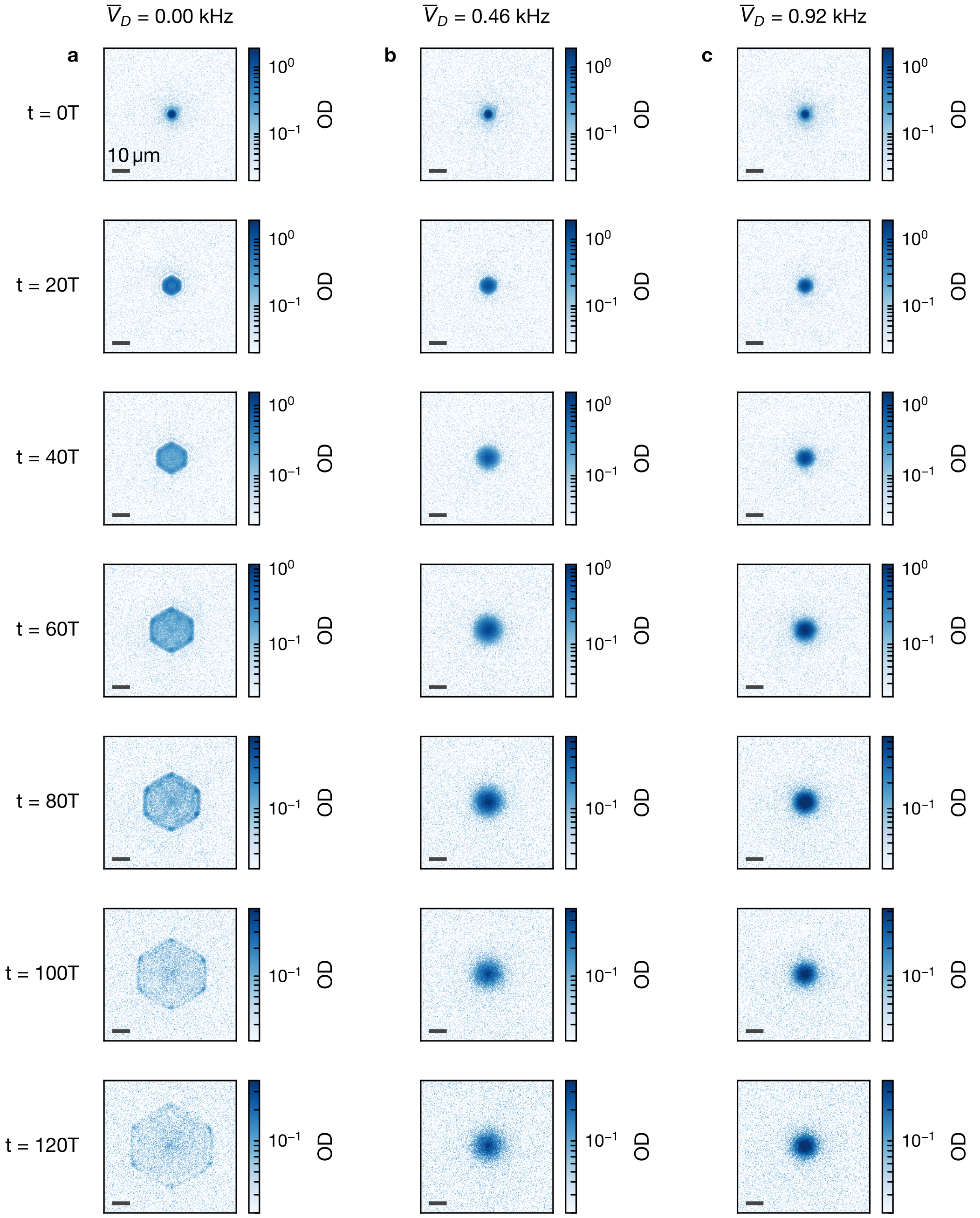

Figure 5.14 | Haldane bulk expansion in the presence of disorder. Atoms are released from the shallow tweezer ($(\omega_s/(2\pi) = 1.3(1)$ kHz) into the lattie at $\omega/(2\pi) = 16$ kHz, deep in the Haldane regime. Each absorption picture is averaged over 39-40 experimental disorder realizations. Only data for chirality $\kappa = 1$ is shown, with data taken for $\kappa = -1$ looking identical. The evolution time of the system is increased from top to bottom. Data is taken for **a** no disorder, **b** $\overline{V}_D/h = 0.46$ kHz, and **c** $\overline{V}_D/h = 0.92$ kHz. The scalebar in the bottom left of each picture has length 10 µm. Note that the optical density is scaled logarithmically to show data at high and low densities simultaneously.

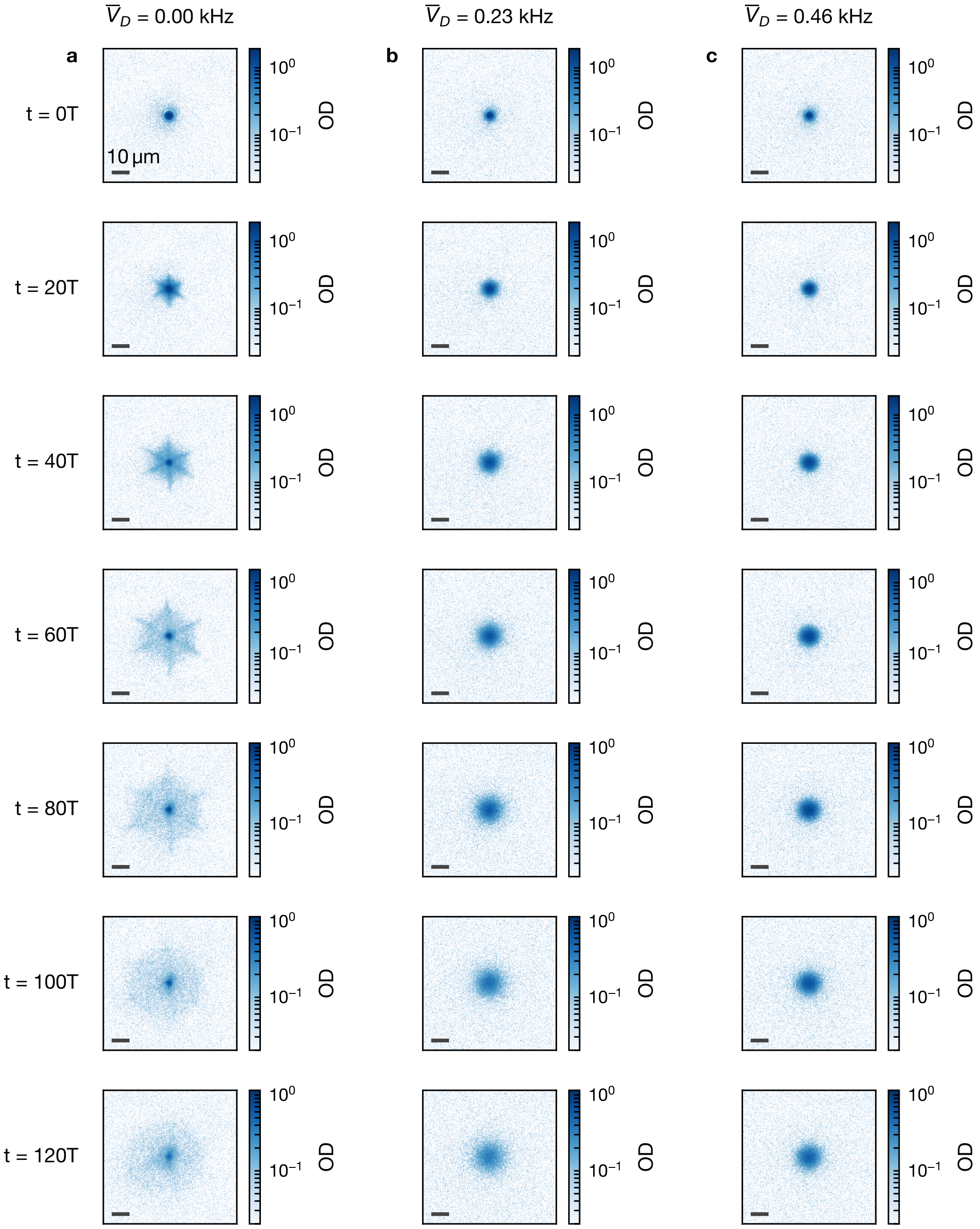

Figure 5.15 | Anomalous bulk expansion in the presence of disorder. Atoms are released from the shallow tweezer into the lattie at $\omega/(2\pi) = 7$ kHz, deep in the anomalous regime. Each absorption picture is averaged over 39-40 experimental disorder realizations. Only data for chirality $\kappa = 1$ is shown, with data taken for $\kappa = -1$ looking identical. The evolution time of the system is increased from top to bottom. Data is taken for **a** no disorder, **b** $\overline{V}_D/h = 0.23$ kHz, and **c** $\overline{V}_D/h = 0.46$ kHz. The scalebar in the bottom left of each picture has length 10 µm. Note that the optical density is scaled logarithmically to show data at high and low density simultaneously.

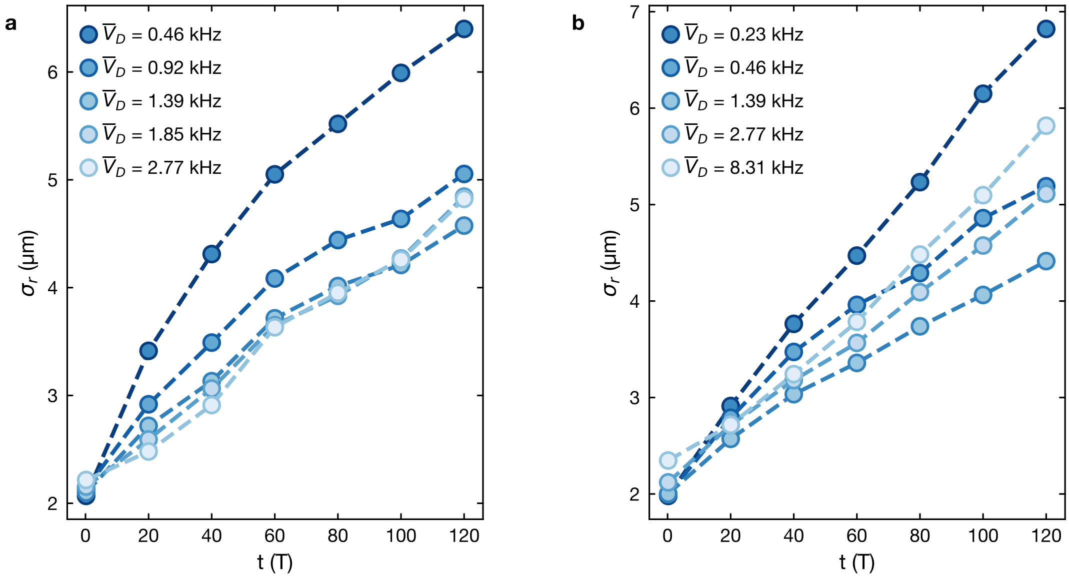

Figure 5.16 | Bulk expansion with in the Haldane- and anomalous regime. The radial width σ_r of a 2D Gaussian fit to a cloud expanding in the bulk of the lattice ($\kappa = 1$) after release from the shallow tweezer. **a** shows data taken at $\omega/(2\pi) = 16$ kHz in the Haldane regime, **b** shows data taken at $\omega/(2\pi) = 7$ kHz in the anomalous Floquet regime. The uncertainty in the estimation of the radial width has been extracted via a bootstrapping resampling method, with error bars hidden behind the data points. The widths are fit to the absorption pictures averaged over 39-40 different experimental disorder realizations.

the larger disorder value in subfigure c being slower. Noticably, this system does not appear to suffer from the atom loss observed in the edge state at the same modulation parameters in Fig. 5.6, which is not yet fully understood. While the atom number in the expansion in the absence of disorder is hard to quantify due to the large system size, no drastic atom loss can be observed in the presence of disorder. Potentially, spectral noise in the step potential projected by the DMD might drive transitions to higher-lying bands of the system, so that an adjustment of the modulation scheme or of the lattice depth might allow for the observation of the edge states for longer times. Alternatively, the presence of disorder might have a stabilizing effect on the bulk, in analogy to the system investigated in [239] in the presence of interactions. Additional data was taken at larger disorder strengths up to $\overline{V}_D/h = 2.77\,\text{kHz}$, but is not shown here, as no clear difference to the data presented in subfigure c can be seen.

In the following, we repeat these measurement in the anomalous Floquet regime of our system, at $\omega/(2\pi) = 7\,\text{kHz}$. In Fig. 5.15a, the expansion of a wavepacket in the absence of disorder is shown. Here, the dispersion of the Floquet bands is significantly modified compared to the static case, such that the observed expansion represents a star-shape. Clearly visible is a dark spot in the center of the system, which is not propagating due to the reduced band velocity, stemming from the flattened bands. For evolution times $t \geq 100T$, this pattern washes out, with the rays originating in the center no longer being observable. This might hint at the system dephasing or decohering, but these features could potentially also be recovered by higher averaging of the data.

In Fig. 5.15b and c the evolution of a wavepacket is shown in the presence of disorder for $\overline{V}_D = 0.23\,\mathrm{kHz}$ and $\overline{V}_D = 0.46\,\mathrm{kHz}$, respectively. The disorder strengths displayed were deliberately chosen lower here, as due to the flattened bands a larger impact of the disorder on the transport is expected. The behavior is qualitatively similar to the behavior in the Haldane regime: Only after $t = 20T$ and for the lower disorder strength, some anisotropic transport, following the star-shape observed in the clean system, can be observed. Apart from that, the clouds appear to be rotationally symmetric, and spread out slowly, with the transport velocity being lower for the larger disorder strength.

To more quantitatively study this behavior, we extract the width of the clouds by fitting them with a radially symmetric 2D Gaussian,

$$\mathrm{OD}(\mathbf{r}) = A \cdot e^{-(\mathbf{r}-\mathbf{r_0})^2/(2\sigma_r^2)} \tag{5.8}$$

with the results for σ_r displayed in Fig. 5.16. Here, the amplitude A and the center position $\mathbf{r_0}$ of the Gaussian were treated as free parameters. In Fig. 5.16a, the widths in the Haldane regime are shown for $\overline{V}_D/h \in [0.46\,\mathrm{kHz}, 0.92\,\mathrm{kHz}, 1.39\,\mathrm{kHz}, 1.85\,\mathrm{kHz}, 2.77\,\mathrm{kHz}]$. Uncertainties in the estimation of the width have been determined via bootstrapping, with the error bars being hidden behind the data points. It is apparent, that at the lowest two disorder strengths, the expansion occurs slightly faster compared to the curves for larger disorder, which appear to collapse onto a single curve.

In the anomalous regime, similar behavior can be observed: Here, disorder strengths $\overline{V}_D/h \in [0.23\,\mathrm{kHz}, 0.46\,\mathrm{kHz}, 1.39\,\mathrm{kHz}, 2.77\,\mathrm{kHz}, 8.31\,\mathrm{kHz}]$ are shown, with the propagation at larger disorder being measured due to the larger robustness of the edge mode. For the lowest disorder, the cloud clearly expands slightly faster, while the propagation slows down for larger values. The curves do not collapse onto a single curve as in the Haldane regime, instead a decrease followed by an increase is visible. A minimum in the propagation appears around $\overline{V}_D/h = 1.39\,\mathrm{kHz}$, where the disorder strength coincides with the width of the bands.

In all measurements however, it is clear that the system is not fully localized, with the cloud further expanding even for the longest ovservation time, $t = 120T$, which equals 7.5 ms in the Haldane regime, and ≈ 17 ms in the anomalous regime. As no strong atoms loss is visible even for the longest evolution times, the investigation at even longer times might be insightful in future experiments.

CHAPTER 6

Conclusion and Outlook

This thesis investigates the properties of Floquet-modulated Bloch bands, both in the presence and the absence of disorder, through real-space detection of the chiral edge states. The periodic modulation of tunnel couplings enables the realization of different topological regimes, with a primary focus on the Haldane regime, which constitutes a Chern insulator, and on the anomalous Floquet regime, a genuine out-of-equilibrium phase.

The population of chiral edge states in this thesis was accomplished by utilizing an optical tweezer, enabling the placement of a tightly confined wave packet in the lattice, in combination with a digital micromirror device, projecting an adjacent potential step to serve as a topological interface. Adjusting the precise parameters of this preparation protocol allowed us to selectively populate the edge modes in three distinct topological regimes. To probe the emergence of the edge state, the height of the potential step was varied, which uncovered the relevant energy scales in the different regimes. This led to the observation that the relevant energy scale in anomalous Floquet systems is tied to the modulation frequency, as opposed to the lattice tunneling. Further investigation of the dependence of the chiral transport velocity on the width of the potential step in the Haldane regime revealed that the velocity is decreases with increasing interface widths, a result which is in agreement with theoretical predictions [154–156].

To explore the effect of disorder on topological phases of matter, we implemented a setup for generating high-resolution disorder potentials. In this setup, a diffuser is illuminated with coherent light, and its Fourier plane is projected onto the atomic plane, yielding a speckle pattern. We characterized the correlation length of the resulting pattern, and developed a novel method for calibrating the disorder strength in situ, by performing diffraction measurements on the atomic cloud, and by comparing our observation to numerical simulations. We studied the effect of this disorder potential on the edge transport in a Haldane system and observed disorder-induced velocity renormalization of edge-mode propagation [235].

By exploiting the dependence of the edge mode population on the specific preparation protocol, we were able to distinguish two distinct topological regimes, using the existence of chiral transport as an observable, and to extract the location of the phase transition between the two regimes. After applying disorder to the system, we observed a disorder-driven phase transition between these two topologically nontrivial phases, which is in good agreement with theoretical predictions [109]. Furthermore, we studied the breakdown of chiral transport in the presence of strong disorder, observing enhanced robustness of the edge modes in the anomalous Floquet regime.

The disorder-driven phase transition between the anomalous Floquet and Haldane regime offers a novel pathway for probing the physics emerging at the interface between Chern insulators and genuine out-of-equilibrium systems. Locally introducing disorder into an optical lattice system – e.g. by projecting disorder using a digital micromirror device – might allow to selectively drive regions of the lattice into the anomalous Floquet phase. The geometry of this interface can then be tailored, ranging from a straight boundary to a quantum point contact. Such quantum point contacts are routinely used in condensed matter systems to investigate the topological properties of materials, with a large number of experiments investigating topological systems in the presence of interactions [240–248].

Further improvements on the experimental platform would enable us to populate the edge mode of the system at multiple locations with a constant phase difference, or allow for the splitting and recombination of edge modes. An interesting addition to the platform at this point would be the implementation of an improved detection system described in [204], enabling us to study the propagation and dynamics of the edge mode with single-site resolution.

While for the experiments presented in this thesis the choice of tweezer trap frequency allowed for some selectivity regarding which edge state will be populated, finer spectral resolution would enable us to populate edge modes in a more controlled manner. In this regard, it might be helpful to implement a cold-atom-elevator [233], in which an atom reservoir with tunable potential energy offset with respect to the system under investigation is separated from it by a wall potential with a small hole allowing for leakage of the atoms into the edge mode of the system. By tuning the potential energy offset between the two systems, the edge mode of the system under investigation can be populated in an energy selective manner.

Building upon the single-particle systems investigated in this thesis, the incorporation of many-body interactions represents the natural next step, paving the way to exploring the rich landscape of strongly correlated topological phases of matter. One challenge here is the lifetime, as periodically driven, interacting, closed systems will heat up to infinite temperatures in the long-time limit [249, 250]. Previous work has investigated the relevant timescales and limiting factors for this on our experimental platform [206], showing that a tighter confinement of the system in z-direction together with an active stabilization of the phases of the lattice beams could reduce the heating rates. Additionally, the engineering of multi-tone drives might help to further suppress heating [251, 252].

The implementation of an optical flux lattice presents an alternative approach to prevent Floquet heating while achieving high flux densities [253–255]. Although lattices of this kind inherently generate highly non-uniform fields, a recent proposal suggests that supplementing them with an additional scalar potential may enable the creation of topologically non-trivial flat Bloch bands [256]. A key challenge to this approach, however, is the potential for magnetic field noise to introduce non-uniform perturbations across the system. Investigating the impact of such noise is crucial, particularly as the precise stabilization of magnetic fields remains a significant experimental challenge.

Furthermore, introducing disorder into the topological Bloch bands of our platform enables the investigation of exotic Floquet topological phases. Although the anomalous Floquet systems realized in this work exhibit many properties of conventional Chern insulators, such as quantized chiral edge transport, they also can host entirely novel phases. A prime example is the Anomalous Floquet Anderson Insulator (AFAI), a phase characterized by a fully localized bulk that coexists with robustly conductive edge states [66, 67]. A remarkable feature of the AFAI phase is its predicted resilience not only to spatial disorder but also to temporal noise [257, 258]. This exceptional stability suggests that its topological properties might extend into interacting regimes, potentially opening new avenues for research on topological many-body systems [239]. Significantly, theoretical work predicts the existence of an AFAI phase in the specific modulation scheme utilized in this thesis [108].

Appendices

Appendix A: Independence of the results from the initial tweezer position

The measurements presented in Chapter 5 rely on an alignment of the optical tweezer with respect to the hard-wall potential prior to data acquisition, as described in Sec. 5.1. This optimization enables sufficient data collection for reliable disorder averaging while maintaining reasonable measurement durations for a dataset. To ensure that our results are not artifacts of this specific alignment procedure, we performed additional measurements with reduced sampling density and fewer disorder realizations at multiple tweezer positions. This appendix demonstrates that the observed phenomena remain consistent across different initial preparation positions.

Before each experimental run, the position of the optical tweezer was aligned relative to the potential step by varying the tweezer position perpendicular to the wall, finding the maximum integrated absolute differential signal $|\mathrm{OD}_{\kappa=1} - \mathrm{OD}_{\kappa=-1}|$ after $50T$ in a region along the edge. This optimization was performed separately for the shallow- and for the deep tweezer settings: For the shallow tweezer settings ($\omega_s = 1.3(1)\,\mathrm{kHz}$, $V_s/h = 13.2\,\mathrm{kHz}$) the signal was optimized at $\omega/(2\pi) = 7\,\mathrm{kHz}$, while for the deep tweezer settings ($\omega_d = 2.0(1)\,\mathrm{kHz}$, $V_d/h = 2.8\,\mathrm{kHz}$) the optimization was performed at $\omega/(2\pi) = 16\,\mathrm{kHz}$.

In Fig. A.1 the measurements presented in Fig. 5.11 are repeated. Apart from the optimized position, here data was also taken when releasing the atoms from the tweezer displaced by $\pm 0.48\,\mu\mathrm{m}$ perpendicular to the hard wall potential. The data reveals excellent qualitative and quantitative agreement of the results across the three positions. The disorder-induced shift of the phase transition remains clearly observable regardless of initial position, and the extracted transition frequencies are consistent within their error bars. This measurement also exhibits the same divergence from the two-band Bott index calculation as observed in Fig. 5.11, further emphasizing the influence of higher-lying bands for this shift.

Fig. A.2 presents measuremets of the edge transport in the strong-disorder regime, analogous to the results presented in Fig. 5.13. Measurements were again performed at three different tweezer positions: The optimized position as well as tweezer positions displaced by $\pm 0.48\,\mu\mathrm{m}$ perpendicular to the hard wall potential. For the deep tweezer settings, the position closer to the hard-wall potential (labeled $-0.48\,\mu\mathrm{m}$) does not show any edge transport.

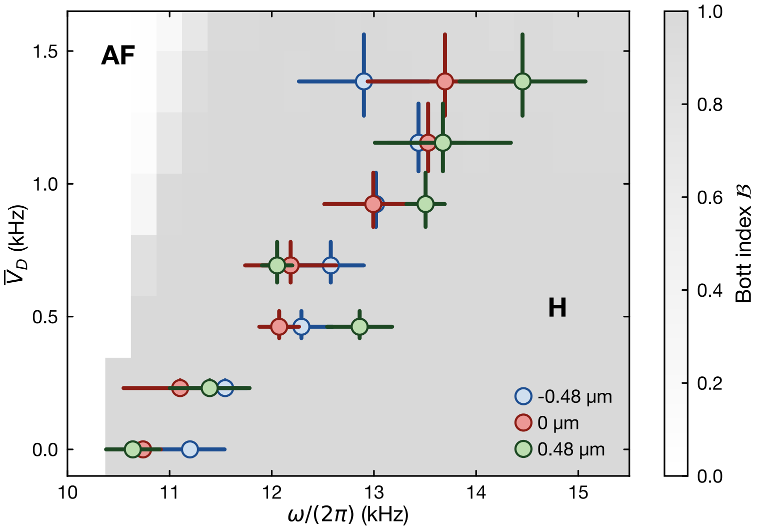

Figure A.1 | Tracking the phase transition for different initial positions. Location of the phase transition as a function of disorder, with data taken at three different tweezer positions perpendicular to the wall. The location of the phase transition has been determined via a fit to the center-of-mass distance $\Delta\bar{y}$ after $50T$ for different amplitude modulation frequencies at a given disorder, analogous to Fig. 5.11. Each of the data points in the fit is the average over 5 to 7 different disorder realizations. The horizontal error bars indicate the fit error, while the vertical error bars represent the error on the disorder calibration. The gray shading in the background encodes the Bott index $\mathcal{B}$.

Analysis of individual experimental realizations reveals that atoms are placed directly on the potential step at this position, where corrugations of the optical potential hinder transport. The remaining measurements demonstrate behavior consistent with Fig. 5.13: At $\omega/(2\pi) = 11.75\,\mathrm{kHz}$, a fast decay of the edge transport is occurs for the deep tweezer settings, while for the shallow tweezer settings the re-emergent behavior of the edge state can be observed. For the results at $\omega/(2\pi) = 7\,\mathrm{kHz}$ and $16\,\mathrm{kHz}$, the transport decays with increasing disorder potential strength $\overline{V}_D$, with the edge transport in the Anomalous Floquet regime again staying robust for longer compared to the transport in the Haldane regime.

These measurements demonstrate the our experimental results are robust against variations in the precise preparation protocol, and underline that the observed disorder-driven phase transitions are a robust feature of the underlying system. While the initial alignment of the tweezer position is helpful for optimizing the strength of the chiral signal, it is not essential for the observation of the results presented in this thesis.

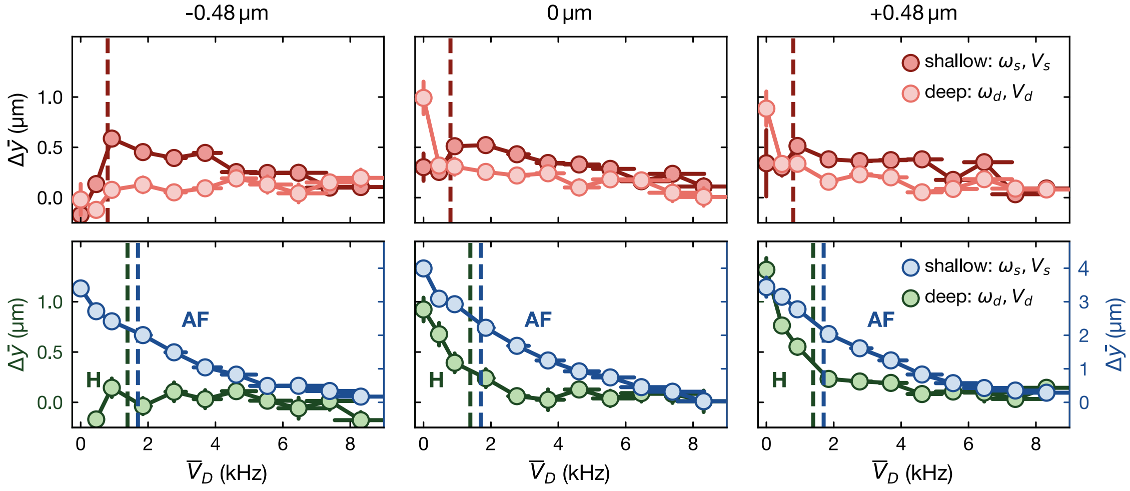

Figure A.2 | Effect of large potential disorder for different initial positions. Center-of-mass distance $\Delta\bar{y}$ measured after $50T$ as a function of disorder strength at $\omega/(2\pi) = 11.75$ kHz (top), 7 kHz (blue) as well as 16 kHz (green). Error bars on $\Delta\bar{y}$ were extracted via bootstrapping, while horizontal error bars indicate the uncertainty in disorder calibration. At 11.75 kHz was collected using both shallow and deep tweezer settings, while measurements at 7 kHz used only the shallow configuration, and those at 16 kHz only the deep tweezer settings. Data was taken at three initial tweezer positions perpendicular to the wall, with 0 µm denoting the optimized position where data is typically collected. Each data point represents an average over 16-17 different disorder realizations. The vertical dashed lines mark the minimal energy gap of the system at each modulation frequency. Note that the data for 7 kHz has been plotted on a separate axis marked on the right due to its much larger velocity.

Bibliography

[1] X.-L. Qi and S.-C. Zhang, *Topological insulators and superconductors*, Reviews of Modern Physics **83**, Publisher: American Physical Society, 1057 (2011).

[2] L. D. Landau and E. M. Lifshitz, *Statistical Physics: Volume 5*, Englisch (Butterworth-Heinemann, Amsterdam Heidelberg, 1980).

[3] N. W. Ashcroft and N. D. Mermin, *Solid State Physics*, en (Holt, Rinehart and Winston, 1976).

[4] S. M. Girvin and K. Yang, *Modern Condensed Matter Physics*, Englisch (Cambridge University Pr., Cambridge New York, 2019).

[5] K. von Klitzing, G. Dorda, and M. Pepper, *New Method for High-Accuracy Determination of the Fine-Structure Constant Based on Quantized Hall Resistance*, Phys. Rev. Lett. **45**, Publisher: American Physical Society, 494 (1980).

[6] K. von Klitzing, *The quantized Hall effect*, Reviews of Modern Physics **58**, Publisher: American Physical Society, 519 (1986).

[7] K. von Klitzing, T. Chakraborty, P. Kim, V. Madhavan, X. Dai, J. McIver, Y. Tokura, L. Savary, D. Smirnova, A. M. Rey, C. Felser, J. Gooth, and X. Qi, *40 years of the quantum Hall effect*, en, Nature Reviews Physics **2**, Publisher: Nature Publishing Group, 397 (2020).

[8] S. Sachdev, *Quantum Phase Transitions*, 2nd ed. (Cambridge University Press, Cambridge, 2011).

[9] M. Z. Hasan and C. L. Kane, *Colloquium: Topological insulators*, Reviews of Modern Physics **82**, Publisher: American Physical Society, 3045 (2010).

[10] X.-G. Wen, *Colloquium: Zoo of quantum-topological phases of matter*, Reviews of Modern Physics **89**, Publisher: American Physical Society, 041004 (2017).

[11] R. B. Laughlin, *Quantized Hall conductivity in two dimensions*, Phys. Rev. B **23**, Publisher: American Physical Society, 5632 (1981).

[12] B. Jeckelmann and B. Jeanneret, *The quantum Hall effect as an electrical resistance standard*, en, Reports on Progress in Physics **64**, 1603 (2001).

[13] R. E. Prange, *Quantized Hall resistance and the measurement of the fine-structure constant*, Phys. Rev. B **23**, Publisher: American Physical Society, 4802 (1981).

[14] H. Aoki and T. Ando, *Effect of localization on the hall conductivity in the two-dimensional system in strong magnetic fields*, Solid State Communications **38**, 1079 (1981).

[15] P. Phillips, *Advanced Solid State Physics*, 2nd ed. (Cambridge University Press, 2012).

[16] D. J. Thouless, M. Kohmoto, M. P. Nightingale, and M. den Nijs, *Quantized Hall Conductance in a Two-Dimensional Periodic Potential*, Phys. Rev. Lett. **49**, Publisher: American Physical Society, 405 (1982).

[17] D. Newell and E. Tiesinga, *The International System of Units (SI), 2019 Edition*, en, NIST, Last Modified: 2021-03-16T05:00-04:00 Publisher: David Newell, Eite Tiesinga (2019).

[18] S.-c. Zhang, *Topological states of quantum matter*, en, Physics **1**, Publisher: American Physical Society, 6 (2008).

[19] M. Nakahara, *Geometry, Topology and Physics*, 2nd ed. (CRC Press, Boca Raton, 2018).

[20] M. Z. Hasan and J. E. Moore, *Three-Dimensional Topological Insulators*, en, Annual Review of Condensed Matter Physics **2**, Publisher: Annual Reviews, 55 (2011).

[21] R. Moessner and J. E. Moore, *Topological Phases of Matter* (Cambridge University Press, Cambridge, 2021).

[22] A. Altland and M. R. Zirnbauer, *Nonstandard symmetry classes in mesoscopic normal-superconducting hybrid structures*, Phys. Rev. B **55**, Publisher: American Physical Society, 1142 (1997).

[23] P. Heinzner, A. Huckleberry, and M. Zirnbauer, *Symmetry Classes of Disordered Fermions*, en, Communications in Mathematical Physics **257**, 725 (2005).

[24] F. D. M. Haldane, *Model for a Quantum Hall Effect without Landau Levels: Condensed-Matter Realization of the "Parity Anomaly"*, Phys. Rev. Lett. **61**, Publisher: American Physical Society, 2015 (1988).

[25] C. L. Kane and E. J. Mele, *Quantum Spin Hall Effect in Graphene*, Phys. Rev. Lett. **95**, Publisher: American Physical Society, 226801 (2005).

[26] B. A. Bernevig, T. L. Hughes, and S.-C. Zhang, *Quantum Spin Hall Effect and Topological Phase Transition in HgTe Quantum Wells*, Science **314**, Publisher: American Association for the Advancement of Science, 1757 (2006).

[27] B. A. Bernevig and S.-C. Zhang, *Quantum Spin Hall Effect*, Phys. Rev. Lett. **96**, Publisher: American Physical Society, 106802 (2006).

[28] M. Koenig, S. Wiedmann, C. Bruene, A. Roth, H. Buhmann, L. W. Molenkamp, X.-L. Qi, and S.-C. Zhang, *Quantum Spin Hall Insulator State in HgTe Quantum Wells*, en, Science **318**, 766 (2007).

[29] D. C. Tsui, H. L. Stormer, and A. C. Gossard, *Two-Dimensional Magnetotransport in the Extreme Quantum Limit*, Phys. Rev. Lett. **48**, Publisher: American Physical Society, 1559 (1982).

[30] R. B. Laughlin, *Anomalous Quantum Hall Effect: An Incompressible Quantum Fluid with Fractionally Charged Excitations*, Phys. Rev. Lett. **50**, Publisher: American Physical Society, 1395 (1983).

[31] H. L. Stormer, D. C. Tsui, and A. C. Gossard, *The fractional quantum Hall effect*, Reviews of Modern Physics **71**, Publisher: American Physical Society, S298 (1999).

[32] C. Nayak, S. H. Simon, A. Stern, M. Freedman, and S. Das Sarma, *Non-Abelian anyons and topological quantum computation*, Reviews of Modern Physics **80**, Publisher: American Physical Society, 1083 (2008).

[33] A. Stern, *Non-Abelian states of matter*, en, Nature **464**, Publisher: Nature Publishing Group, 187 (2010).

[34] M. H. Anderson, J. R. Ensher, M. R. Matthews, C. E. Wieman, and E. A. Cornell, *Observation of Bose-Einstein Condensation in a Dilute Atomic Vapor*, EN, Science, Publisher: American Association for the Advancement of Science, 10.1126/science.269.5221.198 (1995).

[35] K. B. Davis, M. .-. Mewes, M. R. Andrews, N. J. van Druten, D. S. Durfee, D. M. Kurn, and W. Ketterle, *Bose-Einstein Condensation in a Gas of Sodium Atoms*, Phys. Rev. Lett. **75**, Publisher: American Physical Society, 3969 (1995).

[36] B. DeMarco and D. S. Jin, *Onset of Fermi Degeneracy in a Trapped Atomic Gas*, Science **285**, Publisher: American Association for the Advancement of Science, 1703 (1999).

[37] S. Inouye, M. R. Andrews, J. Stenger, H.-J. Miesner, D. M. Stamper-Kurn, and W. Ketterle, *Observation of Feshbach resonances in a Bose–Einstein condensate*, en, Nature **392**, Publisher: Nature Publishing Group, 151 (1998).

[38] E. Timmermans, P. Tommasini, M. Hussein, and A. Kerman, *Feshbach resonances in atomic Bose–Einstein condensates*, Physics Reports **315**, 199 (1999).

[39] C. Chin, R. Grimm, P. Julienne, and E. Tiesinga, *Feshbach resonances in ultracold gases*, Reviews of Modern Physics **82**, Publisher: American Physical Society, 1225 (2010).

[40] L. Tarruell, D. Greif, T. Uehlinger, G. Jotzu, and T. Esslinger, *Creating, moving and merging Dirac points with a Fermi gas in a tunable honeycomb lattice*, en, Nature **483**, Publisher: Nature Publishing Group, 302 (2012).

[41] M. N. Kosch, L. Asteria, H. P. Zahn, K. Sengstock, and C. Weitenberg, *Multifrequency optical lattice for dynamic lattice-geometry control*, Physical Review Research **4**, Publisher: American Physical Society, 043083 (2022).

[42] J.-C. Yu, S. Bhave, L. Reeve, B. Song, and U. Schneider, *Observing the two-dimensional Bose glass in an optical quasicrystal*, en, Nature **633**, Publisher: Nature Publishing Group, 338 (2024).

[43] C. C. Bradley, C. A. Sackett, J. J. Tollett, and R. G. Hulet, *Evidence of Bose-Einstein Condensation in an Atomic Gas with Attractive Interactions*, Phys. Rev. Lett. **75**, Publisher: American Physical Society, 1687 (1995).

[44] I. Bloch, J. Dalibard, and W. Zwerger, *Many-body physics with ultracold gases*, Reviews of Modern Physics **80**, Publisher: American Physical Society, 885 (2008).

[45] C. Gross and I. Bloch, *Quantum simulations with ultracold atoms in optical lattices*, Science **357**, Publisher: American Association for the Advancement of Science, 995 (2017).

[46] W. S. Bakr, A. Peng, M. E. Tai, R. Ma, J. Simon, J. I. Gillen, S. Fölling, L. Pollet, and M. Greiner, *Probing the Superfluid–to–Mott Insulator Transition at the Single-Atom Level*, Science **329**, Publisher: American Association for the Advancement of Science, 547 (2010).

[47] J. F. Sherson, C. Weitenberg, M. Endres, M. Cheneau, I. Bloch, and S. Kuhr, *Single-atom-resolved fluorescence imaging of an atomic Mott insulator*, en, Nature **467**, Publisher: Nature Publishing Group, 68 (2010).

[48] C. Gross and W. S. Bakr, *Quantum gas microscopy for single atom and spin detection*, en, Nat. Phys. **17**, Publisher: Nature Publishing Group, 1316 (2021).

[49] R. Grimm, M. Weidemüller, and Y. B. Ovchinnikov, *Optical Dipole Traps for Neutral Atoms*, in *Advances In Atomic, Molecular, and Optical Physics*, Vol. 42, edited by B. Bederson and H. Walther (Academic Press, 2000), 95.

[50] S. Eckel, J. G. Lee, F. Jendrzejewski, N. Murray, C. W. Clark, C. J. Lobb, W. D. Phillips, M. Edwards, and G. K. Campbell, *Hysteresis in a quantized superfluid 'atomtronic' circuit*, en, Nature **506**, Publisher: Nature Publishing Group, 200 (2014).

[51] P. Zupancic, P. M. Preiss, R. Ma, A. Lukin, M. E. Tai, M. Rispoli, R. Islam, and M. Greiner, *Ultra-precise holographic beam shaping for microscopic quantum control*, EN, Optics Express **24**, Publisher: Optica Publishing Group, 13881 (2016).

[52] N. Liebster, M. Sparn, E. Kath, J. Duchene, K. Fujii, S. L. Görlitz, T. Enss, H. Strobel, and M. K. Oberthaler, *Observation of Pattern Stabilization in a Driven Superfluid*, Phys. Rev. X **15**, Publisher: American Physical Society, 011026 (2025).

[53] D. Barredo, V. Lienhard, S. de Léséleuc, T. Lahaye, and A. Browaeys, *Synthetic three-dimensional atomic structures assembled atom by atom*, en, Nature **561**, Publisher: Nature Publishing Group, 79 (2018).

[54] D. Bluvstein et al., *Logical quantum processor based on reconfigurable atom arrays*, en, Nature, 10.1038/s41586-023-06927-3 (2023).

[55] J. Dalibard, F. Gerbier, G. Juzeliūnas, and P. Öhberg, *Colloquium: Artificial gauge potentials for neutral atoms*, Reviews of Modern Physics **83**, Publisher: American Physical Society, 1523 (2011).

[56] M. Aidelsburger, M. Atala, M. Lohse, J. T. Barreiro, B. Paredes, and I. Bloch, *Realization of the Hofstadter Hamiltonian with Ultracold Atoms in Optical Lattices*, Phys. Rev. Lett. **111**, Publisher: American Physical Society, 185301 (2013).

[57] H. Miyake, G. A. Siviloglou, C. J. Kennedy, W. C. Burton, and W. Ketterle, *Realizing the Harper Hamiltonian with Laser-Assisted Tunneling in Optical Lattices*, Phys. Rev. Lett. **111**, Publisher: American Physical Society, 185302 (2013).

[58] M. E. Tai, A. Lukin, M. Rispoli, R. Schittko, T. Menke, Dan Borgnia, P. M. Preiss, F. Grusdt, A. M. Kaufman, and M. Greiner, *Microscopy of the interacting Harper–Hofstadter model in the two-body limit*, en, Nature **546**, Publisher: Nature Publishing Group, 519 (2017).

[59] G. Jotzu, M. Messer, R. Desbuquois, M. Lebrat, T. Uehlinger, D. Greif, and T. Esslinger, *Experimental realization of the topological Haldane model with ultracold fermions*, en, Nature **515**, Publisher: Nature Publishing Group, 237 (2014).

[60] M. Tarnowski, F. N. Ünal, N. Fläschner, B. S. Rem, A. Eckardt, K. Sengstock, and C. Weitenberg, *Measuring topology from dynamics by obtaining the Chern number from a linking number*, en, Nature Communications **10**, Publisher: Nature Publishing Group, 1728 (2019).

[61] K. Wintersperger, C. Braun, F. N. Ünal, A. Eckardt, M. D. Liberto, N. Goldman, I. Bloch, and M. Aidelsburger, *Realization of an anomalous Floquet topological system with ultracold atoms*, en, Nat. Phys. **16**, Publisher: Nature Publishing Group, 1058 (2020).

[62] A. Impertro, S. Huh, S. Karch, J. F. Wienand, and M. Aidelsburger, *Strongly interacting Meissner phases in large bosonic flux ladders*, en, Nat. Phys. **21**, Publisher: Nature Publishing Group, 895 (2025).

[63] J. Léonard, S. Kim, J. Kwan, P. Segura, F. Grusdt, C. Repellin, N. Goldman, and M. Greiner, *Realization of a fractional quantum Hall state with ultracold atoms*, en, Nature **619**, Publisher: Nature Publishing Group, 495 (2023).

[64] C. Wang, F.-M. Liu, M.-C. Chen, H. Chen, X.-H. Zhao, C. Ying, Z.-X. Shang, J.-W. Wang, Y.-H. Huo, C.-Z. Peng, X. Zhu, C.-Y. Lu, and J.-W. Pan, *Realization of fractional quantum Hall state with interacting photons*, Science **384**, Publisher: American Association for the Advancement of Science, 579 (2024).

[65] M. S. Rudner, N. H. Lindner, E. Berg, and M. Levin, *Anomalous Edge States and the Bulk-Edge Correspondence for Periodically Driven Two-Dimensional Systems*, Phys. Rev. X **3**, Publisher: American Physical Society, 031005 (2013).

[66] P. Titum, E. Berg, M. S. Rudner, G. Refael, and N. H. Lindner, *Anomalous Floquet-Anderson Insulator as a Nonadiabatic Quantized Charge Pump*, Phys. Rev. X **6**, Publisher: American Physical Society, 021013 (2016).

[67] A. Kundu, M. Rudner, E. Berg, and N. H. Lindner, *Quantized large-bias current in the anomalous Floquet-Anderson insulator*, Phys. Rev. B **101**, Publisher: American Physical Society, 041403 (2020).

[68] M. Atala, M. Aidelsburger, J. T. Barreiro, D. Abanin, T. Kitagawa, E. Demler, and I. Bloch, *Direct measurement of the Zak phase in topological Bloch bands*, en, Nat. Phys. **9**, Publisher: Nature Publishing Group, 795 (2013).

[69] L. Duca, T. Li, M. Reitter, I. Bloch, M. Schleier-Smith, and U. Schneider, *An Aharonov-Bohm interferometer for determining Bloch band topology*, Science **347**, Publisher: American Association for the Advancement of Science, 288 (2015).

[70] M. Aidelsburger, M. Lohse, C. Schweizer, M. Atala, J. T. Barreiro, S. Nascimbène, N. R. Cooper, I. Bloch, and N. Goldman, *Measuring the Chern number of Hofstadter bands with ultracold bosonic atoms*, en, Nat. Phys. **11**, Publisher: Nature Publishing Group, 162 (2015).

[71] N. Fläschner, B. S. Rem, M. Tarnowski, D. Vogel, D.-S. Lühmann, K. Sengstock, and C. Weitenberg, *Experimental reconstruction of the Berry curvature in a Floquet Bloch band*, Science **352**, Publisher: American Association for the Advancement of Science, 1091 (2016).

[72] L. Asteria, D. T. Tran, T. Ozawa, M. Tarnowski, B. S. Rem, N. Fläschner, K. Sengstock, N. Goldman, and C. Weitenberg, *Measuring quantized circular dichroism in ultracold topological matter*, en, Nat. Phys. **15**, Publisher: Nature Publishing Group, 449 (2019).

[73] J. Li, R.-L. Chu, J. K. Jain, and S.-Q. Shen, *Topological Anderson Insulator*, Phys. Rev. Lett. **102**, Publisher: American Physical Society, 136806 (2009).

[74] E. J. Meier, F. A. An, A. Dauphin, M. Maffei, P. Massignan, T. L. Hughes, and B. Gadway, *Observation of the topological Anderson insulator in disordered atomic wires*, Science **362**, Publisher: American Association for the Advancement of Science, 929 (2018).

[75] S. Nakajima, N. Takei, K. Sakuma, Y. Kuno, P. Marra, and Y. Takahashi, *Competition and interplay between topology and quasi-periodic disorder in Thouless pumping of ultracold atoms*, en, Nat. Phys. **17**, Publisher: Nature Publishing Group, 844 (2021).

[76] S. Stützer, Y. Plotnik, Y. Lumer, P. Titum, N. H. Lindner, M. Segev, M. C. Rechtsman, and A. Szameit, *Photonic topological Anderson insulators*, en, Nature **560**, Number: 7719 Publisher: Nature Publishing Group, 461 (2018).

[77] G.-G. Liu, Y. Yang, X. Ren, H. Xue, X. Lin, Y.-H. Hu, H.-x. Sun, B. Peng, P. Zhou, Y. Chong, and B. Zhang, *Topological Anderson Insulator in Disordered Photonic Crystals*, Phys. Rev. Lett. **125**, Publisher: American Physical Society, 133603 (2020).

[78] X.-D. Chen, Z.-X. Gao, X. Cui, H.-C. Mo, W.-J. Chen, R.-Y. Zhang, C. T. Chan, and J.-W. Dong, *Realization of Time-Reversal Invariant Photonic Topological Anderson Insulators*, Phys. Rev. Lett. **133**, Publisher: American Physical Society, 133802 (2024).

[79] C. Braun, R. Saint-Jalm, A. Hesse, J. Arceri, I. Bloch, and M. Aidelsburger, *Real-space detection and manipulation of topological edge modes with ultracold atoms*, Nat. Phys. **20**, 1306 (2024).

[80] A. Hesse, J. Arceri, M. Hornung, C. Braun, and M. Aidelsburger, *Probing disorder-driven topological phase transitions via topological edge modes with ultracold atoms in Floquet-engineered honeycomb lattices*, arXiv:2508.20154, preprint (2025).

[81] M. V. Berry, *Quantal phase factors accompanying adiabatic changes*, Proceedings of the Royal Society of London. A. Mathematical and Physical Sciences **392**, Publisher: Royal Society, 45 (1997).

[82] G. Floquet, *Sur les équations différentielles linéaires à coefficients périodiques*, fr, Annales scientifiques de l'École Normale Supérieure **12**, 47 (1883).

[83] J. H. Shirley, *Solution of the Schrödinger Equation with a Hamiltonian Periodic in Time*, Physical Review **138**, Publisher: American Physical Society, B979 (1965).

[84] M. Grifoni and P. Hänggi, *Driven quantum tunneling*, Physics Reports **304**, 229 (1998).

[85] A. Eckardt, *Colloquium: Atomic quantum gases in periodically driven optical lattices*, Reviews of Modern Physics **89**, Publisher: American Physical Society, 011004 (2017).

[86] W. Magnus, *On the exponential solution of differential equations for a linear operator*, en, Communications on Pure and Applied Mathematics **7**, 649 (1954).

[87] M. M. Maricq, *Application of average Hamiltonian theory to the NMR of solids*, Phys. Rev. B **25**, Publisher: American Physical Society, 6622 (1982).

[88] N. Goldman and J. Dalibard, *Periodically Driven Quantum Systems: Effective Hamiltonians and Engineered Gauge Fields*, en, Phys. Rev. X **4**, 031027 (2014).

[89] Y.-J. Lin, K. Jiménez-García, and I. B. Spielman, *Spin–orbit-coupled Bose–Einstein condensates*, en, Nature **471**, Publisher: Nature Publishing Group, 83 (2011).

[90] T. Kitagawa, E. Berg, M. Rudner, and E. Demler, *Topological characterization of periodically driven quantum systems*, Phys. Rev. B **82**, Publisher: American Physical Society, 235114 (2010).

[91] S. Mukherjee, A. Spracklen, M. Valiente, E. Andersson, P. Öhberg, N. Goldman, and R. R. Thomson, *Experimental observation of anomalous topological edge modes in a slowly driven photonic lattice*, en, Nature Communications **8**, Publisher: Nature Publishing Group, 13918 (2017).

[92] L. J. Maczewsky, J. M. Zeuner, S. Nolte, and A. Szameit, *Observation of photonic anomalous Floquet topological insulators*, en, Nature Communications **8**, Publisher: Nature Publishing Group, 13756 (2017).

[93] F. Gao, Z. Gao, X. Shi, Z. Yang, X. Lin, H. Xu, J. D. Joannopoulos, M. Soljačić, H. Chen, L. Lu, Y. Chong, and B. Zhang, *Probing topological protection using a designer surface plasmon structure*, en, Nature Communications **7**, Publisher: Nature Publishing Group, 11619 (2016).

[94] S. Afzal, T. J. Zimmerling, Y. Ren, D. Perron, and V. Van, *Realization of Anomalous Floquet Insulators in Strongly Coupled Nanophotonic Lattices*, Phys. Rev. Lett. **124**, Publisher: American Physical Society, 253601 (2020).

[95] W. Hu, J. C. Pillay, K. Wu, M. Pasek, P. P. Shum, and Y. D. Chong, *Measurement of a Topological Edge Invariant in a Microwave Network*, Phys. Rev. X **5**, Publisher: American Physical Society, 011012 (2015).

[96] Z. Zhang, P. Delplace, and R. Fleury, *Superior robustness of anomalous non-reciprocal topological edge states*, en, Nature **598**, Publisher: Nature Publishing Group, 293 (2021).

[97] Y.-G. Peng, C.-Z. Qin, D.-G. Zhao, Y.-X. Shen, X.-Y. Xu, M. Bao, H. Jia, and X.-F. Zhu, *Experimental demonstration of anomalous Floquet topological insulator for sound*, en, Nature Communications **7**, Publisher: Nature Publishing Group, 13368 (2016).

[98] A. D'Errico, F. Cardano, M. Maffei, A. Dauphin, R. Barboza, C. Esposito, B. Piccirillo, M. Lewenstein, P. Massignan, and L. Marrucci, *Two-dimensional topological quantum walks in the momentum space of structured light*, EN, Optica **7**, Publisher: Optica Publishing Group, 108 (2020).

[99] F. Nathan and M. S. Rudner, *Topological singularities and the general classification of Floquet–Bloch systems*, en, New Journal of Physics **17**, Publisher: IOP Publishing, 125014 (2015).

[100] C. A. Bracamontes, J. Maslek, and J. V. Porto, *Realization of a Floquet-Engineered Moat Band for Ultracold Atoms*, Phys. Rev. Lett. **128**, Publisher: American Physical Society, 213401 (2022).

[101] T. A. Sedrakyan, L. I. Glazman, and A. Kamenev, *Spontaneous Formation of a Nonuniform Chiral Spin Liquid in a Moat-Band Lattice*, Phys. Rev. Lett. **114**, Publisher: American Physical Society, 037203 (2015).

[102] C. Wei and T. A. Sedrakyan, *Chiral spin liquid state of strongly interacting bosons with a moat dispersion: A Monte Carlo simulation*, Annals of Physics **456**, 169354 (2023).

[103] G. Roati, C. D'Errico, L. Fallani, M. Fattori, C. Fort, M. Zaccanti, G. Modugno, M. Modugno, and M. Inguscio, *Anderson localization of a non-interacting Bose–Einstein condensate*, en, Nature **453**, Publisher: Nature Publishing Group, 895 (2008).

[104] J. Billy, V. Josse, Z. Zuo, A. Bernard, B. Hambrecht, P. Lugan, D. Clément, L. Sanchez-Palencia, P. Bouyer, and A. Aspect, *Direct observation of Anderson localization of matter waves in a controlled disorder*, en, Nature **453**, Publisher: Nature Publishing Group, 891 (2008).

[105] S. S. Kondov, W. R. McGehee, J. J. Zirbel, and B. DeMarco, *Three-Dimensional Anderson Localization of Ultracold Matter*, Science **334**, Publisher: American Association for the Advancement of Science, 66 (2011).

[106] F. Jendrzejewski, A. Bernard, K. Mueller, P. Cheinet, V. Josse, M. Piraud, L. Pezzé, L. Sanchez-Palencia, A. Aspect, and P. Bouyer, *Three-dimensional localization of ultracold atoms in an optical disordered potential*, en, Nat. Phys. **8**, 398 (2012).

[107] G. Semeghini, M. Landini, P. Castilho, S. Roy, G. Spagnolli, A. Trenkwalder, M. Fattori, M. Inguscio, and G. Modugno, *Measurement of the mobility edge for 3D Anderson localization*, en, Nat. Phys. **11**, Publisher: Nature Publishing Group, 554 (2015).

[108] A. Dutta, E. Sen, J.-H. Zheng, M. Aidelsburger, and W. Hofstetter, *Anomalous Floquet Anderson insulator in a continuously driven optical lattice*, Phys. Rev. B **109**, Publisher: American Physical Society, L121114 (2024).

[109] J.-H. Zheng, A. Dutta, M. Aidelsburger, and W. Hofstetter, *Floquet topological phase transitions induced by uncorrelated or correlated disorder*, Phys. Rev. B **109**, Publisher: American Physical Society, 184201 (2024).

[110] D. J. Bishop, D. C. Tsui, and R. C. Dynes, *Nonmetallic Conduction in Electron Inversion Layers at Low Temperatures*, Phys. Rev. Lett. **44**, Publisher: American Physical Society, 1153 (1980).

[111] G. Bergmann, *Weak localization in thin films: a time-of-flight experiment with conduction electrons*, Physics Reports **107**, 1 (1984).

[112] G. Bergmann, *Quantitative analysis of weak localization in thin Mg films by magnetoresistance measurements*, Phys. Rev. B **25**, Publisher: American Physical Society, 2937 (1982).

[113] F. Jendrzejewski, K. Müller, J. Richard, A. Date, T. Plisson, P. Bouyer, A. Aspect, and V. Josse, *Coherent Backscattering of Ultracold Atoms*, en, Phys. Rev. Lett. **109**, 195302 (2012).

[114] P. W. Anderson, *Absence of Diffusion in Certain Random Lattices*, Physical Review **109**, Publisher: American Physical Society, 1492 (1958).

[115] E. Abrahams, P. W. Anderson, D. C. Licciardello, and T. V. Ramakrishnan, *Scaling Theory of Localization: Absence of Quantum Diffusion in Two Dimensions*, Phys. Rev. Lett. **42**, Publisher: American Physical Society, 673 (1979).

[116] T. A. Loring and M. B. Hastings, *Disordered topological insulators via C*-algebras*, en, Europhysics Letters **92**, 67004 (2011).

[117] L. Duca, *Probing topological properties of Bloch bands with ultracold atoms in a honeycomb optical lattice*, PhD Thesis, Ludwig-Maximilians-Universität München (2015).

[118] T. Li, *Probing Bloch band geometry with ultracold atoms in optical lattices*, PhD Thesis, Ludwig-Maximilians-Universität München (2016).

[119] M. Reitter, *Scattering processes in interacting Floquet systems*, PhD Thesis, Ludwig-Maximilians-Universität München (2017).

[120] J. Näger, *Parametric instabilities of interacting bosons in driven optical lattices*, PhD Thesis, Ludwig-Maximilians-Universität München (2019).

[121] K. Wintersperger, *Realization of Floquet topological systems with ultracold atoms in optical honeycomb lattices*, PhD Thesis, Ludwig-Maximilians-Universität München (2020).

[122] C. Braun, *Real-space detection and manipulation of topological edge modes with ultracold atoms*, PhD Thesis, Ludwig-Maximilians-Universität München (2024).

[123] D. A. Steck, *Rubidium 87 D Line Data*,

[124] T. G. Tiecke, *Properties of Potassium*,

[125] J. Schoser, A. Batär, R. Löw, V. Schweikhard, A. Grabowski, Y. B. Ovchinnikov, and T. Pfau, *Intense source of cold Rb atoms from a pure two-dimensional magneto-optical trap*, Phys. Rev. A **66**, Publisher: American Physical Society, 023410 (2002).

[126] K. Dieckmann, R. J. C. Spreeuw, M. Weidemüller, and J. T. M. Walraven, *Two-dimensional magneto-optical trap as a source of slow atoms*, Phys. Rev. A **58**, Publisher: American Physical Society, 3891 (1998).

[127] H. J. Metcalf and P. Van Der Straten, *Laser Cooling and Trapping*, edited by R. S. Berry, J. L. Birman, J. W. Lynn, M. P. Silverman, H. E. Stanley, and M. Voloshin, Graduate Texts in Contemporary Physics (Springer, New York, NY, 1999).

[128] C. J. Foot, *Atomic Physics*, Oxford Master Series in Physics (Oxford University Press, Oxford, New York, 2004).

[129] V. Gokhroo, G. Rajalakshmi, R. K. Easwaran, and C. S. Unnikrishnan, *Sub-Doppler deep-cooled bosonic and fermionic isotopes of potassium in a compact 2D+–3D MOT set-up*, en, Journal of Physics B: Atomic, Molecular and Optical Physics **44**, 115307 (2011).

[130] W. Petrich, M. H. Anderson, J. R. Ensher, and E. A. Cornell, *Behavior of atoms in a compressed magneto-optical trap*, EN, JOSA B **11**, Publisher: Optica Publishing Group, 1332 (1994).

[131] M. Landini, S. Roy, L. Carcagní, D. Trypogeorgos, M. Fattori, M. Inguscio, and G. Modugno, *Sub-Doppler laser cooling of potassium atoms*, Phys. Rev. A **84**, Publisher: American Physical Society, 043432 (2011).

[132] M. Greiner, I. Bloch, T. W. Hänsch, and T. Esslinger, *Magnetic transport of trapped cold atoms over a large distance*, Phys. Rev. A **63**, Publisher: American Physical Society, 031401 (2001).

[133] D. S. Naik and C. Raman, *Optically plugged quadrupole trap for Bose-Einstein condensates*, Phys. Rev. A **71**, Publisher: American Physical Society, 033617 (2005).

[134] D. M. Brink and C. V. Sukumar, *Majorana spin-flip transitions in a magnetic trap*, Phys. Rev. A **74**, Publisher: American Physical Society, 035401 (2006).

[135] A. L. Migdall, J. V. Prodan, W. D. Phillips, T. H. Bergeman, and H. J. Metcalf, *First Observation of Magnetically Trapped Neutral Atoms*, Phys. Rev. Lett. **54**, Publisher: American Physical Society, 2596 (1985).

[136] H. F. Hess, *Evaporative cooling of magnetically trapped and compressed spin-polarized hydrogen*, Phys. Rev. B **34**, Publisher: American Physical Society, 3476 (1986).

[137] K. B. Davis, M.-O. Mewes, M. A. Joffe, M. R. Andrews, and W. Ketterle, *Evaporative Cooling of Sodium Atoms*, Phys. Rev. Lett. **74**, Publisher: American Physical Society, 5202 (1995).

[138] L. De Sarlo, P. Maioli, G. Barontini, J. Catani, F. Minardi, and M. Inguscio, *Collisional properties of sympathetically cooled $^{39}\mathrm{K}$*, Phys. Rev. A **75**, Publisher: American Physical Society, 022715 (2007).

[139] F. H. Mies, C. J. Williams, P. S. Julienne, and M. Krauss, *Estimating Bounds on Collisional Relaxation Rates of Spin-Polarized 87Rb Atoms at Ultracold Temperatures*, eng, Journal of Research of the National Institute of Standards and Technology **101**, 521 (1996).

[140] F. Ferlaino, C. D'Errico, G. Roati, M. Zaccanti, M. Inguscio, G. Modugno, and A. Simoni, *Feshbach spectroscopy of a $\mathrm{K}\text{\ensuremath{-}}\mathrm{Rb}$ atomic mixture*, Phys. Rev. A **73**, Publisher: American Physical Society, 040702 (2006).

[141] C. D'Errico, M. Zaccanti, M. Fattori, G. Roati, M. Inguscio, G. Modugno, and A. Simoni, *Feshbach resonances in ultracold 39K*, en, New Journal of Physics **9**, 223 (2007).

[142] A. Ashkin, *Trapping of Atoms by Resonance Radiation Pressure*, Phys. Rev. Lett. **40**, Publisher: American Physical Society, 729 (1978).

[143] S. Chu, J. E. Bjorkholm, A. Ashkin, and A. Cable, *Experimental Observation of Optically Trapped Atoms*, Phys. Rev. Lett. **57**, Publisher: American Physical Society, 314 (1986).

[144] Y. Shin, M. Saba, T. A. Pasquini, W. Ketterle, D. E. Pritchard, and A. E. Leanhardt, *Atom Interferometry with Bose-Einstein Condensates in a Double-Well Potential*, Phys. Rev. Lett. **92**, Publisher: American Physical Society, 050405 (2004).

[145] H. Labuhn, D. Barredo, S. Ravets, S. de Léséleuc, T. Macrì, T. Lahaye, and A. Browaeys, *Tunable two-dimensional arrays of single Rydberg atoms for realizing*

quantum Ising models, en, Nature **534**, Publisher: Nature Publishing Group, 667 (2016).

[146] M. Endres, H. Bernien, A. Keesling, H. Levine, E. R. Anschuetz, A. Krajenbrink, C. Senko, V. Vuletic, M. Greiner, and M. D. Lukin, *Atom-by-atom assembly of defect-free one-dimensional cold atom arrays*, Science **354**, Publisher: American Association for the Advancement of Science, 1024 (2016).

[147] C.-L. Hung, X. Zhang, L.-C. Ha, S.-K. Tung, N. Gemelke, and C. Chin, *Extracting density–density correlations from in situ images of atomic quantum gases*, en, New Journal of Physics **13**, 075019 (2011).

[148] K. Zimmermann, A. Jordan, F. Gay, K. Watanabe, T. Taniguchi, Z. Han, V. Bouchiat, H. Sellier, and B. Sacépé, *Tunable transmission of quantum Hall edge channels with full degeneracy lifting in split-gated graphene devices*, en, Nature Communications **8**, Publisher: Nature Publishing Group, 14983 (2017).

[149] T. Werkmeister, J. R. Ehrets, Y. Ronen, M. E. Wesson, D. Najafabadi, Z. Wei, K. Watanabe, T. Taniguchi, D. E. Feldman, B. I. Halperin, A. Yacoby, and P. Kim, *Strongly coupled edge states in a graphene quantum Hall interferometer*, en, Nature Communications **15**, Publisher: Nature Publishing Group, 6533 (2024).

[150] N. Liebster, M. Sparn, E. Kath, J. Duchene, H. Strobel, and M. K. Oberthaler, *Supersolid-like sound modes in a driven quantum gas*, en, Nat. Phys. **21**, Publisher: Nature Publishing Group, 1064 (2025).

[151] J.-y. Choi, S. Hild, J. Zeiher, P. Schauß, A. Rubio-Abadal, T. Yefsah, V. Khemani, D. A. Huse, I. Bloch, and C. Gross, *Exploring the many-body localization transition in two dimensions*, Science **352**, Publisher: American Association for the Advancement of Science, 1547 (2016).

[152] P. Sompet, S. Hirthe, D. Bourgund, T. Chalopin, J. Bibo, J. Koepsell, P. Bojović, R. Verresen, F. Pollmann, G. Salomon, C. Gross, T. A. Hilker, and I. Bloch, *Realizing the symmetry-protected Haldane phase in Fermi–Hubbard ladders*, en, Nature **606**, Publisher: Nature Publishing Group, 484 (2022).

[153] S. Hirthe, T. Chalopin, D. Bourgund, P. Bojović, A. Bohrdt, E. Demler, F. Grusdt, I. Bloch, and T. A. Hilker, *Magnetically mediated hole pairing in fermionic ladders of ultracold atoms*, en, Nature **613**, Publisher: Nature Publishing Group, 463 (2023).

[154] T. D. Stanescu, V. Galitski, and S. Das Sarma, *Topological states in two-dimensional optical lattices*, Phys. Rev. A **82**, Publisher: American Physical Society, 013608 (2010).

[155] M. Buchhold, D. Cocks, and W. Hofstetter, *Effects of smooth boundaries on topological edge modes in optical lattices*, Phys. Rev. A **85**, Publisher: American Physical Society, 063614 (2012).

[156] N. Goldman, J. Dalibard, A. Dauphin, F. Gerbier, M. Lewenstein, P. Zoller, and I. B. Spielman, *Direct imaging of topological edge states in cold-atom systems*, Proceedings of the National Academy of Sciences **110**, Publisher: Proceedings of the National Academy of Sciences, 6736 (2013).

[157] Y. Deng and D. Chu, *Coherence properties of different light sources and their effect on the image sharpness and speckle of holographic displays*, en, Scientific Reports **7**, Publisher: Nature Publishing Group, 5893 (2017).

[158] J. W. Goodman, *Speckle Phenomena in Optics: Theory and Applications, Second Edition* (SPIE, 2020).

[159] J. W. Goodman, *Introduction to Fourier Optics*, Englisch (Roberts, Englewood, Colo, 2016).

[160] M. Bass, E. W. V. Stryland, W. D. R, W. L. Wolfe, and O. S. o. America, *Handbook of Optics: Fundamentals, Techniques, and Design*, Englisch (McGraw-Hill Professional, New York, 1994).

[161] J. Chaves, *Introduction to Nonimaging Optics*, English (CRC Press, 2017).

[162] L. Fallani, J. E. Lye, V. Guarrera, C. Fort, and M. Inguscio, *Ultracold Atoms in a Disordered Crystal of Light: Towards a Bose Glass*, Phys. Rev. Lett. **98**, Publisher: American Physical Society, 130404 (2007).

[163] B. Deissler, M. Zaccanti, G. Roati, C. D'Errico, M. Fattori, M. Modugno, G. Modugno, and M. Inguscio, *Delocalization of a disordered bosonic system by repulsive interactions*, en, Nat. Phys. **6**, Publisher: Nature Publishing Group, 354 (2010).

[164] M. Schreiber, S. S. Hodgman, P. Bordia, H. P. Lüschen, M. H. Fischer, R. Vosk, E. Altman, U. Schneider, and I. Bloch, *Observation of many-body localization of interacting fermions in a quasirandom optical lattice*, Science **349**, Publisher: American Association for the Advancement of Science, 842 (2015).

[165] A. Lukin, M. Rispoli, R. Schittko, M. E. Tai, A. M. Kaufman, S. Choi, V. Khemani, J. Léonard, and M. Greiner, *Probing entanglement in a many-body–localized system*, Science **364**, Publisher: American Association for the Advancement of Science, 256 (2019).

[166] L. Koehn, C. Parsonage, C. W. Duncan, P. Kirton, A. J. Daley, T. Hilker, E. Haller, A. L. Rooij, and S. Kuhr, *Quantum-gas microscopy of the Bose-glass phase*, arXiv:2504.13040 [cond-mat], 2025.

[167] M. White, M. Pasienski, D. McKay, S. Q. Zhou, D. Ceperley, and B. DeMarco, *Strongly Interacting Bosons in a Disordered Optical Lattice*, Phys. Rev. Lett. **102**, Publisher: American Physical Society, 055301 (2009).

[168] S. Krinner, D. Stadler, J. Meineke, J.-P. Brantut, and T. Esslinger, *Superfluidity with disorder in a thin film of quantum gas*, Phys. Rev. Lett. **110**, Publisher: American Physical Society, 100601 (2013).

[169] B. Lecoutre, Y. Guo, X. Yu, M. Niranjan, M. Mukhtar, V. V. Volchkov, A. Aspect, and V. Josse, *Bichromatic state-dependent disordered potential for Anderson localization of ultracold atoms*, en, The European Physical Journal D **76**, 218 (2022).

[170] S. Hiebel, B. Nagler, S. Barbosa, J. Koch, and A. Widera, *Characterizing quantum gases in time-controlled disorder realizations using cross-correlations of density distributions*, en, New Journal of Physics **26**, Publisher: IOP Publishing, 013042 (2024).

[171] T. Schulte, S. Drenkelforth, J. Kruse, R. Tiemeyer, K. Sacha, J. Zakrzewski, M. Lewenstein, W. Ertmer, and J. J. Arlt, *Analysis of localization phenomena in weakly interacting disordered lattice gases*, en, New Journal of Physics **8**, 230 (2006).

[172] Y. P. Chen, J. Hitchcock, D. Dries, M. Junker, C. Welford, and R. G. Hulet, *Phase coherence and superfluid-insulator transition in a disordered Bose-Einstein condensate*, Phys. Rev. A **77**, Publisher: American Physical Society, 033632 (2008).

[173] W. R. McGehee, S. S. Kondov, W. Xu, J. J. Zirbel, and B. DeMarco, *Three-Dimensional Anderson Localization in Variable Scale Disorder*, Phys. Rev. Lett. **111**, Publisher: American Physical Society, 145303 (2013).

[174] V. V. Volchkov, M. Pasek, V. Denechaud, M. Mukhtar, A. Aspect, D. Delande, and V. Josse, *Measurement of Spectral Functions of Ultracold Atoms in Disordered Potentials*, Phys. Rev. Lett. **120**, Publisher: American Physical Society, 060404 (2018).

[175] B. Gadway, D. Pertot, R. Reimann, M. G. Cohen, and D. Schneble, *Analysis of Kapitza-Dirac diffraction patterns beyond the Raman-Nath regime*, EN, Optics Express **17**, Publisher: Optica Publishing Group, 19173 (2009).

[176] J. H. Huckans, I. B. Spielman, B. L. Tolra, W. D. Phillips, and J. V. Porto, *Quantum and classical dynamics of a Bose-Einstein condensate in a large-period optical lattice*, Phys. Rev. A **80**, Publisher: American Physical Society, 043609 (2009).

[177] O. Morsch and M. Oberthaler, *Dynamics of Bose-Einstein condensates in optical lattices*, Reviews of Modern Physics **78**, Publisher: American Physical Society, 179 (2006).

[178] M. Lewenstein, A. Sanpera, and V. Ahufinger, *Ultracold Atoms in Optical Lattices: Simulating quantum many-body systems* (Oxford University Press, 2012).

[179] P. L. Kapitza and P. a. M. Dirac, *The reflection of electrons from standing light waves*, en, Mathematical Proceedings of the Cambridge Philosophical Society **29**, 297 (1933).

[180] P. Pedri, L. Pitaevskii, S. Stringari, C. Fort, S. Burger, F. S. Cataliotti, P. Maddaloni, F. Minardi, and M. Inguscio, *Expansion of a Coherent Array of Bose-Einstein Condensates*, Phys. Rev. Lett. **87**, Publisher: American Physical Society, 220401 (2001).

[181] M. Greiner, O. Mandel, T. Esslinger, T. W. Hänsch, and I. Bloch, *Quantum phase transition from a superfluid to a Mott insulator in a gas of ultracold atoms*, en, Nature **415**, Publisher: Nature Publishing Group, 39 (2002).

[182] F. Gerbier, A. Widera, S. Fölling, O. Mandel, T. Gericke, and I. Bloch, *Interference pattern and visibility of a Mott insulator*, Phys. Rev. A **72**, Publisher: American Physical Society, 053606 (2005).

[183] E. Stückelberg, *Theorie der unelastischen Stösse zwischen Atomen*, Helvetica Physica Acta **5**, Publisher: Birkhäuser, 369 (1932).

[184] S. Kling, T. Salger, C. Grossert, and M. Weitz, *Atomic Bloch-Zener Oscillations and Stückelberg Interferometry in Optical Lattices*, Phys. Rev. Lett. **105**, Publisher: American Physical Society, 215301 (2010).

[185] A. Zenesini, D. Ciampini, O. Morsch, and E. Arimondo, *Observation of Stückelberg oscillations in accelerated optical lattices*, Phys. Rev. A **82**, Publisher: American Physical Society, 065601 (2010).

[186] T. Li, L. Duca, M. Reitter, F. Grusdt, E. Demler, M. Endres, M. Schleier-Smith, I. Bloch, and U. Schneider, *Bloch state tomography using Wilson lines*, Science **352**, Publisher: American Association for the Advancement of Science, 1094 (2016).

[187] M. Greiner, I. Bloch, O. Mandel, T. W. Hänsch, and T. Esslinger, *Exploring Phase Coherence in a 2D Lattice of Bose-Einstein Condensates*, Phys. Rev. Lett. **87**, Publisher: American Physical Society, 160405 (2001).

[188] M. R. Andrews, M.-O. Mewes, N. J. van Druten, D. S. Durfee, D. M. Kurn, and W. Ketterle, *Direct, Nondestructive Observation of a Bose Condensate*, Science **273**, Publisher: American Association for the Advancement of Science, 84 (1996).

[189] C. C. Bradley, C. A. Sackett, and R. G. Hulet, *Analysis of in situ images of Bose-Einstein condensates of lithium*, Phys. Rev. A **55**, Publisher: American Physical Society, 3951 (1997).

[190] C. Raman, J. R. Abo-Shaeer, J. M. Vogels, K. Xu, and W. Ketterle, *Vortex Nucleation in a Stirred Bose-Einstein Condensate*, Phys. Rev. Lett. **87**, Publisher: American Physical Society, 210402 (2001).

[191] F. Serwane, G. Zürn, T. Lompe, T. B. Ottenstein, A. N. Wenz, and S. Jochim, *Deterministic Preparation of a Tunable Few-Fermion System*, Science **332**, Publisher: American Association for the Advancement of Science, 336 (2011).

[192] A. M. Kaufman, B. J. Lester, and C. A. Regal, *Cooling a Single Atom in an Optical Tweezer to Its Quantum Ground State*, Phys. Rev. X **2**, Publisher: American Physical Society, 041014 (2012).

[193] W. S. Bakr, J. I. Gillen, A. Peng, S. Fölling, and M. Greiner, *A quantum gas microscope for detecting single atoms in a Hubbard-regime optical lattice*, en, Nature **462**, Publisher: Nature Publishing Group, 74 (2009).

[194] L. W. Cheuk, M. A. Nichols, M. Okan, T. Gersdorf, V. V. Ramasesh, W. S. Bakr, T. Lompe, and M. W. Zwierlein, *Quantum-Gas Microscope for Fermionic Atoms*, Phys. Rev. Lett. **114**, Publisher: American Physical Society, 193001 (2015).

[195] E. Haller, J. Hudson, A. Kelly, D. A. Cotta, B. Peaudecerf, G. D. Bruce, and S. Kuhr, *Single-atom imaging of fermions in a quantum-gas microscope*, en, Nat. Phys. **11**, Publisher: Nature Publishing Group, 738 (2015).

[196] D. Mitra, P. T. Brown, E. Guardado-Sanchez, S. S. Kondov, T. Devakul, D. A. Huse, P. Schauß, and W. S. Bakr, *Quantum gas microscopy of an attractive Fermi–Hubbard system*, en, Nat. Phys. **14**, Publisher: Nature Publishing Group, 173 (2018).

[197] K.-N. Schymik, S. Pancaldi, F. Nogrette, D. Barredo, J. Paris, A. Browaeys, and T. Lahaye, *Single Atoms with 6000-Second Trapping Lifetimes in Optical-Tweezer*

Arrays at Cryogenic Temperatures, Phys. Rev. Applied **16**, Publisher: American Physical Society, 034013 (2021).

[198] F. Gyger, M. Ammenwerth, R. Tao, H. Timme, S. Snigirev, I. Bloch, and J. Zeiher, *Continuous operation of large-scale atom arrays in optical lattices*, Physical Review Research **6**, Publisher: American Physical Society, 033104 (2024).

[199] R. Tao, M. Ammenwerth, F. Gyger, I. Bloch, and J. Zeiher, *High-Fidelity Detection of Large-Scale Atom Arrays in an Optical Lattice*, Phys. Rev. Lett. **133**, Publisher: American Physical Society, 013401 (2024).

[200] S. Anand, C. E. Bradley, R. White, V. Ramesh, K. Singh, and H. Bernien, *A dual-species Rydberg array*, en, Nat. Phys. **20**, Publisher: Nature Publishing Group, 1744 (2024).

[201] H. J. Manetsch, G. Nomura, E. Bataille, K. H. Leung, X. Lv, and M. Endres, *A tweezer array with 6100 highly coherent atomic qubits*, en, Nature, Publisher: Nature Publishing Group, 60 (2025).

[202] T. Gericke, P. Würtz, D. Reitz, T. Langen, and H. Ott, *High-resolution scanning electron microscopy of an ultracold quantum gas*, en, Nat. Phys. **4**, Publisher: Nature Publishing Group, 949 (2008).

[203] C. Veit, N. Zuber, O. A. Herrera-Sancho, V. S. V. Anasuri, T. Schmid, F. Meinert, R. Löw, and T. Pfau, *Pulsed Ion Microscope to Probe Quantum Gases*, Phys. Rev. X **11**, Publisher: American Physical Society, 011036 (2021).

[204] L. Asteria, H. P. Zahn, M. N. Kosch, K. Sengstock, and C. Weitenberg, *Quantum gas magnifier for sub-lattice-resolved imaging of 3D quantum systems*, en, Nature **599**, Publisher: Nature Publishing Group, 571 (2021).

[205] M. Reitter, J. Näger, K. Wintersperger, C. Sträter, I. Bloch, A. Eckardt, and U. Schneider, *Interaction Dependent Heating and Atom Loss in a Periodically Driven Optical Lattice*, Phys. Rev. Lett. **119**, Publisher: American Physical Society, 200402 (2017).

[206] K. Wintersperger, M. Bukov, J. Näger, S. Lellouch, E. Demler, U. Schneider, I. Bloch, N. Goldman, and M. Aidelsburger, *Parametric Instabilities of Interacting Bosons in Periodically Driven 1D Optical Lattices*, Phys. Rev. X **10**, Publisher: American Physical Society, 011030 (2020).

[207] M. Hans, F. Schmutte, C. Viermann, N. Liebster, M. Sparn, M. K. Oberthaler, and H. Strobel, *High signal to noise absorption imaging of alkali atoms at moderate magnetic fields*, Review of Scientific Instruments **92**, 023203 (2021).

[208] A. Bergschneider, V. M. Klinkhamer, J. H. Becher, R. Klemt, G. Zürn, P. M. Preiss, and S. Jochim, *Spin-resolved single-atom imaging of* ^{6}Li *in free space*, Phys. Rev. A **97**, Publisher: American Physical Society, 063613 (2018).

[209] K. Hueck, N. Luick, L. Sobirey, J. Siegl, T. Lompe, H. Moritz, L. W. Clark, and C. Chin, *Calibrating high intensity absorption imaging of ultracold atoms*, EN, Optics Express **25**, Publisher: Optica Publishing Group, 8670 (2017).

[210] G. Reinaudi, T. Lahaye, Z. Wang, and D. Guéry-Odelin, *Strong saturation absorption imaging of dense clouds of ultracold atoms*, EN, Optics Letters, Vol. 32, Issue 21, pp. 3143-3145, Publisher: Optica Publishing Group, 10.1364/OL.32.003143 (2007).

[211] B. I. Halperin, *Quantized Hall conductance, current-carrying edge states, and the existence of extended states in a two-dimensional disordered potential*, Phys. Rev. B **25**, Publisher: American Physical Society, 2185 (1982).

[212] R. Rammal, G. Toulouse, M. T. Jaekel, and B. I. Halperin, *Quantized Hall conductance and edge states: Two-dimensional strips with a periodic potential*, Phys. Rev. B **27**, Publisher: American Physical Society, 5142 (1983).

[213] A. H. MacDonald, *Edge states and quantized Hall conductivity in a periodic potential*, Phys. Rev. B **29**, Publisher: American Physical Society, 6563 (1984).

[214] Y. Hatsugai, *Edge states in the integer quantum Hall effect and the Riemann surface of the Bloch function*, Phys. Rev. B **48**, Publisher: American Physical Society, 11851 (1993).

[215] Y. Hatsugai, *Chern number and edge states in the integer quantum Hall effect*, Phys. Rev. Lett. **71**, Publisher: American Physical Society, 3697 (1993).

[216] X.-L. Qi, Y.-S. Wu, and S.-C. Zhang, *General theorem relating the bulk topological number to edge states in two-dimensional insulators*, Phys. Rev. B **74**, Publisher: American Physical Society, 045125 (2006).

[217] Q. Niu and D. J. Thouless, *Quantised adiabatic charge transport in the presence of substrate disorder and many-body interaction*, en, Journal of Physics A: Mathematical and General **17**, 2453 (1984).

[218] T.-W. Zhou, G. Cappellini, D. Tusi, L. Franchi, J. Parravicini, C. Repellin, S. Greschner, M. Inguscio, T. Giamarchi, M. Filippone, J. Catani, and L. Fallani, *Observation of universal Hall response in strongly interacting Fermions*, Science **381**, Publisher: American Association for the Advancement of Science, 427 (2023).

[219] M. C. Rechtsman, J. M. Zeuner, Y. Plotnik, Y. Lumer, D. Podolsky, F. Dreisow, S. Nolte, M. Segev, and A. Szameit, *Photonic Floquet topological insulators*, en, Nature **496**, Publisher: Nature Publishing Group, 196 (2013).

[220] M. Hafezi, S. Mittal, J. Fan, A. Migdall, and J. M. Taylor, *Imaging topological edge states in silicon photonics*, en, Nature Photonics **7**, Publisher: Nature Publishing Group, 1001 (2013).

[221] J. Ningyuan, C. Owens, A. Sommer, D. Schuster, and J. Simon, *Time- and Site-Resolved Dynamics in a Topological Circuit*, Phys. Rev. X **5**, Publisher: American Physical Society, 021031 (2015).

[222] R. Süsstrunk and S. D. Huber, *Observation of phononic helical edge states in a mechanical topological insulator*, Science **349**, Publisher: American Association for the Advancement of Science, 47 (2015).

[223] T. Ozawa, H. M. Price, A. Amo, N. Goldman, M. Hafezi, L. Lu, M. C. Rechtsman, D. Schuster, J. Simon, O. Zilberberg, and I. Carusotto, *Topological photonics*, Reviews of Modern Physics **91**, Publisher: American Physical Society, 015006 (2019).

[224] M. Leder, C. Grossert, L. Sitta, M. Genske, A. Rosch, and M. Weitz, *Real-space imaging of a topologically protected edge state with ultracold atoms in an amplitude-chirped optical lattice*, en, Nature Communications **7**, Publisher: Nature Publishing Group, 13112 (2016).

[225] S. de Léséleuc, V. Lienhard, P. Scholl, D. Barredo, S. Weber, N. Lang, H. P. Büchler, T. Lahaye, and A. Browaeys, *Observation of a symmetry-protected topological phase of interacting bosons with Rydberg atoms*, Science **365**, Publisher: American Association for the Advancement of Science, 775 (2019).

[226] A. Celi, P. Massignan, J. Ruseckas, N. Goldman, I. B. Spielman, G. Juzeliūnas, and M. Lewenstein, *Synthetic Gauge Fields in Synthetic Dimensions*, Phys. Rev. Lett. **112**, Publisher: American Physical Society, 043001 (2014).

[227] T. Ozawa and H. M. Price, *Topological quantum matter in synthetic dimensions*, en, Nature Reviews Physics **1**, Publisher: Nature Publishing Group, 349 (2019).

[228] M. Mancini, G. Pagano, G. Cappellini, L. Livi, M. Rider, J. Catani, C. Sias, P. Zoller, M. Inguscio, M. Dalmonte, and L. Fallani, *Observation of chiral edge states with neutral fermions in synthetic Hall ribbons*, Science **349**, Publisher: American Association for the Advancement of Science, 1510 (2015).

[229] B. K. Stuhl, H.-I. Lu, L. M. Aycock, D. Genkina, and I. B. Spielman, *Visualizing edge states with an atomic Bose gas in the quantum Hall regime*, Science **349**, Publisher: American Association for the Advancement of Science, 1514 (2015).

[230] T. Chalopin, T. Satoor, A. Evrard, V. Makhalov, J. Dalibard, R. Lopes, and S. Nascimbene, *Probing chiral edge dynamics and bulk topology of a synthetic Hall system*, en, Nat. Phys. **16**, Publisher: Nature Publishing Group, 1017 (2020).

[231] N. Goldman, J. Beugnon, and F. Gerbier, *Detecting Chiral Edge States in the Hofstadter Optical Lattice*, Phys. Rev. Lett. **108**, Publisher: American Physical Society, 255303 (2012).

[232] N. Goldman, G. Jotzu, M. Messer, F. Görg, R. Desbuquois, and T. Esslinger, *Creating topological interfaces and detecting chiral edge modes in a two-dimensional optical lattice*, Phys. Rev. A **94**, Publisher: American Physical Society, 043611 (2016).

[233] B. Wang, M. Aidelsburger, J. Dalibard, A. Eckardt, and N. Goldman, *Cold-Atom Elevator: From Edge-State Injection to the Preparation of Fractional Chern Insulators*, Phys. Rev. Lett. **132**, Publisher: American Physical Society, 163402 (2024).

[234] R. Yao, S. Chi, B. Mukherjee, A. Shaffer, M. Zwierlein, and R. J. Fletcher, *Observation of chiral edge transport in a rapidly rotating quantum gas*, en, Nat. Phys. **20**, Publisher: Nature Publishing Group, 1726 (2024).

[235] J. F. Karcher, S. Gopalakrishnan, and M. C. Rechtsman, *Stability of topologically protected slow light against disorder*, Phys. Rev. A **109**, Publisher: American Physical Society, 063507 (2024).

[236] D. Toniolo, *On the Bott index of unitary matrices on a finite torus*, en, Letters in Mathematical Physics **112**, 126 (2022).

[237] U. Schneider, L. Hackermüller, J. P. Ronzheimer, S. Will, S. Braun, T. Best, I. Bloch, E. Demler, S. Mandt, D. Rasch, and A. Rosch, *Fermionic transport and out-of-equilibrium dynamics in a homogeneous Hubbard model with ultracold atoms*, en, Nat. Phys. **8**, Publisher: Nature Publishing Group, 213 (2012).

[238] J. P. Ronzheimer, M. Schreiber, S. Braun, S. S. Hodgman, S. Langer, I. P. McCulloch, F. Heidrich-Meisner, I. Bloch, and U. Schneider, *Expansion Dynamics of Interacting*

Bosons in Homogeneous Lattices in One and Two Dimensions, Phys. Rev. Lett. **110**, Publisher: American Physical Society, 205301 (2013).

[239] F. Nathan, D. Abanin, E. Berg, N. H. Lindner, and M. S. Rudner, *Anomalous Floquet insulators*, Phys. Rev. B **99**, Publisher: American Physical Society, 195133 (2019).

[240] R. de-Picciotto, M. Reznikov, M. Heiblum, V. Umansky, G. Bunin, and D. Mahalu, *Direct observation of a fractional charge*, en, Nature **389**, Publisher: Nature Publishing Group, 162 (1997).

[241] L. Saminadayar, D. C. Glattli, Y. Jin, and B. Etienne, *Observation of the $e/3$ Fractionally Charged Laughlin Quasiparticle*, Phys. Rev. Lett. **79**, Publisher: American Physical Society, 2526 (1997).

[242] R. Sabo, I. Gurman, A. Rosenblatt, F. Lafont, D. Banitt, J. Park, M. Heiblum, Y. Gefen, V. Umansky, and D. Mahalu, *Edge reconstruction in fractional quantum Hall states*, en, Nat. Phys. **13**, Publisher: Nature Publishing Group, 491 (2017).

[243] J. Nakamura, S. Liang, G. C. Gardner, and M. J. Manfra, *Direct observation of anyonic braiding statistics*, en, Nat. Phys. **16**, Publisher: Nature Publishing Group, 931 (2020).

[244] Y. Ronen, T. Werkmeister, D. Haie Najafabadi, A. T. Pierce, L. E. Anderson, Y. J. Shin, S. Y. Lee, Y. H. Lee, B. Johnson, K. Watanabe, T. Taniguchi, A. Yacoby, and P. Kim, *Aharonov–Bohm effect in graphene-based Fabry–Pérot quantum Hall interferometers*, en, Nature Nanotechnology **16**, Publisher: Nature Publishing Group, 563 (2021).

[245] M. Carrega, L. Chirolli, S. Heun, and L. Sorba, *Anyons in quantum Hall interferometry*, en, Nature Reviews Physics **3**, Publisher: Nature Publishing Group, 698 (2021).

[246] J. Nakamura, S. Liang, G. C. Gardner, and M. J. Manfra, *Impact of bulk-edge coupling on observation of anyonic braiding statistics in quantum Hall interferometers*, en, Nature Communications **13**, Publisher: Nature Publishing Group, 344 (2022).

[247] Ö. Gül, Y. Ronen, S. Y. Lee, H. Shapourian, J. Zauberman, Y. H. Lee, K. Watanabe, T. Taniguchi, A. Vishwanath, A. Yacoby, and P. Kim, *Andreev Reflection in the Fractional Quantum Hall State*, Phys. Rev. X **12**, Publisher: American Physical Society, 021057 (2022).

[248] L. A. Cohen, N. L. Samuelson, T. Wang, T. Taniguchi, K. Watanabe, M. P. Zaletel, and A. F. Young, *Universal chiral Luttinger liquid behavior in a graphene fractional*

quantum Hall point contact, Science **382**, Publisher: American Association for the Advancement of Science, 542 (2023).

[249] A. Lazarides, A. Das, and R. Moessner, *Equilibrium states of generic quantum systems subject to periodic driving*, Physical Review E **90**, Publisher: American Physical Society, 012110 (2014).

[250] L. D'Alessio and M. Rigol, *Long-time Behavior of Isolated Periodically Driven Interacting Lattice Systems*, Phys. Rev. X **4**, Publisher: American Physical Society, 041048 (2014).

[251] K. Viebahn, J. Minguzzi, K. Sandholzer, A.-S. Walter, M. Sajnani, F. Görg, and T. Esslinger, *Suppressing Dissipation in a Floquet-Hubbard System*, Phys. Rev. X **11**, Publisher: American Physical Society, 011057 (2021).

[252] Y. Chen, Z. Zhu, and K. Viebahn, *Mitigating higher-band heating in Floquet-Hubbard lattices via two-tone driving*, Phys. Rev. A **112**, Publisher: American Physical Society, L021301 (2025).

[253] N. R. Cooper, *Optical Flux Lattices for Ultracold Atomic Gases*, Phys. Rev. Lett. **106**, Publisher: American Physical Society, 175301 (2011).

[254] N. R. Cooper and J. Dalibard, *Optical flux lattices for two-photon dressed states*, en, Europhysics Letters **95**, 66004 (2011).

[255] G. Juzeliūnas and I. B. Spielman, *Flux lattices reformulated*, en, New Journal of Physics **14**, Publisher: IOP Publishing, 123022 (2012).

[256] O. E. Sommer and N. R. Cooper, *Ideal Optical Flux Lattices*, arXiv:2509.01481 [cond-mat], 2025.

[257] C. I. Timms, L. M. Sieberer, and M. H. Kolodrubetz, *Quantized Floquet Topology with Temporal Noise*, Phys. Rev. Lett. **127**, Publisher: American Physical Society, 270601 (2021).

[258] P.-P. Zheng, C. I. Timms, and M. H. Kolodrubetz, *Anomalous Floquet-Anderson insulator with quasiperiodic temporal noise*, Phys. Rev. B **108**, Publisher: American Physical Society, 094207 (2023).

Acknowledgements

During the course of my PhD, I have been fortunate to encounter many inspiring people, and even though I cannot possibly name them all, I want to extend my deepest gratitude to those who have most shaped my journey!

First of all, I want to thank Immanuel Bloch and Monika Aidelsburger for giving me the opportunity to pursue a PhD in their lab, and for their supervision throughout the years. They provide an environment, in which talented people and technical know-how are plentiful, and where resources for pursuing ambitious projects are always available. By fostering an atmosphere, in which specialist knowledge is freely shared between the labs, they created an ecosystem in which experiments can rapidly progress. Monikas steady flow of new ideas was invaluable for discovering new directions for future projects, and her sharing her way of thinking about physical problems made the lab meetings a learning experience.

A big thanks goes to the whole Fermi 2 team, which I spent many hours in the lab with, be it taking data, or fixing the machine. Even if the experiment was misbehaved, working with you was always fun! I want to thank Christoph Braun for teaching me, how the experimental setup works, and how to never stop trying if it does not. Your persistent way of not giving up is really inspiring! Johannes Arceri, for performing endless simulations, and for helping to improve the lab in numerous ways - be it the second imaging laser, or completely rebuilding the whole laser cooling setup. I am certain the completely redesigned laser setup will contribute massively to the stability of the experiment in the future. Moritz Hornung, for often challenging beliefs at exactly the right time. Him working tirelessly on understanding speckle potentials, and simulating the diffraction of atoms off it, enabled us to calibrate the speckle potential so nicely. Dizhou Xie, who joined our lab recently as a postdoc, for asking questions about how the lab works, and for not accepting simple answers. I'm sure the experiment is in good hands with you all!

Additional thanks go out to the students writing their thesis or performing internships in our lab: Valentin Weyerer worked on stabilizing the phase of the individual lattice beams on our setup, and found a way of synthesizing arbitrary polarizations extremely well. Simon Karch worked on a new vertical lattice setup, which together with the phase stabilization might help to reduce heating rates in the interacting regime significantly. Carlo Daniel built a setup for a second DMD and worked on improving the flatness of the projected potentials, which might allow us to realize an edge-state-elevator, and to project disorder locally.

I want to thank the whole Bloch & Aidelsburger group, both at LMU and MPQ for the good atmosphere - thank you for the many fun lunch and coffee breaks, and all the evenings spent together. I am grateful for the supportive environment in this group - many problems in the lab could be resolved by just visiting the lab next door, or by calling the labs in Garching. One of the largest assets of this group is the people making it up, and I have tremendously profited from discussions with many of its members - apart from the members of my lab, I want to thank Ronen Kroeze, Alexander Impertro, Etienne Staub, Tim Höhn, Bodo Kaiser, Pascal Weckesser, Giulio Pasqualetti, René Villela, Dominik Bourgund, Sofus

Kristensen, Renhao Tao, Andreas von Haaren, Petar Bojović, Christian Schweizer, and everybody else who I might have forgotten. Special thanks goes out to Johannes, Moritz, Christoph, Giulio, Simon, Bodo and Elli for proofreading parts of this thesis, and for providing valuable feedback, which improved this thesis significantly!

I also want to thank the whole administrative staff at LMU and MPQ - special thanks here go out to Ildiko Keckesi, who navigated me through a plethora of administrative situations, and who always manages to make problems disappear, often without you even noticing it. I also want to thank Bodo Hecker and Reinhard Grottenthaler for helping in designing, improving and fixing the experiments wherever necessary, and for teaching me so many things about analog circuitry. I am grateful to Jürgen Aust and Anton Mayer and their teams in the LMU and MPQ machine shops for manufacturing all the mechanical parts that were needed over the past few years, and for expediting orders where it was really necessary.

I also want to thank André Eckardt, Thomas Birner and Alexander Högele for being part of my thesis defense committee. Special thanks goes out to André Eckardt for agreeing to be the second referee of this thesis.

Beyond the lab, I also want to thank the wonderful people I have around me in my life: I want to thank all the pub quiz (and vacationing in Scotland or Ireland) friends back in Heidelberg, specifically Lisa, Mira, Niko, Daniel, Flo, Josef, and everybody else who was a regular who I might have forgotten to mention! Much of this would not have been possible without your constant support over the past decade! I also want to thank my Schafkopf-, swimming-, sailing-, opera-, theatre, and movie night friends here in Munich, who made day-to-day life so much more fun!

Special thanks goes out to Elli, for constantly supporting me in countless ways, especially over the past few months. Much of this would not have been possible without you being the calm in my storm.

Lastly, I would like to thank my family, especially my parents, for their steady support through all of my life's endeavors.

Thank you!